MASTER THESIS

A NUMERICAL INVESTIGATION OF AERODYNAMICALLY TRAPPED VORTEX COMBUSTOR FOR PREMIXED HYDROGEN COMBUSTION IN GAS TURBINES USING DETAILED CHEMISTRY

SACHIN MENON

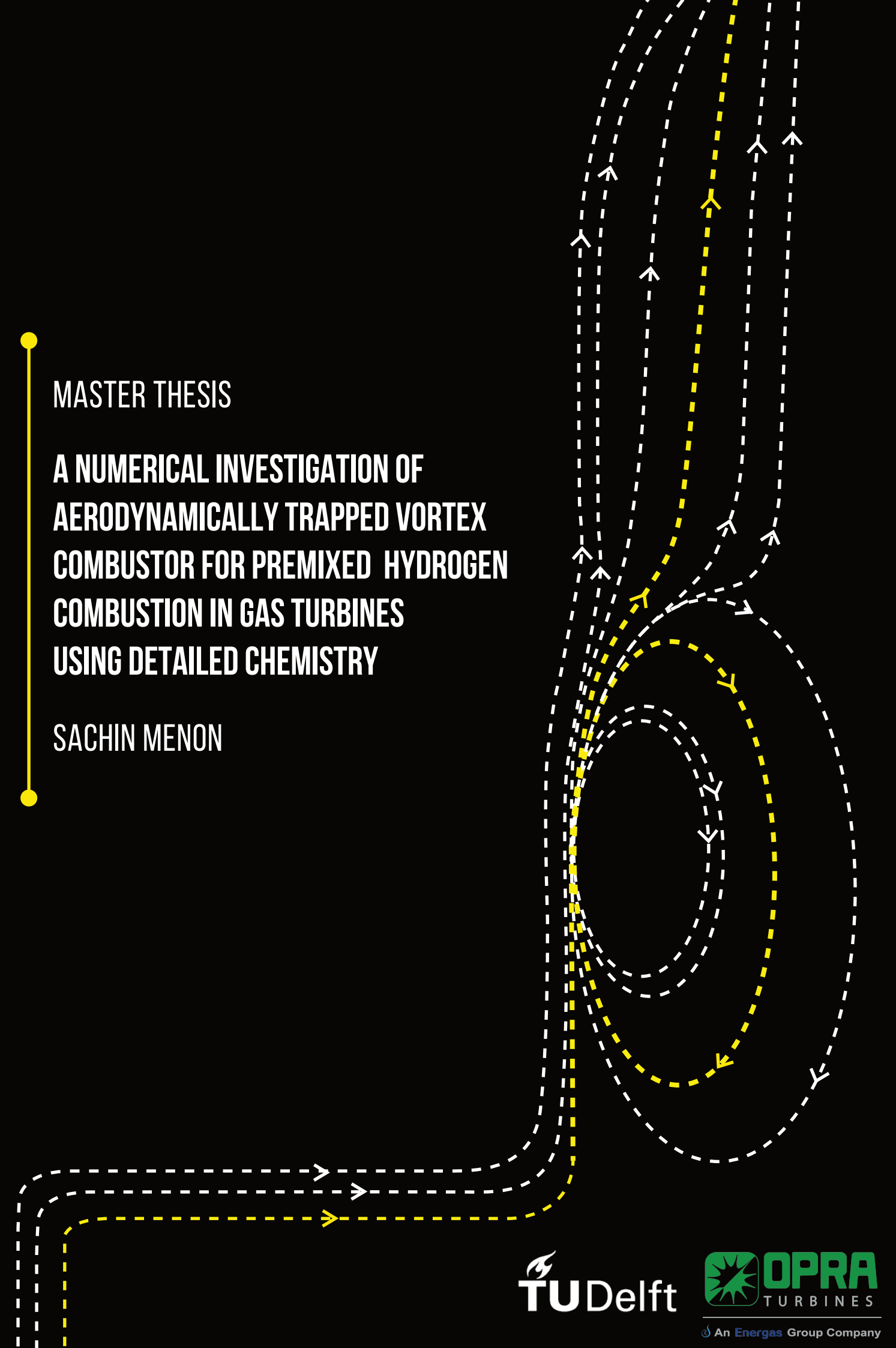

TU Delft

OPRA TURBINES

An Energas Group Company

A Numerical Investigation of Aerodynamically Trapped Vortex Combustor for Premixed Hydrogen Combustion in Gas Turbines Using Detailed Chemistry

Master Thesis

by

Sachin Menon

to obtain the degree of Master of Science in Aerospace Engineering
at the Delft University of Technology,
to be defended publicly on Tuesday, November 26, 2019 at 9:30 am

Student number:	4743571	
Project duration:	December, 2018 – November, 2019	
Thesis committee:	Dr. Arvind Gangoli Rao,	TU Delft, supervisor and chair
	Prof.dr.ir. Sikke Klein	TU Delft, supervisor
	Prof.dr.ing. Georg Eitelberg,	TU Delft, examiner
	Ir. Thijs Bouten,	OPRA Turbines, daily supervisor

An electronic version of this thesis is available at http://repository.tudelft.nl/.

TU Delft

OPRA TURBINES

An Energas Group Company

"We are the representatives of the cosmos; we are an example of what hydrogen atoms can do, given 15 billion years of cosmic evolution."

Carl Sagan

Preface

This thesis is a result of my research and study for more than two years at Delft University of Technology, The Netherlands and at OPRA Turbines, Hengelo, The Netherlands. I'd like to thank my supervisors, Prof. Arvind Gangoli Rao and Prof. Sikke Klein from TU Delft for their help, support and scientific guidance. I thank Prof. D.J.E.M. Roekaerts for the insightful meetings on various theoretical concepts and practical approaches.

I would like to thank my daily supervisor at OPRA Turbines, Thijs Bouten for constant support and guidance throughout the course of this research. My sincere gratitude goes to my department manager and co-supervisor, Jan Withag for the constant motivation and belief in my abilities. Special thanks to Nick Gralike, my first supervisor at OPRA for his continued support and for inviting me to his wedding party.

I'm sincerely thankful to my colleagues at OPRA Turbines, for creating a good working atmosphere. I am expressing my special thanks to Lars-Uno Axelsson, R&D Director at OPRA for taking the time out of his busy schedule for meetings. For help and friendly atmosphere during my work, many thanks to Natalia Terentyeva, Ehsan Fallahi, Gerwin de Weerd, Peter de Graaf, Jan Horvath, Suleyman Karaca, Roland Pross, Marta Grimaldi and everyone at OPRA.

I cannot thank enough Giel Ramaekaers from AVL for all the tutorial sessions, helping with the development of post-processing routines, helping with setting up the simulations, running them, and supporting through each and every step while using AVL Fire for my work.

And finally, last but by no means least, I thank my parents who are with me every step of the way providing all kinds of support and encouragement and special thanks to Lachu & Achu for all the movie nights, dinners, "Amazon" days and many many more.

Abstract

Hydrogen is a clean and carbon-free fuel and is considered a key element for the energy transition. Renewable power generation by solar and wind is increasing, requiring flexible operation to balance the load on the energy grid with the ability to rapidly adjust the output. Gas turbines with a combustion system for hydrogen operation offers a low carbon solution to support the stability of the energy grid. This provides a solution capturing the needs for energy storage, in the form of hydrogen, and flexible power generation. High flame temperatures in the primary zone facilitates the production of NO_x which can be reduced by using premixed combustors. But this introduces the risk of flame flashback. Several combustor concepts have been proposed and studied in the past few years to tackle the problem of flame flashback in premixed high hydrogen fuel combustors. This study looks at one of the concepts which uses Aerodynamically Trapped Vortex to stabilize the flame and studies the flow and flame behavior in the combustor.

Numerical simulations for the analysis were performed with commercial Computational Fluid Dynamics (CFD) simulation package AVL FIRE^{TM}. The flow field characterization was focused on the investigation of the influence of the inlet velocity and inlet turbulence intensity ($u^{'}$) on the mean velocity, wall velocity gradient and turbulence intensity in the combustor. To study the flame stabilization mechanism, reactive simulations were performed at two fuel equivalence ratios. The combustion regime of the flame, wall velocity gradient and temperature distribution in the combustor were quantified from the simulation results.

A validation study was performed prior to the analysis of the ATV combustor to validate both the turbulence and the reactive models for premixed hydrogen combustion. The models were validated against the experiments performed in a dump stabilized cylindrical combustor at Combustion Research Laboratory, Paul Scherrer Institute (PSI), Switzerland. The k-ϵ and k-ζ-f turbulence models were selected for modelling the turbulence. Simulations of non-reacting flow with k-ϵ model resulted in a more accurate prediction of the flow field, turbulence levels and recirculation zone than the k-ζ-f model.

Combustion is modelled using the FIRE^{TM} detailed chemistry solver with the k-ϵ turbulence model to resolve turbulence. No additional turbulence-chemistry interaction model is used in the current research. To reduce chemistry computational time, the multi-zone method is employed. A detailed chemistry approach with sufficient mesh resolution for modelling the reaction in 100% premixed hydrogen combustion predicted the flame behavior with acceptable accuracy. The flow analysis in the Aerodynamically Trapped Vortex (ATV) combustor revealed that the inlet velocity or inlet turbulence had no significant effect on the relative turbulence properties in the flame stabilization zone. The proposed design for the Aerodynamically Trapped Vortex (ATV) combustor was able to stabilize a 100% premixed hydrogen flames without flashback for the simulated conditions.

Keywords : Hydrogen, Premixed flame, Flame flashback, Computational Fluid Dynamics, Aerodynamically Trapped Vortex.

Contents

List of Figures

List of Tables

List of Abbreviations

ATV	Aerodynamically Trapped Vortex
BLF	Boundary Layer Flashback
CAD	Computer Aided Design
CFD	Computational Fluid Dynamics
CIVB	Combustion Induced Vortex Breakdown
CSM	Coherent Structures Model
DLE	Dry Low Emissions
DLN	Dry Low NOx
DNS	Direct Numerical Simulation
EDC	Eddy Dissipation Concept
FGM	Flamelet Generated Manifold
GGPR	General Gas Phase Reactions
HSB	High Swirl Burner
LES	Large Eddy Simulation
LSB	Low Swirl Burner
LHV	Lower Heating Value
MAD	Mixture Averaged Diffusion
MCD	Multi-Component Diffusion
PDF	Probability Density Function
PIV	Particle Image Velocimetry
PLIF	Planar Laser-Induced Fluorescence
PSI	Paul Scherrer Institute
RANS	Reynolds Averaged Navier Stokes
RSM	Reynolds Stress Model
STP	Standard Temperature Pressure
TCI	Turbulence Chemistry Ineraction
TVC	Trapped Vortex Combustor

List of Symbols

Re	Reynolds Number	[-]
Re_L	flame Reynolds Number	[-]
Re_T	turbulent Reynolds Number	[-]
Da	Damköhler number	[-]
Ka	Karlovitz number	[-]
Le	Lewis number	[-]
c	reaction progress variable	[-]
Y	species mass fraction	[-]
X	species mole fraction	[-]
Sc_t	turbulent Schmidt number	[-]
Pr_t	turbulent Prandtl number	[-]
C_p	coefficient of pressure	[-]
D_h	hydraulic diameter	m
L_t	integral length scale	m
u_τ	friction velocity	m/s
$u^{'}$	turbulent intensity	m/s
$\overline{U}$	bulk flow velocity	m/s
S_L	laminar flame speed	m/s
$S_{L,k}$	stretched laminar flame speed	m/s
S_T	turbulent flame speed	m/s
U_0	inlet velocity	m/s
U_{FB}	flashback resistance velocity	m/s
g_f	wall velocity gradient	1/s
g_c	critical velocity gradient	1/s
D_m	molecular diffusion coefficient	m^2/s
c_p	specific heat capacity	kJ/kgK
J	diffusion flux	m/s
P	pressure	Pa(N/m^2)
P_0	inlet pressure	Pa
T_u	preheat temperature	K
T_{ad}	adiabatic flame temperature	K
$\dot{m}$	mass flow rate	kg/s
k	turbulent kinetic energy	m^2/s^2
k_R	reaction rate constant	varies
$\dot{q}_w$	wall heat transfer	W/m^2

Greek Letters

ζ	velocity scale ratio	[-]
ϕ	equivalence ratio	[-]
δ_b	penetration depth	m
δ_f	laminar flame thickness	m
δ_q	quenching distance	m
η	Kolmogorov length scale	m
α	thermal diffusion coefficient	m^2/s

ρ	fluid density	kg/m^3
ρ_u	unburned mixture density	kg/m^3
ρ_b	burned mixture density	kg/m^3
ϵ	turbulent dissipation rate	m^2/s^3
ν	kinematic fluid viscosity	m^2/s
μ	fluid viscosity	kg/ms
μ_t	turbulent fluid viscosity	kg/ms
Γ	total species diffusion coefficient	kg/ms
λ	thermal conductivity	W/mK
τ_w	wall shear stress	kg/ms^2

1 Introduction

The age old proverb "Necessity is the mother of invention" is a perfect way to describe all the groundbreaking inventions since humans discovered fire. Due to the current state of the Earth and interest mostly fired by existential phobia, there has been a surge in development of renewable and clean sources of energy to feed the ever increasing global energy demands. One of those option is to replace all carbon emitting fuels with clean fuels. Among possible clean fuel candidates, hydrogen is on the forefront due to its many advantages to be discussed later. This study looks at possible options to burn hydrogen fuel in gas turbines with very low or no emissions, thus contributing towards the transition to a sustainable future.

1.1. Global Energy

World energy supply has increased by a staggering 150% from 1970 to 2016. While oil remains the dominant fuel, the share of natural gas, nuclear power and renewables has increased significantly as shown in figure 1.1. Since energy from hydrocarbon based fuels is still at large, total carbon emissions also follow a similar trend close to a point of no return. Electricity contributes approximately 20% of the total energy consumption. Electricity production per source is shown in figure 1.2. Close to 75% of electricity comes from combustion of hydrocarbon fuels. Thus replacing all combustion derived energy with combustion free energy is not practical at the moment. A more practical, feasible and innovative option is to replace the fuel with cleaner options like hydrogen and make the transition to complete clean energy smooth.

1.2. Hydrogen energy

Hydrogen provides a solution to sustainable and clean energy sources for future needs of human civilization. Hydrogen paves the way to production of the fuel from variety of raw material, waste products, and excess energy to be utilized to generate heat, electricity and mechanical work in a clean and efficient way (Miranda, 2019).

For energy production, hydrogen can be used in two ways. Firstly by creating electricity from fuel cells at an efficiency close to 60% and secondly by combustion with air to give energy for heating, electricity, propulsive power for aircraft, ships and trains replacing natural gas (Bockris, 2002). When burnt with air, the only products are NO_x and water vapour. There are several techniques to reduce NO_x emissions to be discussed later. The main advantage of using hydrogen as primary fuel in gas turbines is the complete reduction in carbon emission.

Figure 1.3 shows different ways of hydrogen production using energy sources. Major production of hydrogen is by steam reforming of methane or natural gas. More sustainable options are water electrolysis using excess renewable energy such as solar or wind energy.

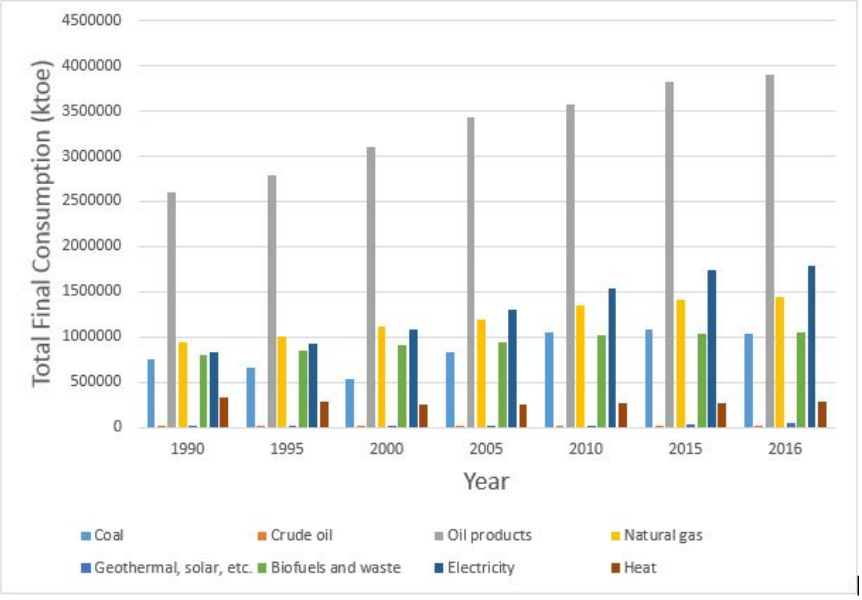

FIGURE 1.1: Total final consumption by source over the years 1990 - 2016. [Based on IEA data from the IEA World Energy Balances 2018 ©IEA 2016, https://webstore.iea.org/world-energy-balances-2018. Licence: www.iea.org/t&c]

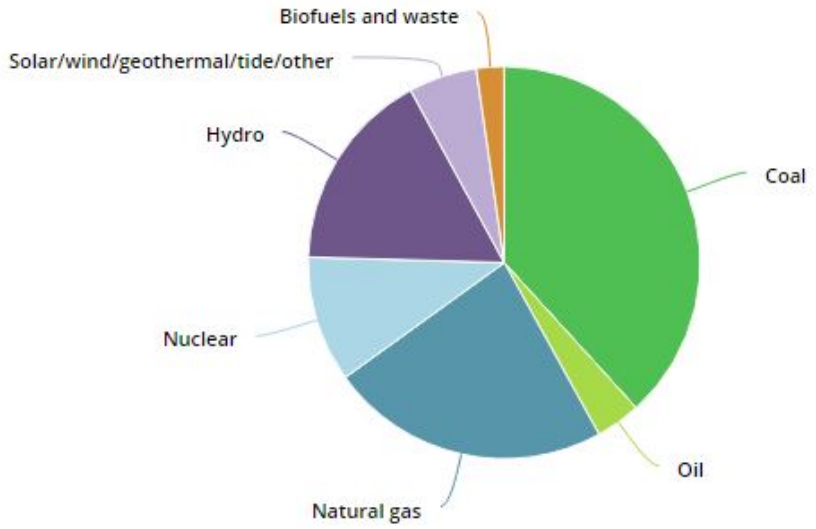

FIGURE 1.2: World gross electricity production, by source, 2016 [Based on IEA data from the Electricity Information 2018 overview ©IEA 2016, https://www.iea.org/statistics/electricity/. Licence:www.iea.org/t&c]

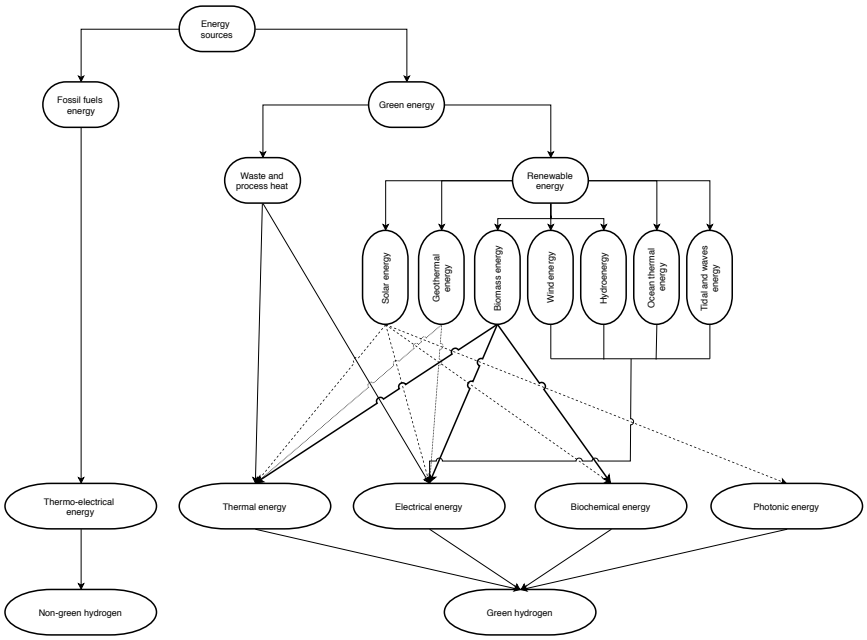

FIGURE 1.3: Energy conversion paths for hydrogen production Miranda, 2019.

One of the main advantages of the latter method is that, hydrogen can be used to complement and adjust electrical energy delivery issues related to inherent intermittence of renewable electricity production (Miranda, 2019).

A hydrogen economy aims at utilizing all the possible applications of hydrogen as a primary fuel and an energy carrier like electricity. The present study focuses on using hydrogen in gas turbines as a fuel to generate electricity, heat and power. Gas turbines provides a fast and flexible solution to peak power demands. Due to their high power to weight ratio, low footprint and low initial costs, they provide power plant flexibility and grid reliability. Complementing renewable sources with gas turbines puts stringent limits on emissions. A need to reduce emissions from combustion of hydrocarbon based fuels has sparked an interest in transition to hydrogen fuel in gas turbines.

1.3. Hydrogen Flame Flashback

Hydrogen is the most abundant element in the universe. It is odourless, colourless and tasteless. With a boiling point of 20.4 K it exists in gaseous state at Normal Temperature Pressure (NTP) conditions (T = 20^{o}C, P = 1 atm). It has a higher Lower Heating Value (LHV) than most fuels with 120 MJ/kg. But because of it's low density (0.0899 g/L), the energy per unit volume is 10.779 MJ/m^3 (*Physical Properties of natural gases* 1988). Stoichiometric hydrogen-air flames at Normal Temperature Pressure (NTP) have an adiabatic flame temperature of 2390K (Movileanu et al., 2011) and laminar flame speeds as high as 3 m/s (Jung, Lee, and Kim, 2016). The laminar flame speed of hydrogen is more than 5 times that of methane.

Flame flashback is one of the prime challenges in premixed hydrogen-air flames due to their higher flame speed. Flame flashback is generally defined as the upstream propagation of the flame due to the imbalance in local flame velocity and flow velocity. During a flashback event, the flame propagates upstream into the premixer and changes the combustion from a premixed flame to a diffusion flame type. This in turn increases the temperatures, the emissions and could cause considerable damage to the equipment.

1.4. Flashback Prevention

For a stable and safe operation of low emission gas turbines with high hydrogen fuels, it is important to solve the problem of flame flashback. Over the years several experimental and numerical studies were performed on different burner concepts aiming at burning hydrogen rich fuel gases. There were also studies aimed towards understanding the flashback mechanism in premixed gas turbines burning high hydrogen fuel. Since flashback is caused by an imbalance in flow velocity and flame speed, using high flow velocities can reduce the flashback propensity in gas turbine combustors. In conventional premixed flame combustors swirling flow produces a recirculation zone which stabilizes the flame. This could introduce the risk of flame blowout when high flow velocity is used.

1.5. Thesis Outline

Burner concepts based on trapped vortex flame stabilization have a higher resistance towards flame blowout than conventional swirl stabilized burners. In 2002, Ansaldo PSM invented the FlameSheet^{TM} combustion system based on trapped vortex flame stabilization for flexible fuel operation (Peter J Stuttaford et al., 2005). The FlameSheet^{TM} combustor uses Aerodynamically Trapped Vortex (ATV) to stabilize the flame. This system can be easily retrofitted into conventional swirl stabilized combustors for fuel flexibility and extended operability.

The lack of extensive studies on the ATV combustor motivates this research to investigate important flow and combustion dynamics of the design. This research focuses on the trapped vortex flame stabilization and sensitivity analysis of the combustor. In Chapter 2 the theory required to understand the concepts and methods used in this thesis are explained.

A numerical approach is adopted for the current research. In chapter 3, the numerical models to be employed in this study are validated with premixed hydrogen combustion experiments performed at the Combustion Research Laboratory, Paul Scherrer Institute, Switzerland. The validation study will help in understanding the merits and shortcomings of the numerical model used in this research for hydrogen combustion and act as a reference for further improvements. The effect of preferential diffusion in turbulent premixed hydrogen flames is also studied. The effective Lewis number of the deficient species in the reaction is calculated based on numerical calculations.

In chapter 4 a detailed procedure is formulated for the preliminary design of the Aerodynamically Trapped Vortex combustor. The combustor is designed to operate at OPRA Turbines operating conditions. The design parameters of the combustor is based on the critical velocity gradient of hydrogen flames.

With the preliminary combustor design, a sensitivity analysis of the ATV combustor is performed in chapter 5. The parameters varied are inlet mass flow rate and inlet turbulence levels. The effect of these parameters on the bulk velocity, turbulence and wall velocity gradient is studied. The bulk velocity and wall velocity gradient gives an idea about the flashback resistance of the combustor. By comparing the behaviour of trapped vortex in both a cold flow and a reactive flow, the effect of heat release on flow dynamics and vortex stabilization can be understood. The knowledge gained from this research could serve as a baseline for further development of ATV combustors, thereby contributing towards the transition to a sustainable and clean energy future.

Finally chapter 6 provides important conclusions from both validation study and sensitivity analysis on the Aerodynamically Trapped Vortex combustor. It also lists areas of improvement and future recommendations for further research on this subject.

2 Theory

The goal of this chapter is to describe the theory behind different concepts and models used in this thesis. A general introduction to properties of turbulent flows is given in section 2.1 followed by characteristics of turbulent premixed flames in section 2.2. A brief description of types of flame flashback mechanisms is given in section 2.3. This is followed by detailed explanation of the two boundary layer flashback prediction models for turbulent premixed hydrogen combustion in section 2.4. These models form the basis of calculation of the combustor geometry. In section 2.5 different combustor designs are reviewed and a detailed overview of the Aerodynamically Trapped Vortex Combustor is given in section 2.5.4. This is followed by detailed description on the computational methods used for this numerical investigation in section 2.6.

2.1. Turbulent Flows

Most kind of fluid flows encountered in practical technical devices are turbulent. Turbulent flow is characterized by chaotic changes in flow properties such as velocity, pressure and temperature. In gas turbines turbulence is highly advantageous since it enhances both mass and heat transfer leading to better fuel mixing and reaction processes.

The onset of turbulence or the transition of laminar to turbulent flow is is predicted by the Reynolds number (Re). The Reynolds number is a non dimensionless quantity given by eq. 2.1:

$$Re = \frac{\text{inertia forces}}{\text{viscous forces}} = \frac{UL}{\nu} \tag{2.1}$$

In eq. 2.1 U is the characteristic flow velocity $[m/s]$, L is the characteristic length scale $[m]$ and ν is the fluid kinematic viscosity $[m^2/s]$. Thus laminar to turbulent flow transitions occurs when the flow disturbances represented by inertia forces exceeds the damping nature of of viscous forces.

Turbulent flows are generally categorized into the wall-bounded and free shear flows. The flows remote from any wall are called free shear flows and the turbulence is generated due to mean velocity gradients (Pope, 2015). In contrast to free shear flows, turbulent flows in most applications are bounded by walls on one or both sides. Turbulent pipe flow is a subclass of bounded flow where the turbulent flow is bounded on all sides by the wall of a pipe.

In a turbulent pipe flow, the characteristic length scale in the Reynolds number equation 2.1 is the hydraulic diameter of the pipe D_h. The boundary layer formed at the entrance to the pipe develops until it merges at the center after a certain length. Beyond this point, the velocity profile is independent of the axial length x and the flow is called "fully developed".

Throughout this work the flow through pipes or pipe like geometry will be approximated as fully developed.

In chapter 4, the preliminary design of the hydrogen combustor is based on the wall velocity gradient of critical sections in the combustor. For a turbulent pipe flow the friction velocity, u_τ follows the relation by Schlichting and Gersten (2016) given by equation 2.2.

$$u_\tau^2 = \frac{\tau_w}{\rho} = 0.03955 \overline{U}^{7/4} \nu^{1/4} D_h^{-1/4} \tag{2.2}$$

where τ_w is the wall shear stress, $\overline{U}$ is the bulk flow velocity and ν is the kinematic viscosity of the fluid. From the above equation, the wall velocity gradient g_f is derived as:

$$g_f = \frac{\tau_w}{\rho \nu} = 0.03955 \overline{U}^{7/4} \nu^{-3/4} D_h^{-1/4} \tag{2.3}$$

2.2. Turbulent Premixed Flames

When the fuel and oxidizer are mixed before entering the reaction zone in the combustor, the flames formed in the reaction are called premixed flames. The fuel and oxidizer are mixed in a ratio within the flammability limits and an ignition source is used during the startup for continuous flames (gas turbines, boilers etc..). The reactions take place in a thin layer, usually thinner than flow scales. The flame properties such as propagation velocity, flame thickness are controlled by transport processes. The transport processes involve heat transport and diffusion of radicals. In turbulent premixed flames, these transport processes are affected by the turbulence in the flow. The interaction between chemical kinetics and turbulence is known as turbulence chemistry interaction.

2.2.1. Flame Regime

To analyze the turbulence-flame interaction, flame regime diagrams like the one shown in figure 2.1 are used. The regime diagram proposed by Borghi (1985) and later modified by Peter (1999) is defined based on the turbulent intensity ($u^{'}$), unstretched laminar flame speed (S_{l0}) , integral length scale (L_T), and unstretched laminar flame thickness (δ_f). The regimes are categorized based on three dimensionless numbers, i.e. the flame Reynolds number (Re_L), the Damköhler number (Da) and the Karlovitz number (Ka). The flame Reynolds number Re_L is defined as in equation 2.4.

$$Re_L = \frac{u^{'} L_t}{S_{l,0} \delta_f} \tag{2.4}$$

The Damköhler number (Da) is the ratio between the integral time scale corresponding to largest eddies to the chemical time scale of the laminar flames (Poinsot and Veynante, 2005). It is defined as in equation 2.5.

$$Da = \frac{\tau_m}{\tau_c} = \frac{L_t}{u^{'}} \frac{S_{l,0}}{\delta_f} \tag{2.5}$$

The Karlovitz number is similar to Damköhler number except that it is defined for smallest eddies. It indicates the ratio between chemical time scale and Kolmogorov time scale as given in eq. 2.6.

$$Ka = \left(\frac{u^{'}}{S_{l,0}} \right)^{3/2} \left(\frac{\delta_f}{L_t} \right)^{1/2} \tag{2.6}$$

The regime for which $Re_L > 1$ characterizes the space of turbulent premixed flames. Within the turbulent premixed flame regime, the flames are categorized based on Karlovitz and Damköhler number.

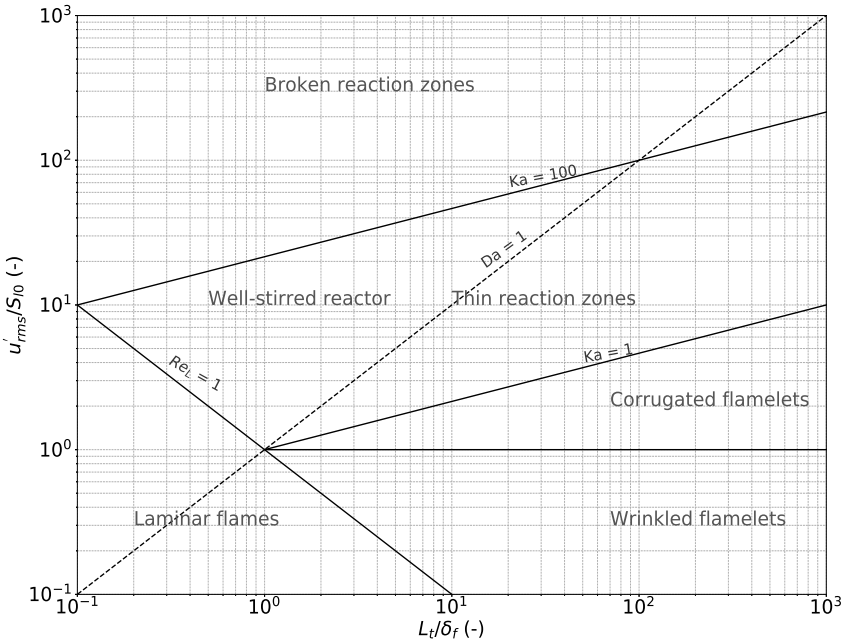

FIGURE 2.1: Regime diagram for premixed turbulent combustion based on (Peter, 1999).

When Ka is less than unity (Ka $<$ 1), the chemical time scales are smaller than the smallest turbulent time scales and the regime is called the flamelet regime. The flame front is thin and the flame structure resembles a laminar flame and the turbulent motions wrinkles the flame. Within the flamelet regime, the flames are classified according to the ratio of turbulent velocity to laminar flame speed (u'_{rms}/S_{l0}). When the turbulent fluctuation are smaller than the laminar flame speed ($u'_{rms} < S_{l0}$), the regime is called wrinkled flamelet regime and the turbulent motions are too low for flame interactions. On the other hand, when $u'_{rms} > S_{l0}$ within the flamelet regime, the turbulent motions are able to wrinkle the flame to cause flame front interactions. This leads to the formation of pockets of fresh and burnt gases. This regime is called the corrugated flamelet regime.

Flames in most practical combustion system fall under the thin reaction zone category. This regime is bounded by the lines corresponding to Ka = 1 and Ka = 100. In this regime, the Kolmogorov length scale η is smaller than the flame thickness and scalar mixing is enhanced within the preheat zone. But the reaction zone remains unaffected by the turbulence. For Ka $>$ 100, both reaction and preheat zone is affected by turbulence. This regime is called broken reaction zones.

Damköhler numbers lower than unity ($Da < 1$) means that the reactions are controlled by chemical kinetics and the flames formed falls in the well stirred reactor regime in the Borghi diagram. For large values of the Damköhler number ($Da >> 1$), the chemical time scales are smaller than turbulent mixing time and thus the reaction are controlled by mixing processes.

2.2.2. Thermo-diffusive Instabilities

Thermo-diffusive instabilities arise due to the difference between the molecular diffusion coefficient of fuel and oxidizer and molecular heat diffusivity of the mixture. For lean hydrogen flame at high preheat temperatures, this effect becomes quite significant even in presence of high turbulence in the flow. The physical mechanism behind thermo-diffusive instability

was explained by Zel'dovich (1944) in 1944. A turbulent premixed flame front is wrinkled by the turbulent eddies and forms bulges either pointing upstream towards the fresh mixture or downstream away from it as shown in figure 2.2. When the deficient reactant in the premixed mixture is light, the molecular diffusion exceeds the molecular heat diffusion. Thus the energy supplied by the faster diffusing reactants into the upstream pointing bulges increases faster than the heat is diffused from it. This results in local increase of flame speed and the bulges grow deeper into fresh mixture. On the other hand, if thermal diffusivity of the mixture is higher than molecular diffusivity of deficient reactant, the wrinkles are smoothed out.

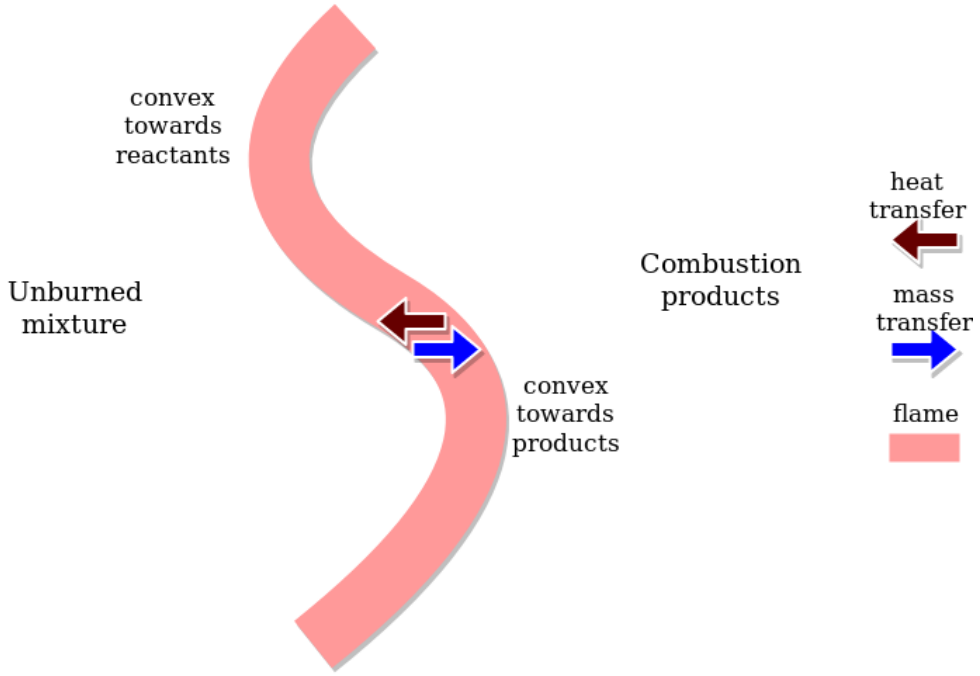

FIGURE 2.2: Turbulence-flame interactions causing stretching and wrinkling of the flame front (Siewert, 2006).

A dimensionless number representing this phenomena is the ratio of heat diffusion coefficient of the mixture $\alpha = \lambda / \rho c_p$ to the molecular diffusion coefficient D_m of the deficient reactant in the mixture (Lefebvre and Ballal, 2010).

$$Le = \frac{\alpha}{D_m} = \frac{\lambda}{D_m \rho c_p} \tag{2.7}$$

where λ is the heat conductivity, ρ is the density and c_p is the specific heat capacity at constant pressure of the mixture.

Lipatnikov and Chomiak (2005) reviewed several experimental and DNS studies showing the effect of thermo-diffusive instabilities on turbulent premixed flames. The author concluded that the turbulent flame speed increases with decreasing Lewis number and the effect is strong even in presence of high turbulence ($u' >> S_L$). These conclusion are supported by lean premixed H_2/air jet flame experiments performed by Wu et al. (1990), where the thermo-diffusive instabilities were strong at flow Reynolds number of 40000 and u'/S_l as high as 15. Similar observations were made by Nakahara and Kido (1998) in experiments with hydrocarbon and hydrogen mixtures showing strong sensitivity of turbulent flame speed to Lewis number.

2.3. Flame Flashback

Flame flashback is one of the prime challenges in premixed hydrogen flames. It is generally defined as the upstream propagation of a flame due to an imbalance in local flame velocity and flow velocity. During a flashback event, the flame propagates upstream into the premixer and changes the combustion from premixed to diffusion type. This in turn increases the temperatures, pollutants and causes considerable damage to the equipment. There are mainly four mechanisms by which undesirable combustion of premixed mixture occurs due to flashback. They are detailed below with reference to hydrogen flames.

Flame Propagation through Boundary Layer For bounded flows, the flow velocity gradually decreases towards a solid boundary due to no-slip wall. Thus it is possible that the flame speed outbalances the local flow velocity near boundaries and travel upstream unless counteracted by flame quenching. The critical distance between flat plates below which the flame cannot propagate is defined as quenching distance δ_q as shown in figure 2.4. The quenching is caused by heat losses to the combustor wall. For flames with low quenching distance, boundary layer flashback (BLF) is a real possibility. There are several possible scenarios of boundary layer flashback as depicted by Eichler (2011) in figure 2.3.

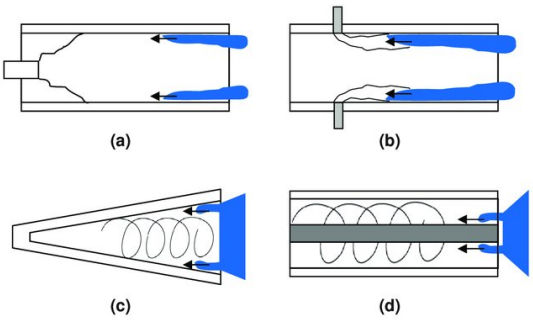

Figure 2.3: Boundary layer flashback scenarios in gas turbine burners (Eichler, 2011)

For a stable flame front at distance δ_b from the wall, the local flow velocity should be equal to flame speed (S_f). Assuming linear velocity profile near the boundary, the 'critical velocity gradient' g_c is written as proposed by (Lewis and Elbe, 1943) in equation 2.8. For a given flow, flashback occurs when the wall velocity gradient is less than g_c.

$$g_c = \frac{\partial u}{\partial y}|_{y=0} = \frac{\tau_w}{\mu} = \frac{S_f|_{y=\delta_b}}{\delta_b} \tag{2.8}$$

In the figure 2.4 δ_q is the quenching distance described above, δ_b is penetration depth and δ_f is the flame thickness. The critical velocity gradient depends on fuel-oxidizer kinetics, ϕ, T, p and T_W. Higher the g_C higher the chance for boundary layer flashback. But this

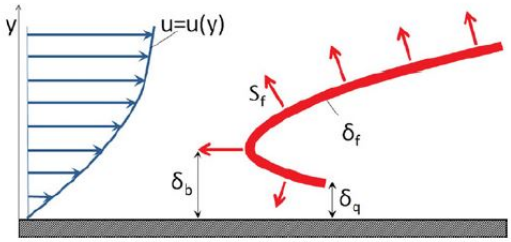

Figure 2.4: Critical velocity gradient concept (Benim and Syed, 2015b).

expression is only valid for laminar boundary layers. Turbulent critical velocity gradients are almost three times that in laminar boundary layer.

Since hydrogen flames have high velocity and low quenching distance, the flame can travel upstream to the premixer through the boundary layer (Hoferichter, Hirsch, Sattelmayer, et al., 2017). Eichler (2011) performed flashback experiments for premixed turbulent hydrogen-air flames in tube and channel flows. The author calculated the critical velocity gradient (g_c) for different equivalence ratios in unconfined and confined tube burners and channel flows. The results of the experiment is shown in figure 2.5. From the figure it is evident that g_c increases monotonically with fuel equivalence ratio. Also unconfined burners have better flashback resistance than confined burners which can be inferred from almost an order of magnitude difference in the g_c.

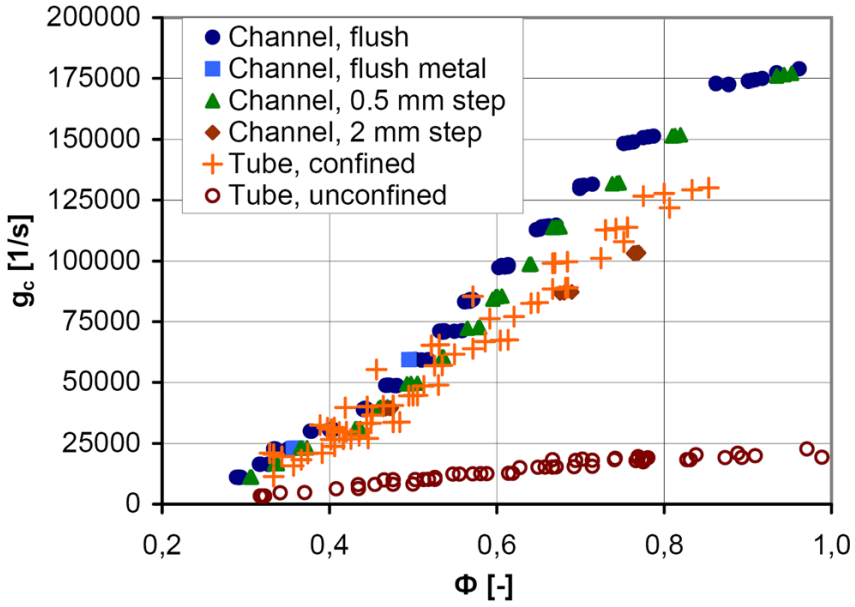

Figure 2.5: Critical velocity gradients for hydrogen air flame as a function of equivalence ratio in different tube and channel flows (Eichler, 2011).

Flame Propagation due to Combustion Instabilities Due to operating near lean blowout limits, combustion instabilities are common in lean premixed systems. Instabilities are caused fuel/air ratio oscillation and vortex shedding. Thermo-acoustic oscillations occurs because heat release fluctuation couples positively with pressure waves producing large velocity and pressure perturbations (Dowling, 1995). At high pulsation levels, significant undershoots of the burner flow velocity results. At lower frequencies of these pulsation, the flame could travel upstream through boundary layer or the core flow (O'Connor, Hemchandra, and Lieuwen, 2016).

Flame Propagation through Core Flow Turbulent flame speeds are always higher than the corresponding laminar flame speeds. Since all practical flows in a gas turbine combustor are turbulent, the turbulent flame speed increases with turbulence. When turbulent flame velocity away from the flow boundary increases above the flow velocity, flame could travel upstream into the burner. This can be caused by local enrichment of the fuel, increasing equivalence ratio in that region (Benim and Syed, 2015a) or change in flow velocities due to combustion.

Laminar flame speeds for hydrogen for $\phi = 0.3$ to 1 falls between 1 m/s and 3 m/s at atmospheric conditions. Typical air flow velocities in gas turbine burners are in the range of 50 m/s. These values suggests that turbulent flame propagation through core flow upstream is unlikely, but shouldn't be neglected Benim and Syed (2015a).

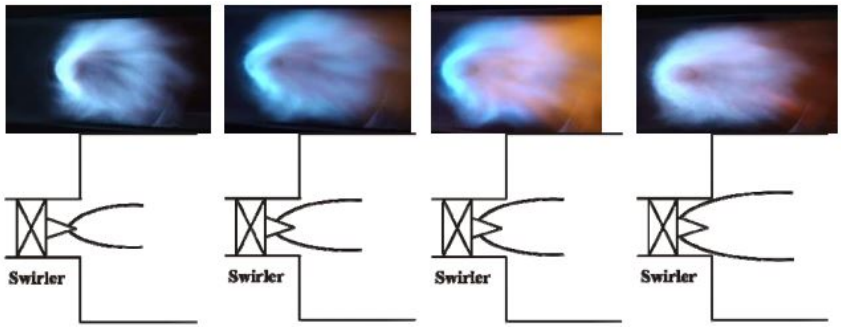

FIGURE 2.6: Sequence on CIVB driven flashback in swirl stabilized combustor (Dam et al., 2011).

Combustion Induced Vortex Breakdown In high swirl stabilized combustors, the swirling flows causes vortex breakdown which forms a central recirculation zone where flame is stabilized. Thus flashback because of combustion induced vortex breakdown (CIVB) is a type of flashback through core flow. But contrary to the previous mechanism, this is driven by interaction of heat release with swirling flow aerodynamics, leading to transition of vortex breakdown characteristics (Fritz, Kröner, and Sattelmayer, 2004). Figure 2.6 shows sequence of images showing CIVB driven flashback under unstable conditions in a swirl stabilized combustion chamber burning syngas fuel. The flame moves upstream into the premixer with increase in equivalence ratio.

Noble et al. (2006) investigated flashback and blowout effects of syngas mixture composition in a swirl stabilized combustor. For syngas mixture with hydrogen composition less than 60% slow flashback was observed which is attributed to CIVB type. Flame temperature, rather than flame speeds appeared to be the key parameter describing flashback tendency. This point towards vortex dynamics alteration by combustion. Thus increased flame speed is not a necessary condition for flashback in such combustors.

2.4. Flashback Prediction

Since flashback is a major challenge in premixed combustors, there exists several numerical and analytical methods to predict flashback in a system. Most methods are correlations based on experiments conducted at different facilities. High expenses associated with these experiments prevent testing at all gas turbine relevant conditions. Thus most methods are tested at certain laboratory conditions and extrapolated or interpolated to corresponding operating conditions of a combustor. In this section few of these prediction models are discussed.

2.4.1. Damköhler Correlation

Damköhler correlation developed by Kalantari, Sullivan-Lewis, and Mcdonell (2015) at University of California Irvine based on dimensional analysis using the Buckingham Pi theorem. The correlation is optimized for 3 bar $\leq$ p $\leq$ 8 bar, 300 K $\leq T_u \leq$ 500 K and 30 m/s $\leq U_0 \leq$ 40 m/s for hydrogen-air flames at gas turbine premixer conditions and is given by:

$$Da_{DC} = 5.79x10^{-6} Le_f^{1.68} Pe_F^{1.91} \left(\frac{T_u}{T_{u,ref}}\right)^{2.57} \left(\frac{T_B}{T_{u,ref}}\right)^{-0.49} \left(\frac{p}{p_{ref}}\right)^{-2.1} \tag{2.9}$$

where, Le_f is fuel's Lewis number, Pe_F is Peclet number based on laminar flame speed, T_B is burner tip temperature, T_u is preheating temperature and p is premixer pressure. The experimental Damköhler number is given by equation 2.10 at the experimentally determined

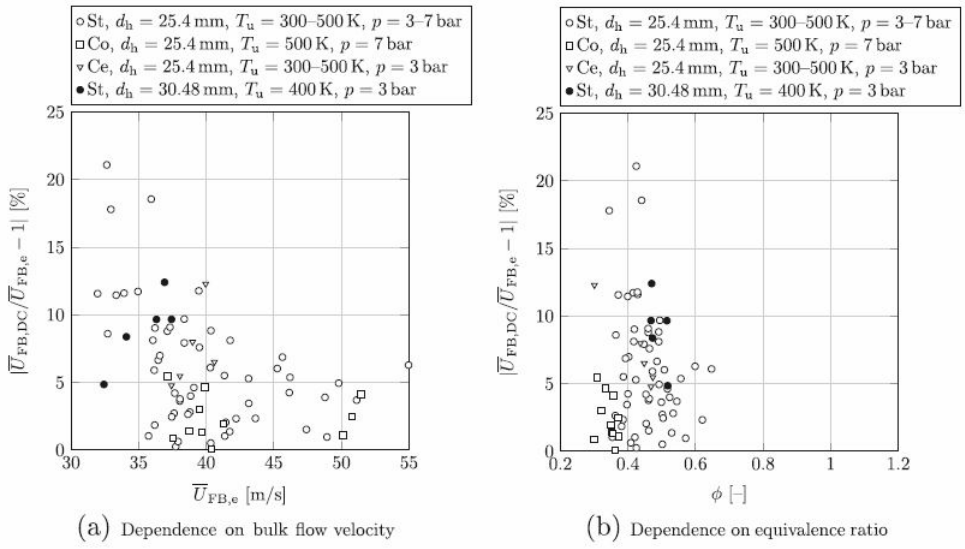

FIGURE 2.7: Prediction accuracy of Damköhler correlation. St: Stainless steel burner; Co: copper burner; Ce: ceramic burner (Hoferichter, Hirsch, Sattelmayer, et al., 2017).

flashback points.

$$Da_e = \frac{S_L^2 \rho_u c_{p,u} \nu_u}{\lambda_u u_\tau^2} \tag{2.10}$$

The shear stress velocity is calculated using the Blasius equation 2.2.

The correlation is based on flashback experiments conducted at above conditions. The prediction accuracy of Damköhler correlation is assessed in Hoferichter, Hirsch, Sattelmayer, et al. (2017) comparing predicted bulk flow velocity at flashback and measured bulk flow velocity from experiments from different burner material, as shown in figure 2.7. Damköhler correlation provides a fast way to predict flashback to reasonable accuracy at the optimized condition.

2.4.2. Hoferichter's Model

The Hoferichter's Model for confined flames was developed at TU Munich, Germany by Hoferichter, Hirsch, and Sattelmayer (2016) and is based on onset of flashback in the event of boundary layer separation upstream of flame tip. According to this idea, the flashback is predicted by calculating the minimum pressure rise upstream of flame tip which causes flow separation (Hoferichter, Hirsch, and Sattelmayer, 2016). The author used Stratford's criteria to predict boundary layer separation due to pressure rise upstream induced by flame. The model is detailed in appendix A.

The model calculated the free flow velocity needed to prevent flashback known as the flashback resistance velocity (U_{FB}). The prediction model was validated with experimental flashback studies conducted by Eichler (2011) for premixed hydrogen air in rectangular channel at different preheating temperatures. The comparison of model predicted flashback limits and that obtained from experiments is shown in figure 2.8. Although Hoferichter's Model gave excellent prediction of flashback velocity at room temperature, at higher temperature, large deviations were observed.

2.4.3. Tober's Model

Tober (2019) devised an improved model based on Hoferichter's model. The original model was modified for flame instabilities and flame stretch effects. An improved equation for turbulent

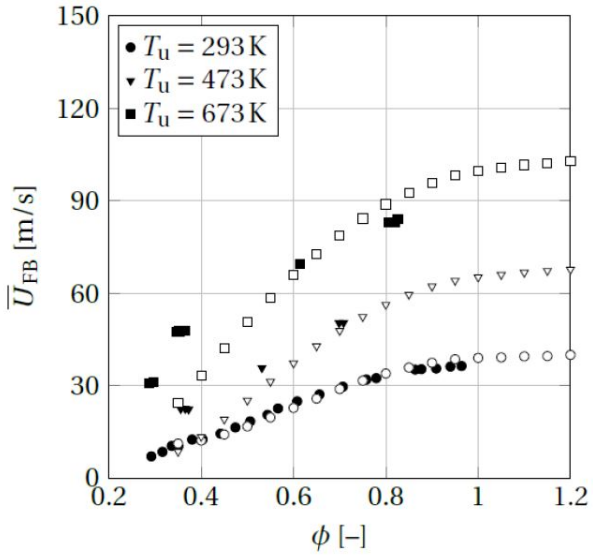

FIGURE 2.8: Validation of predicted velocity at flashback with experimental data at atmospheric conditions for channel flow. Filled symbols : experimental data; Empty symbols : predicted values (Hoferichter, Hirsch, and Sattelmayer, 2016).

flame speed was derived to include all the aforementioned effects. While calculating flame stretch effects, Hoferichter assumed the turbulence to be isotropic and neglected the flame stretch due to anisotropic stresses. The effects of anisotropic stresses are modelled in Tober's model. The flame instabilities caused by thermo-diffusive instabilities are modelled here. Thus the preferential diffusion effects in lean premixed hydrogen-air combustion is modelled into the turbulent flame speed. Results from the improved flashback velocity prediction model is given in figure 2.9.

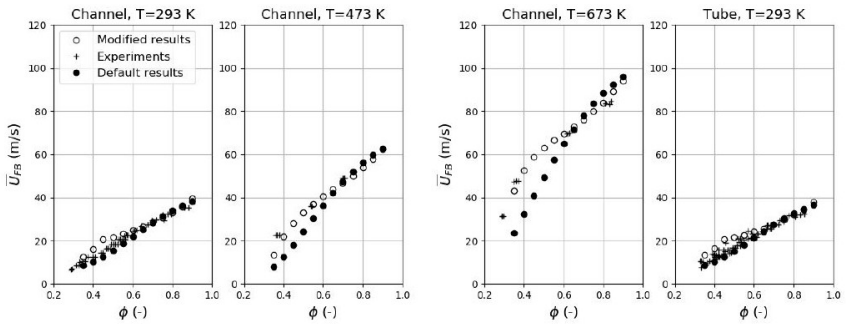

FIGURE 2.9: Predicted flashback velocity with Tober's model compared with experiments (Eichler, 2011). Original results - Hoferichter's model; Modified results - Tober's model

2.4.4. Lin's prediction model

Lin (2014) proposed a flashback prediction model for hydrogen rich gas and syngas flames based on the critical velocity gradient of the flame. An empirical correlation was proposed for the calculation of the critical velocity gradient of the flame based on a characteristic velocity and characteristic length scale.

At critical condition of flashback, the flame propagation through the boundary layer is facilitates by the high turbulent flame speed. Thus the characteristic velocity is selected

as the flame turbulent flame speed (S_T). There are various length scales such as penetration depth (δ_b), quenching distance (δ_q) which are associated with a bounded flame. These lengths have the same order of magnitude as the laminar flame thickness (δ_f) (Wohl, 1953). Thus the characteristic length scale is selected as the laminar flame thickness, δ_f. The final empirical formula for the flame critical velocity gradient is given in equation 2.11.

$$g_c = \frac{S_T}{Le\delta_f} \tag{2.11}$$

The Lewis number is included in the denominator to capture the increase in critical velocity gradient with decrease in Lewis number.

The flow velocity gradient (g_f) is estimated using the Blasius correlation eq. 2.3. Boundary layer flashback occurs when the critical velocity gradient exceeds the flow velocity gradient or when $g_c > g_f$. The equation is validated with experiments performed by the author for hydrogen rich fuel gases. Figure 2.10 shows the variation of critical velocity gradient with equivalence ratio at different inlet pressure for $H_2 - N_2$ (85-15 by %vol) mixture for preheat temperature of 623 K.

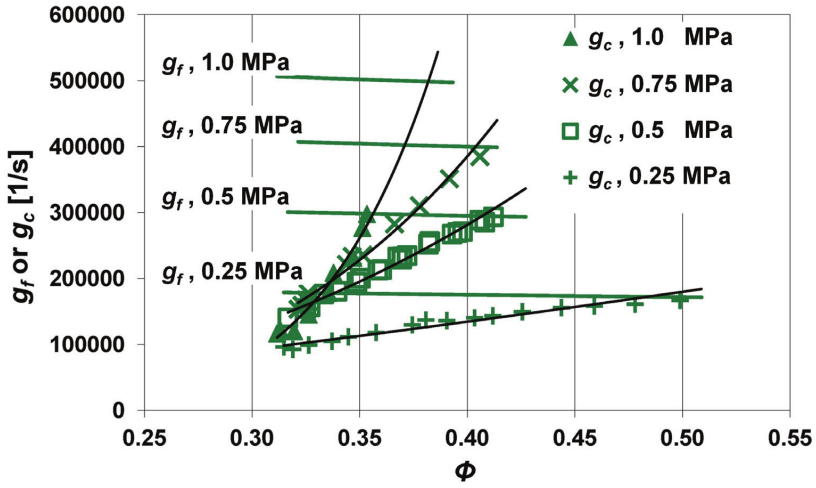

FIGURE 2.10: Flow velocity gradient g_f and critical velocity gradient g_c (symbols) against ϕ for $H_2 - N_2$ (85-15 by %vol) at $T_u = 623$ K.

The green lines represent the flow velocity gradient and the black lines represent the critical velocity gradient of the flame. The lines intersect at the flashback point estimated from the experiment at all pressure conditions except at 1.0 MPa.

2.5. Combustor Concepts

Even though the potential of hydrogen as a gas turbine fuel has been known for decades, it is recently that the power generation sector started looking for options to use hydrogen as an alternative fuel for premixed gas turbine combustion. Several experiments and numerical studies were conducted to analyze the behaviour of hydrogen rich fuels in premixed combustors. Earlier studies were focused on adapting conventional swirl stabilized combustors to operate with syngas and mixtures of natural gas and hydrogen. The transition towards 100% hydrogen as fuel for premixed combustion in gas turbine combustors was retarded by the challenge of flame flashback.

This section is a review of different burner concepts capable of burning hydrogen rich fuel at lean premixed conditions. For each burner design, information from relevant

experimental and numerical studies at operating conditions similar to OPRA Turbine operating conditions are presented.

2.5.1. High Swirl Burners

High swirl burners are actively used for burning natural gas and other conventional fuels in premixed mode. Recent studies have focused on preventing flashback in high swirl burners operating with hydrogen rich fuel gases. Lam, Geipel, and Larfeldt (2014) tested the Siemens SGT-400 DLE combustion system at atmospheric condition using hydrogen enriched natural gas. The author observed that the addition of hydrogen increased the NOx emissions due to chemical kinetic and higher temperatures. H_2 addition also increased the gas flammability and reactivity. This resulted in a decrease in flame blowout temperature and stable operation was achieved for hydrogen content up-to 80% by vol. A similar test was performed at high pressure conditions by Lam and Parsania (2016). Compared to the previous test, at high pressure conditions the system could only operate without flashback for up to 20% by vol of hydrogen.

Reichel, Terhaar, and Paschereit (2018) used axial air injection to mitigate flashback for 100% hydrogen fuel at 1 atm pressure and temperatures up to 673 K. The burner setup used is shown in figure 2.11. Even though axial air injection reduced flashback due to vortex breakdown, it had a negative effect on boundary layer flashback.

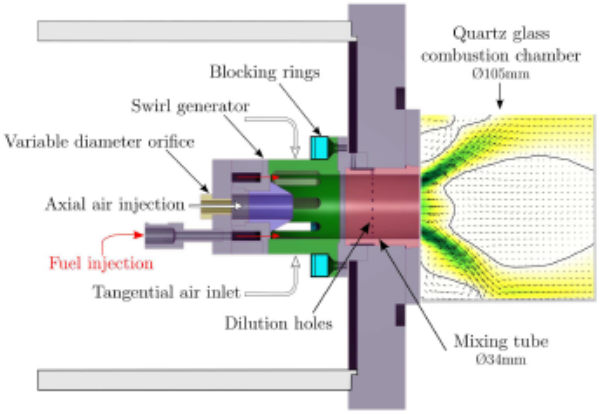

FIGURE 2.11: High swirl burners with axial air injection (Reichel, Terhaar, and Paschereit, 2018)

2.5.2. Low Swirl Burners

R.K Cheng et al. (2000) developed low swirl based burner for gas turbine applications. The low swirl flow causes a divergence field at the burner exit. This causes a reduction in flow velocity, where the flame is stabilized as shown in figure 2.12. The low residence time of the low swirl flame is advantageous for ultra low NO_x emissions. Laboratory experiments were conducted on the burner at gas turbine conditions and the behaviour was studied by R.K. Cheng et al. (2009). The low swirl burner was observed to have slightly better flashback resistance than high swirl burner for hydrogen rich fuels. For hydrogen content above 60% by vol in methane, a shift in stabilization mechanism was observed.

Johnson et al. (2005) compared the flow fields and emissions of high swirl and low swirl burners. The burners were tested at gas turbine relevant conditions of 0.08-2.2 MW ($20 < U_0 < 50$m/s, $230 < T_0 < 430^o$ C, $6 < P_0 < 15$ atm) for natural gas. The reduction in residence time in the flame reflected in a 60% reduction in NO_x emissions compared to HSB without compromise in CO emissions. Similar studies for H_2-CH_4 flames found the stabilization mechanism changing with increasing hydrogen composition in the fuel (R.K. Cheng et al.,

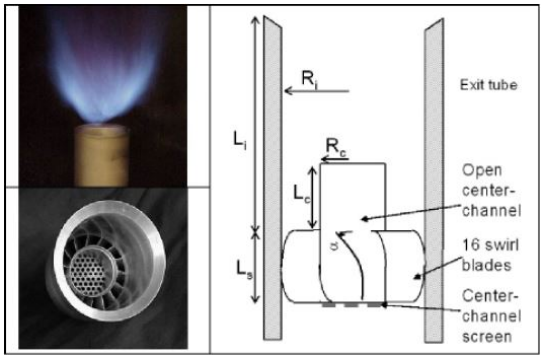

FIGURE 2.12: Low swirl burner cross section view and detached methane flame (Littlejohn et al., 2007).

2009). Beerer et al. (2013) studied temperature, pressure and flow velocity dependence of H_2 flames in low swirl burners. Their findings revealed that flashback resistance increased with preheat temperature and burner flow velocity but decreased with pressure and adiabatic flame temperature. The dependence is depicted in figure 2.13. The figure shows the adiabatic flame temperature at flashback for different conditions. Higher pressure ratio increases the final inlet temperature of the mixture to the combustor chamber. Since increasing pressure decreases flashback resistance, in this case the detrimental effect is somewhat mitigated by increase in inlet temperature.

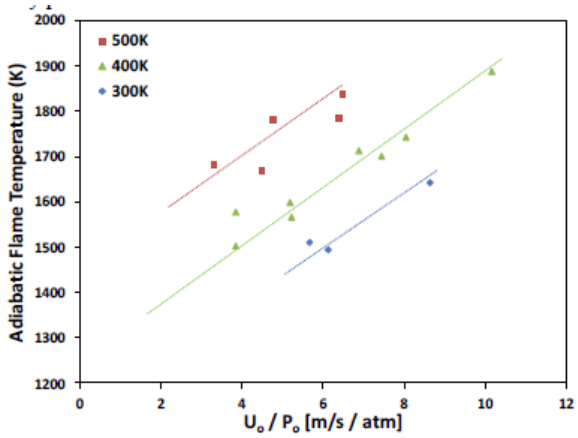

FIGURE 2.13: Flashback resistance curve (Beerer et al., 2013)

2.5.3. Micromix Injector

Micromix injector are based on multi-point injection, multi-burning zone concept. Multiple micro mixing cups eliminate the need for large scale spatial mixing, thereby reducing residence time needed to achieve adequate mixing for ultra low emission combustion. Micromix injector consists of multiple straight tubes of millimeter scale diameter arranged in a parallel array. The incoming compressed air is split among the tubes and fuel is added through sub-millimeter holes into each of these tubes. The fuel injected in a jet-in-crossflow fashion mixes with the oxidizer stream and exits as a fully premixed jet. The location, diameter and number of holes of both air and fuel injector tubes are carefully designed and optimized so as to prevent flashback.

D. York, S. Ziminsky, and Yilmaz (2012) tested the multi tube mixer in a small scale single nozzle rig at GE's F-class gas turbine conditions. A sectioned model view and photograph of the single nozzle used for rig test is shown in figure 2.14. With a pressure

drop of 3-5% across the premixer, flashback free stable operation was achieved for flame temperatures of over 1900K with 60%H_2 - 40% N_2 fuel. The full can NO_x emissions for the same fuel composition were below 10 ppm. Funke et al. (2013) investigated NO_x emissions

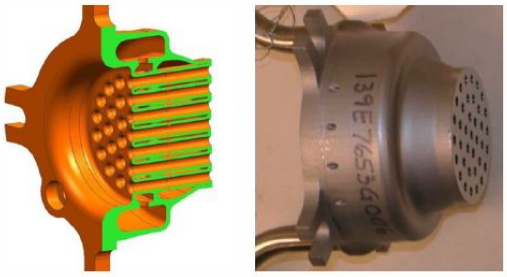

FIGURE 2.14: Cross section and photograph of multitube mixer injector for high hydrogen fuels (D. York, S. Ziminsky, and Yilmaz, 2012).

and flame stabilization in diffusion type micromix combustors. The injection and cross flow mixing schematics is shown in figure 2.15a. They compared NO_x emissions of micromix burners with lifted and attached flames as shown in figure 2.15b. Achieving low emissions in micromix burners requires deep understanding of mixing patters, residence time and flame stabilization in-order to optimize them.

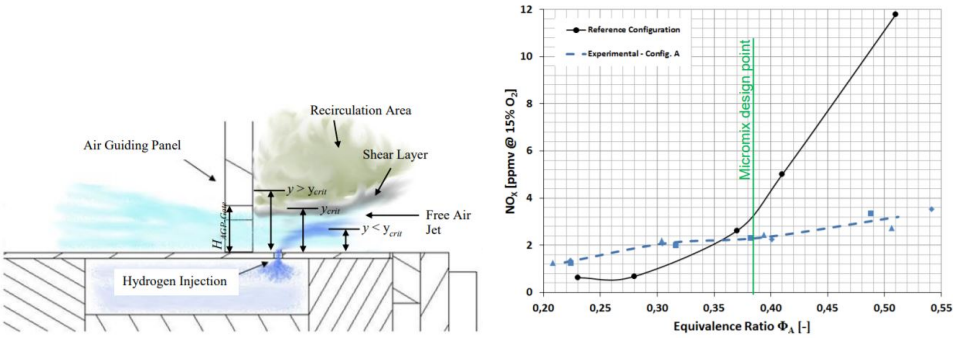

(A) Schematics of injection and cross flow mixing in micromix burners.

(B) NO_x emissions for attached flames (Reference configuration) and lifted flames (Configuration A).

FIGURE 2.15: Injection schematics and NO_x emissions for micromix burners (Funke et al., 2013).

2.5.4. Aerodynamically Trapped Vortex Combustor

The Aerodynamically Trapped Vortex (ATV) Combustor is a subset of the trapped vortex combustor concept. The trapped vortex combustor (TVC) makes use of cavities to stabilize a flame as shown in figure 2.16. For a proper cavity design, a large rotating vortex is formed in the cavity. The cavity is formed by two bluff bodies. The vortex can be locked or stabilized inside the cavity by injecting fuel in the right direction into the cavity or from the premixer. Since the flame is anchored away from the main flow, stable combustion can be achieved in high speed flow applications.

The FlameSheet^{TM} combustor shown in figure 2.17, invented by Ansaldo Power Systems Mfg in 2002 is based on the trapped vortex combustion concept. It is also known as combustor within a combustor due to the presence of two main reaction zones. The combustor makes use of aerodynamically trapped vortex for flame stabilization instead of bluff bodies. Near the boundary of the liner, a 180^o turn in the flow through a combustor dome causes

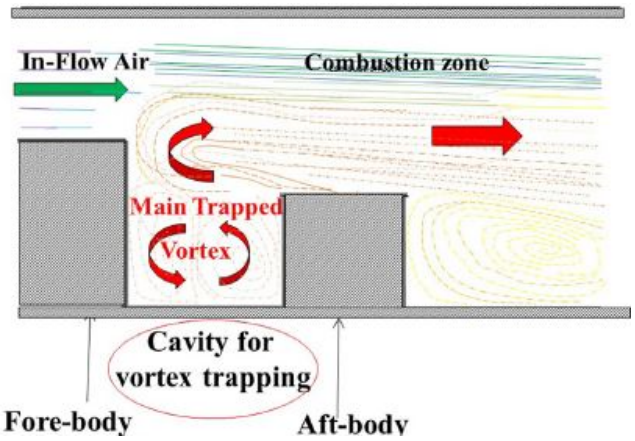

FIGURE 2.16: Schematic of trapped vortex combustion (Zhao, Gutmark, and Goey, 2018).

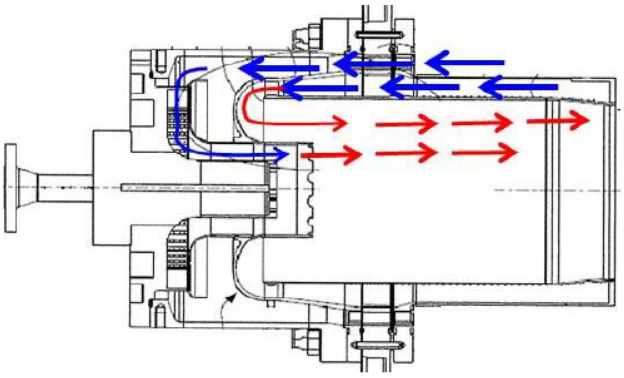

FIGURE 2.17: Overall flow design of FlameSheet^{TM} combustor P. Stuttaford et al., 2016

separation of the flow from the liner edge and creates a trapped vortex (Peter J Stuttaford et al., 2005). The trapped vortex anchors the flame similar to a backward facing step combustor by recirculating hot combustion product to provide enhanced stability. Figure 2.18 shows the flame stabilization mechanism in the FlameSheet^{TM} combustor. Equivalent point 1 corresponds to point of separation and equivalent point 2 corresponds to flow reattachment to the combustor liner (P. Stuttaford et al., 2016). The vortex is formed between the space enclosed by these points. For a fixed geometry, the strength of the vortex and the reattachment length depends on factors such as inlet flow velocity and turbulence levels within the combustor. The velocity and temperature contours from reactive CFD simulations performed by P. Stuttaford et al. (2016) is shown in figure 2.19.

P. Stuttaford et al. (2016) conducted tests on General Electric 7FA heavy duty gas turbine retrofitted with the FlameSheet^{TM} combustor at F-class base load operating conditions ($\dot{m} = 27 kg/s$, $P_0 = 24$ bar, $T_0 = 920$ K). In the tests fuels with hydrogen content up-to 65% by vol were successfully tested without flashback. NO_x and CO emissions were found to be lower than 6 ppmv (15% O_2) as shown in figure 2.20a and 2.20b respectively.

Burner concepts based on trapped vortex flame stabilization are better suited for hydrogen fuel operation. The high flow velocities can be used in the combustor which could counter high flame speeds. Apart from the experiments by P. Stuttaford et al. (2016) and Rizkalla et al. (2018) there are no extensive studies on FlameSheet^{TM} type combustors that have been externally published. For adopting this concept in a gas turbine combustor a thorough understanding of flame stabilization, flame flashback mechanism, emissions among

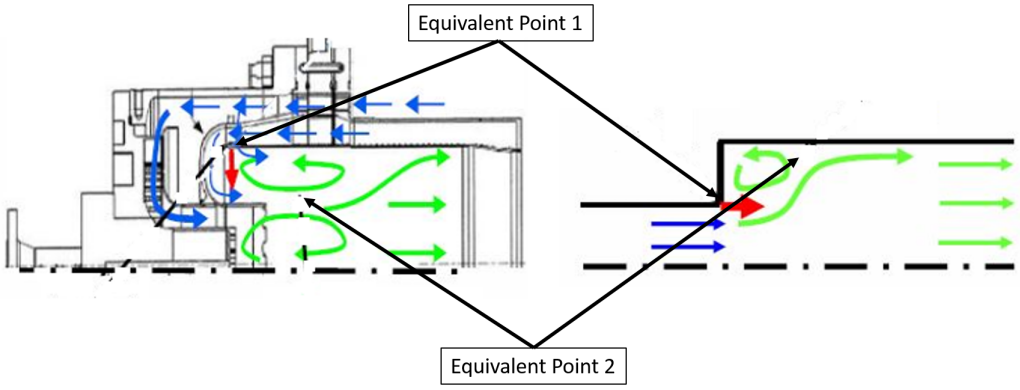

FIGURE 2.18: Illustration of flame stabilization in FlameSheet^{TM} combustor (P. Stuttaford et al., 2016).

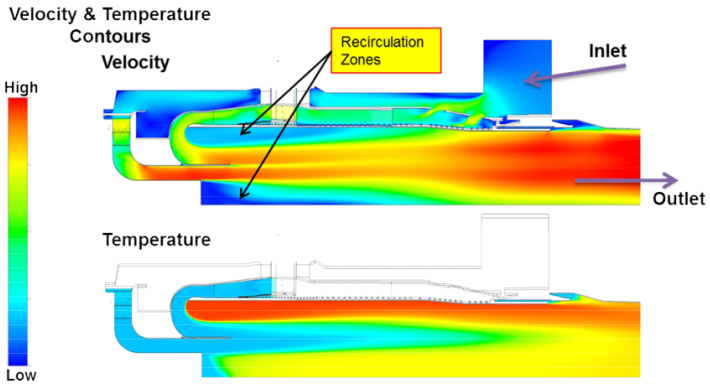

FIGURE 2.19: Qualitative velocity and temperature contours from reactive CFD simulations P. Stuttaford et al. (2016).

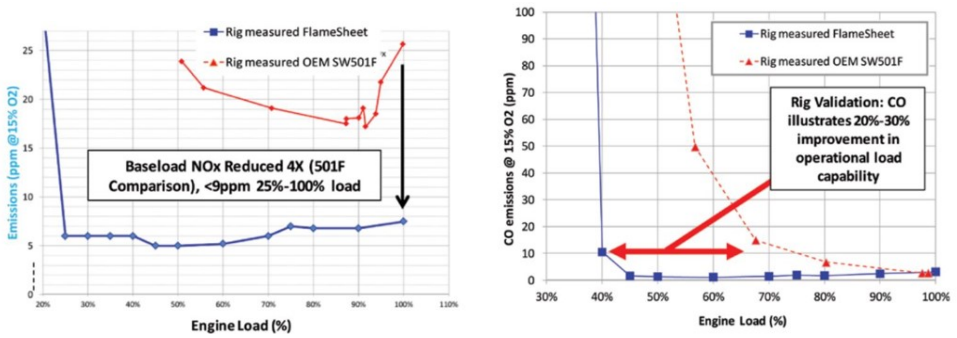

(A) NO_x emissions comparison - FlameSheet^{TM} and OEM combustor. (B) CO emissions comparison - FlameSheet^{TM} and OEM combustor.

FIGURE 2.20: Emission measurements of FlameSheet^{TM} combustor (Varley, 2017).

other characteristics is required.

2.6. Computational Methods

All realistic flows in a combustion chamber are turbulent with complex chemical reactions. Even though experimental results are considered more reliable, costs and time required only

allow few experimental studies. Therefore computational methods are used to analyze design iterations at relevant conditions. First, the methods to capture the turbulence are discussed and different models to capture the reaction chemistry. All the models are discussed with respect to simulating hydrogen flames in combustors.

In industries, popular ways to capture turbulence is by Reynolds Averaged Navier-Stokes (RANS) models and Large Eddy Simulation (LES). RANS models are based on averaging the turbulence field to extract the mean flow characteristics. As a result of averaging, there are unclosed fluctuations terms called Reynolds stress terms which need modelling. Contrary to RANS models, LES resolves part of the turbulence and models the rest. Large scale eddies are resolved with sufficient accuracy and the smaller ones are modelled using relations based on the resolved turbulence.

2.6.1. Reynolds Averaged Navier Stokes of Premixed Flames

The physics of non reacting compressible flows is governed by continuity, momentum and energy conservation equations. For three dimensional compressible flows in Cartesian coordinates the mass , momentum and energy equations are given by equations 2.12, 2.13 and 2.14 respectively.

Mass

$$\frac{\partial \rho}{\partial t} + \frac{\partial \rho u_i}{\partial x_i} = 0 \tag{2.12}$$

Momentum

$$\frac{\partial}{\partial t}\rho u_j + \frac{\partial}{\partial x_i}\rho u_i u_j = -\frac{\partial p}{\partial x_j} + \frac{\partial \tau_{ij}}{\partial x_i} \tag{2.13}$$

Energy

$$\frac{\partial \rho h}{\partial t} + \frac{\partial}{\partial x_i}\rho u_i h = \frac{Dp}{Dt} + \frac{\partial}{\partial x_i}(\lambda \frac{\partial T}{\partial x_i}) + \tau_{ij}\frac{\partial u_i}{\partial x_j} \tag{2.14}$$

Compared to non reacting flow equations, combustion adds N-1 (N is number of species in the reaction) number of equations to the set of governing equations. The contribution of energy released from the chemical reactions is added to the energy equation. The species conservation equation is given in equation 2.15 and the new energy conservation equation in equation 2.16. Solving for species conservation equations adds significant computational effort to already computationally intensive task of resolving turbulence.

The transport equation for the mass fraction Y_r of species p in a multi-component reacting system is given by:

$$\frac{\partial \rho Y_r}{\partial t} + \frac{\partial}{\partial x_i}(\rho u_i Y_r) = -\frac{\partial J_{r,j}}{\partial x_i} + \dot{\omega}_r \tag{2.15}$$

where $J_{r,j} = -\rho D_{Y_r}\frac{dY_r}{dx_i}$ denotes the diffusion flux of species r and $\dot{\omega}_r$ is the volumetric reaction rate of species r in the mixture.

The updated energy equation for reacting flows is given by:

$$\frac{\partial \rho h}{\partial t} + \frac{\partial}{\partial x_i}(\rho u_i h) = \frac{Dp}{Dt} - \frac{\partial}{\partial x_i}(\lambda \frac{\partial J_{q,i}}{\partial x_i}) + \tau_{ij}\frac{\partial u_j}{\partial x_i} + \dot{Q} \tag{2.16}$$

where $\dot{Q}$ is the heat source term due to electrical spark or radiation flux and $J_{q,i} = -\lambda\frac{\partial T}{\partial x_i} + \sum_{r=1}^{N} h_r J_{r,j}$ represents the energy flux.

To reduce computational cost the turbulence is modelled using RANS models and the governing equations are averaged. In the RANS approach, any vector, scalar or tensor

quantities are decomposed into its mean and fluctuating component. The average of the fluctuating component is zero. For variable density flows, Reynolds averaging of density fluctuation terms introduces more unclosed terms (De, Agarwal, et al., 2017). Therefore Favre averaging is used for a quantity f given by,

$$\widetilde{f} = \frac{\overline{\rho f}}{\overline{\rho}} \tag{2.17}$$

Using the Favre formulation for averaging quantities, the averaged conservation equations are given below.

Favre averaged mass conservation:

$$\frac{\partial \overline{\rho}}{\partial t} + \frac{\partial \overline{\rho}\widetilde{u}_i}{\partial x_i} = 0 \tag{2.18}$$

Favre averaged species conservation: For r = 1 to N-1:

$$\frac{\partial \overline{\rho}\widetilde{Y}_r}{\partial t} + \frac{\partial}{\partial x_i}\left(\overline{\rho}\widetilde{u}_i\widetilde{Y}_r\right) = \frac{\partial}{\partial x_i}\left(\overline{\rho D_{Y_r}}\widetilde{\frac{\partial Y_r}{\partial x_i}} - \overline{\rho}\widetilde{u_i^{"}Y_r^{"}}\right) + \overline{\dot{\omega}_r} \tag{2.19}$$

Favre averaged momentum conservation:

$$\frac{\partial}{\partial t}\overline{\rho}\widetilde{u}_j + \frac{\partial}{\partial x_i}\overline{\rho}\widetilde{u}_i\widetilde{u}_j = -\frac{\partial \overline{r}}{\partial x_j} + \frac{\partial\left(\overline{\tau}_{ij} - \overline{\rho}\widetilde{u_i^{"}u_j^{"}}\right)}{\partial x_i} \tag{2.20}$$

The term $-\overline{\rho}\widetilde{u_i^{"}u_j^{"}}$) is known as Reynolds stress. These terms are either solved using transport equations or modelled using turbulent viscosity hypothesis.
Favre averaged energy conservation:

$$\frac{\partial \overline{\rho}\widetilde{h}}{\partial t} + \frac{\partial}{\partial x_i}\overline{\rho}\widetilde{u}_i\widetilde{h} = \frac{\overline{Dp}}{Dt} + \frac{\partial}{\partial x_i}\left(\overline{\rho}\alpha\widetilde{\frac{\partial h}{\partial x_i}} - \overline{\rho}\widetilde{u_i^{"}h^{"}}\right) + \overline{\tau_{ij}\frac{\partial u_i}{\partial x_j}} + \overline{\dot{Q}} \tag{2.21}$$

2.6.2. Turbulence Modelling

The unclosed Reynolds stress terms in the Reynolds equations needs to be modelled using turbulence models. The turbulence is modelled using turbulent viscosity hypothesis or from modelled Reynolds-stress transport equations. In the turbulent viscosity assumption proposed by Boussinesq (Hinze, 1975), the Reynolds stress terms are modelled as given in equation 2.22.

$$-\overline{\rho}\widetilde{u_i^{"}u_j^{"}} = \mu_t\left(\frac{\partial \widetilde{u}_i}{\partial x_j} + \frac{\partial \widetilde{u}_j}{\partial x_i} - \frac{2}{3}\delta_{ij}\frac{\partial \widetilde{u}_k}{\partial x_k}\right) + \frac{2}{3}\overline{\rho}\widetilde{k}\delta_{ij} \tag{2.22}$$

where $\widetilde{k} = \frac{1}{2}\widetilde{u_k^{"}u_k^{"}}$. The turbulence viscosity μ_t is obtained with algebraic relations or from modelled quantities such and turbulent kinetic energy (k) and its dissipation rate (ϵ). On the other hand RSM turbulence models solves transport equation for each component of the Reynolds stress tensor.

Similar to equation above, the turbulent fluxes of scalars, $\widetilde{\overline{\rho}u_i^{"}Y_k^{"}}$ and $\widetilde{\overline{\rho}u_i^{"}h^{"}}$ are modelled using gradient assumptions given in equation 2.23 and 2.24 respectively.

$$\widetilde{\overline{\rho}u_i^{"}Y_r^{"}} = -\frac{\mu_t}{Sc_t}\frac{\partial \widetilde{Y}_k}{\partial x_j} \tag{2.23}$$

$$\widetilde{\overline{\rho}u_i^{"}h} = -\frac{\mu_t}{Pr_t}\frac{\partial \widetilde{h}}{\partial x_j} \tag{2.24}$$

where Sc_t and Pr_t are the turbulent Schmidt number and Prandtl number respectively.

Standard $k-\epsilon$ turbulence model

$k-\epsilon$ turbulence models are the most common RANS models used in Computational Fluid Dynamics (CFD) for industrial flow simulations. It is a two equation model that models the turbulence based on two quantities - turbulent kinetic energy (k) and turbulent dissipation rate (ϵ). In this model, the turbulent viscosity is based on these two quantities and is given by equation 2.25.

$$\mu_t = \rho C_\mu \frac{k^2}{\epsilon} \tag{2.25}$$

where $C_\mu = 0.09$ is a model constant. The transport equation for k and ϵ are given in equations 2.26 and 2.27.

$$\frac{\partial(\rho k)}{\partial t} + \frac{\partial(\rho k u_i)}{\partial x_i} = \frac{\partial}{\partial x_j}\left[\left(\mu + \frac{\mu_t}{\sigma_k}\right)\frac{\partial k}{\partial x_j}\right] + P_k + P_b - \rho\epsilon - Y_m + S_k \tag{2.26}$$

$$\frac{\partial(\rho \epsilon)}{\partial t} + \frac{\partial(\rho \epsilon u_i)}{\partial x_i} = \frac{\partial}{\partial x_j}\left[\left(\mu + \frac{\mu_t}{\sigma_\epsilon}\right)\frac{\partial \epsilon}{\partial x_j}\right] + C_{1\epsilon}\frac{\epsilon}{k}\left(P_k + C_{3\epsilon}P_b\right) - C_{2\epsilon}\rho\frac{\epsilon^2}{k} + S_\epsilon \tag{2.27}$$

where P_k represents the production of turbulence due to mean velocity gradients,

$$P_k = -\rho\overline{u_i' u_j'}\frac{\partial u_i}{\partial x_i} = \mu_t S^2 \tag{2.28}$$

S is the modulus of the mean rate of strain tensor.

$$S = \sqrt{2S_{ij}S_{ij}} \tag{2.29}$$

P_b is the effect of buoyancy on turbulence production,

$$P_b = g_i \frac{\mu_t}{Pr_t}\frac{\partial T}{\partial x_i} \tag{2.30}$$

g_i is the gravitational component in i-direction and the turbulent Prandtl number, Pr_t is 0.85.

Y_M is the contribution of fluctuating dilatation in compressible turbulence to the dissipation rate.

$$Y_M = 2\rho\epsilon M_t^2 \tag{2.31}$$

with turbulent Mach number $M_t = \sqrt{\frac{k}{a^2}}$, where a is the sound speed.

S_k and S_ϵ are the source terms for turbulent kinetic energy and dissipation rate equations respectively defined by the user. The constant used in the equation are fixed and are given in table 2.1.

k-ϵ-ζ-f turbulence model

Hanjalic, Popovac, and Hadžiabdić (2004) proposed a two equation eddy-viscosity turbulence model called k-ζ-f model based on Durbin's elliptic relaxation concept (Durbin, 1991) which

C_μ	$C_{\epsilon 1}$	$C_{\epsilon 2}$	$C_{\epsilon 3}$	σ_k	σ_ϵ
0.09	1.44	1.92	0.8	1	1.3

TABLE 2.1: Value of constants in the $k-\epsilon$ model (Wilcox et al., 1998).

eliminated the need for empirical damping functions near the wall. According to Durbin (1991), it is the cross stream velocity v that is responsible for turbulent transport in a boundary layer flow. Thus the correct expression for turbulent viscosity becomes:

$$\mu_t = \rho C_\mu \frac{v^2 k}{\epsilon}$$

To improve the numerical stability of of the original $\overline{v^2}-f$ model, the transport equation is solved for velocity scale ratio $\zeta = \frac{\overline{v^2}}{k}$ instead of velocity scale $\overline{v^2}$. Thus the the expression for turbulent viscosity becomes:

$$\mu_t = \rho C_\mu \frac{\zeta k^2}{\epsilon}$$

The transport equations for the $k-\zeta-f$ model is given in equations 2.32 - 2.37.

$$\rho \frac{Dk}{Dt} = \rho(P_k - \epsilon) + \frac{\partial}{\partial x_j}\left[\left(\mu + \frac{\mu_t}{\sigma_k}\right)\frac{\partial k}{\partial x_j}\right] \tag{2.32}$$

$$\rho \frac{D\epsilon}{Dt} = \rho\frac{(C^*_{\epsilon 1}P_k - C_{\epsilon 2}\epsilon)}{T} + \frac{\partial}{\partial x_j}\left[\left(\mu + \frac{\mu_t}{\sigma_k}\right)\frac{\partial \epsilon}{\partial x_j}\right] \tag{2.33}$$

$$\rho \frac{D\zeta}{Dt} = \rho f - \rho\frac{\zeta}{k}P_k + \frac{\partial}{\partial x_j}\left[\left(\mu + \frac{\mu_t}{\sigma_\zeta}\right)\frac{\partial \zeta}{\partial x_j}\right] \tag{2.34}$$

where the following form of the f equations as adopted

$$f - L^2\frac{\partial^2 f}{\partial x_j \partial x_j} = \left(C_1 + C_2\frac{P_k}{\zeta}\frac{2/3-\zeta}{T}\right) \tag{2.35}$$

where the turbulent time scale T and length scale L is given by,

$$T = max\left(min\left(\frac{k}{\epsilon}, \frac{a}{\sqrt{6}C_\mu|S|\zeta}\right), C_T\left(\frac{\nu}{\epsilon}\right)^{1/2}\right) \tag{2.36}$$

$$L = C_L max\left(min\left(\frac{k^{3/2}}{\epsilon}, \frac{k^{1/2}}{\sqrt{6}C_\mu|S|\zeta}\right), C_\eta\frac{\nu^{3/4}}{\epsilon^{1/4}}\right) \tag{2.37}$$

An additional modifications to the ϵ equation is in the constant $C_{\epsilon 1}$ being dampened close to the wall with equation 2.38

$$C^*_{\epsilon 1} = C_{\epsilon 1}\left(1 + 0.045\sqrt{1/\zeta}\right) \tag{2.38}$$

The values of the constants used in the model is given in table 2.2.

In validation studies performed by Hanjalic, Popovac, and Hadžiabdić (2004), the $k-\zeta-f$ model produced satisfactory results for backward facing step flow experiment by C. Vogel and K. Eaton (1985). The velocity profiles at different axial locations are shown in figure 2.21.

C_μ	$C_{\epsilon 1}$	$C_{\epsilon 2}$	C_1	C_2	σ_k	σ_ϵ	σ_ζ	C_T	C_L	C_η
0.22	1.4	1.9	0.4	0.65	1	1.3	1.2	6.0	0.36	85

TABLE 2.2: Value of constants in the $k-\zeta-f$ model (Hanjalic, Popovac, and Hadžiabdić, 2004).

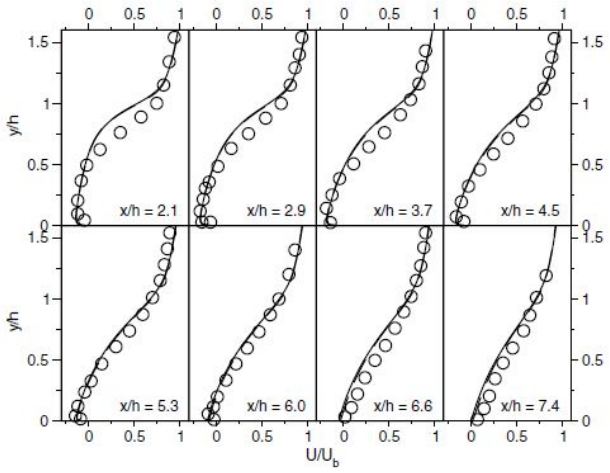

FIGURE 2.21: Velocity profiles in a backward-facing step flow (Re = 28000). Symbols: experiments by C. Vogel and K. Eaton (1985). Full line: k-ζ-f model

2.6.3. Combustion Model

The unclosed Reynolds stress terms in the Navier Stokes equation can be modelled using any of the eddy-viscosity models or Reynolds Stress Models (RSM). A combustion model aims at modelling the average volumetric reaction rate of each species, $\overline{\dot{\omega}_k}$.

In this work the combustion is modelled using FIRE^{TM} detailed chemistry solver. The solver reads the chemical mechanisms in CHEMKIN format. The effect of chemistry is considered in a way that at the beginning of each FIRE^{TM} time step Δ_t a single zone 0D reactor model is called for each computational cell. Based on the results of this model FIRE^{TM} calculates the source terms for the species transport equations and the enthalpy equation. To include the effects of turbulence chemistry interaction (TCI), additional TCI models can be coupled with the solver. To reduce chemistry computational time, the multi-zone method is employed.

The rate of production of species r is given by equation 2.39:

$$\dot{\omega}_r = \sum_{i=1}^{I} \nu_{ri} \cdot \dot{q}_i \tag{2.39}$$

where ν_{ri} is the stoichiometric coefficient of species r in reaction i and the reaction rate $\dot{q}_i$ of reaction i is defined by equation 2.40:

$$\dot{q}_i = k_R \cdot \prod_{r=1}^{N} [c_{r,g}]^{\nu_{ri}} \tag{2.40}$$

where $c_{r,g}$ is the concentration of species r in gas g given by ideal gas equation 2.41,

$$c_{r,g} = X_{r,g} \cdot \frac{p_g}{R \cdot T_g} \tag{2.41}$$

where $X_{r,g}$ is the mole fraction of species r in gas g, p_g and T_g are the total pressure of gas and the temperature of the gas respectively. The reaction rate constant k_R is defined by the Arrhenius temperature dependence:

$$k_R = A_i \cdot T^{b_i} \cdot e^{\frac{-E_i}{R \cdot T}} \tag{2.42}$$

From the above equations, the chemical source term $\dot{\omega}_k$ is a function of mixture temperature T and mass fraction of species Y_r and are non linear as can be seen in equation 2.42 and 2.40.

$$\dot{\omega}_r = \dot{\omega}_r(Y_r, T)$$

In a RANS simulation, the Favre average of the reaction rate $\dot{\omega}_r$ is given by,

$$\widetilde{\dot{\omega}_r} = \dot{\omega}_r(\widetilde{Y_r, T}) \tag{2.43}$$

An important part of modelling combustion is closure of the mean reaction rate. Several complex turbulence chemistry interaction models have been proposed to model the mean reaction rate in the species equation. Few of the models capable of including the full chemistry is reviewed in the next few sections.

Well Mixed Model

In the well mixed model the interaction between turbulence and chemistry is not modelled into the species reaction rate. Instead the reaction rate is calculated based on the mean of species mass fraction and temperature. Thus equation 2.43 becomes

$$\widetilde{\dot{\omega}_k(Y_r, T)} \approx \dot{\omega}_r(\widetilde{Y}_r, \widetilde{T}) \tag{2.44}$$

The well mixed model assumes that the flames are in the well stirred reactor regime shown in figure 2.1. Thus the chemical time scales are larger than the turbulent time scale (Da $<$ 1) and the reaction is predominantly controlled by the chemistry. This model is less reliable when the turbulence controls the reaction (Da $>$ 1) and turbulence fluctuations are high enough to significantly change the reaction rates.

Eddy Dissipation Concept

The Eddy Dissipation Concept (EDC) is general combustion concept which assumes that all reactions are confined to "fine structures" (F Magnussen, 2005). The fine structures have a characteristic length similar to that of the Kolmogorov length scale. In the model, the reacting flow-field may be discretized into a network of perfectly-stirred reactors within these fine structures. The fine structures control the dissipation of turbulent energy into heat and molecular mixing of radicals. The reaction rate of any given species in each reactor is derived from theoretical arguments, based on the semi-empirical turbulent energy cascade between length-scales (F Magnussen, 2005).

The EDC has been applied for numerical simulation of various premixed and diffusion type combustion problems (F Magnussen, 2005). It has also been successful in capturing flame behaviour where chemical kinetics is faster than turbulent mixing and vice-versa. Furthermore, by including the detailed chemistry, mass fractions for individual species are solved without

needing to reduce the model to pre-defined mixture fractions or progress variables like flamelet models (Oijen and Goey, 2000).

Presumed PDF Approach

In the presumed Probability Density Function (PDF) approach a given shape of the PDF is assumed. The PDF function is defined by the mean and variance of the random variable or the physical quantity. The approach is usually based on a single variable. If multiple variables are involved, the joint PDF is calculated using the assumption that the variables are statistically independent (De and Chaudhuri, 2018).

In AVL Fire™ the model simulates turbulence chemistry interaction for the premixed combustion based on both the Gaussian PDF function for the local instantaneous temperature and on explicit relationships for the mean value of function $\overline{f(T)}$. These explicit relationships are derived using the Gaussian quadrature technique (Venkateshan and Swaminathan, 2014). The temperature T is assumed to be the random variable satisfying the Gaussian distribution, i.e.,$T = a + \sigma x$, where $a = \overline{T}$ is the mean value, $\sigma = \sqrt{\overline{T'T'}}$ is the variance, T' is the temperature pulsation and x is the Gaussian standard value varying from 0 to 1. The variance σ is estimated by solving a transport equation similar to one given in equation 2.45 which is used in FIRE™.

$$\frac{\partial \rho\sigma^2}{\partial t} + \frac{\partial}{\partial x_i}(u_i \rho\sigma^2) = \frac{\partial}{\partial x_i}\frac{\mu_t}{\sigma_t}\frac{\partial \sigma^2}{\partial x_i} + C_g \mu_t \left(\frac{\partial a}{\partial x_j}\right)^2 - C_d \rho \frac{\epsilon}{k}\sigma^2 \tag{2.45}$$

where $\sigma_t = 0.85$, $C_g = 2.86$ and $C_d = 2.0$.

2.6.4. Present Approach

In the present approach the average reaction rate is calculated as a function of average temperature and mass fractions of species involved. This approximation is represented by equation 2.44. The equation is only true if the fluctuating components of the temperature and mass fractions are small and the commutation error is negligible.

Ramaekers et al. (2019) performed a comparison of a RANS model ($k - \zeta - f$) and LES-CSM model on the emission prediction of OPRA DLE combustor with natural gas as fuel. The combustion was modelled using the FIRE™ detailed chemistry solver with GRI 3.0 mechanism (Smith et al., n.d.). At nominal load, the CO and NO emissions were predicted within 10% accuracy. Pomraning, Richards, and Senecal (2014) showed that accurate combustion results can be obtained with RANS turbulence model, detailed chemistry and sufficient mesh resolution. The author showed that, in many cases insufficient mesh resolution leads to under-resolved turbulence field. The under-resolved turbulence field leads to sub-grid error which has been wrongly viewed as turbulence chemistry interaction effects. Thus in absence of large fluctuations in temperature and species mass fractions, a well resolved turbulence field can produce good results.

The inclusion of preferential diffusion is achieved by calculating the molecular diffusion coefficient of each species. The diffusion coefficients are calculated in two ways. The first method uses mixture averaged diffusion coefficient which calculated one diffusion coefficient per species. In the second method, the multi-component diffusion coefficients are used (Lefebvre and Ballal, 2010). The general species transport equation is given by equation 2.46 and 2.47. Each species diffuses with different diffusion velocities in the mixture.

$$\frac{\partial \rho Y_r}{\partial t} + \frac{\partial}{\partial x_i}\left(\rho U_i Y_r\right) = \frac{\partial}{\partial x_i}\left(\Gamma_{y_r}\frac{\partial y_r}{\partial x_i}\right) + \dot{\omega}_r \quad r = 1, 2, \ldots K_{spec} \tag{2.46}$$

$$\Gamma_{y_r} = \left(\rho D_{r,m} + \frac{\mu_t}{Sc_t}\right) \tag{2.47}$$

where S_{C_t} is the turbulent Schmidt number and $D_{r,m}$ is the mixture averaged diffusion coefficient of species r in mixture m.

The multi-component diffusion equations for ideal gas is given by Maxwell-Stefan equation (Taylor and Krishna, 1993):

$$\nabla x_r = \sum_{j=1, j\neq r}^{K_{gas}} \frac{M}{\rho D_{rj}} \left(\frac{x_r \vec{j_j}}{M_j} - \frac{x_j \vec{j_r}}{M_r} \right) \quad r = 1,2...K_{spec} \tag{2.48}$$

here x_r and j_r are mole fraction and diffusive mass flux of species r, M is the molar mass of the mixture and D_{rj} is the binary diffusion coefficient between species r and j. The species transport equation with multi-component diffusion is given in equation 2.49 and 2.50.

$$\frac{\partial \rho Y_r}{\partial t} + \frac{\partial}{\partial x_i}\left(\rho(U_i - U_{\delta i})Y_r\right) = \frac{\partial}{\partial x_i}\left(\Gamma_{y_r,r}\frac{\partial y_r}{\partial x_i}\right) + S_{y_r} + \frac{\partial}{\partial x_i}\sum_{j=1, j\neq r}^{K_{gas}-1}\left(\Gamma_{y_r,j}\frac{\partial y_j}{\partial x_i}\right) \quad r = 1,2,...K_{spec}-1 \tag{2.49}$$

$$\Gamma_{y_r,j} = \left(\rho D_{rj} + \frac{\mu_t}{Sc_t}\delta_{rj}\right) \tag{2.50}$$

2.6.5. Reaction Mechanism

A large number of reaction mechanisms exist in the literature which includes H_2/O_2 kinetics. But the accuracy of these sub mechanisms have to taken into consideration while selecting a reaction mechanism for pure hydrogen air reactions. The current investigation allows the use of reduced reaction mechanisms for hydrogen air combustion. A reduced reaction mechanism allows to capture the chemistry of dominant reactions and reduce computational cost of solving transport equation for more species. Since NO_x prediction is not part of the research, the number of reactions reduces and nitrogen mass fraction is calculated as $1 - \sum Y_i$ where $\sum Y_i$ is the sum of mass fractions of all species except nitrogen.

Ströhle and Myhrvold (2007) studied six reaction mechanisms for hydrogen air reaction by comparing laminar flame speeds at atmospheric and high pressure conditions with experimental values. Out of the six mechanisms, the Li et al. (2004) and the Ó Conaire et al. (2004) mechanisms performed better while comparing the ignition delay times. The laminar speeds predicted by the mechanism was also compared at P = 1 atm and 4 atm and found good agreement with the experiments. The almost equal performance of these models is attributed to the use of same experimental data for these mechanisms. But the author(Ströhle and Myhrvold, 2007) recommends the Li et al. (2004) mechanism since it contains more up-to date data for gas turbine conditions. The Li et al. (2004) mechanism for hydrogen-air combustion is listed in table 2.3.

2.7. Conclusion

Hydrogen provides a solution to sustainable and clean energy source for future needs of human civilization. This study investigates a cleaner and safe way of using hydrogen as gas turbine fuel. The main challenge with transitioning from conventional fuels to hydrogen is the improvements needed to the existing combustor technology to mitigate flame flashback and NO_x emissions.

The Aerodynamically Trapped Vortex (ATV) combustor have shown significant promise in achieving stable and clean combustion of hydrogen rich fuel gases. The lack of extensive studies on the ATV combustor motivates this research to investigate important flow and

No.	Reaction		A	n	E
1	$H + O_2 = O + OH$		3.547×10^{15}	-0.406	16.599
2	$O + H_2 = H + OH$		0.508×10^{5}	2.67	6290
3	$H_2 + OH = H_2O + H$		0.216×10^{9}	1.51	3430
4	$O + H_2O = OH + OH$		2.970×10^{6}	2.02	13.400
5	$H_2 + M = H + H + M^a$		4.577×10^{19}	-1.40	104.380
6	$O + O + M = O_2 + M^a$		6.165×10^{15}	-0.50	0
7	$O + H + M = OH + M^a$		4.417×10^{18}	-1.00	0
8	$H + OH + M = H_2O + M^a$		3.800×10^{22}	-2.00	0
9	$H + O_2 + M = H0_2 + M^b$	k_∞	1.475×10^{12}	0.60	0
		k_0	1.475×10^{12}	0.60	0
10	$HO_2 + H = H_2 + O_2$		1.660×10^{13}	-1.72	524.8
11	$HO_2 + H = OH + OH$		7.079×10^{13}	0.0	823
12	$HO_2 + O = O_2 + OH$		0.325×10^{14}	0.0	295
13	$HO_2 + OH = H_2O + O_2$		2.890×10^{13}	0.0	0
14	$HO_2 + HO_2 = H_2O_2 + O_2$		4.200×10^{14}	0.0	-497
	$HO_2 + HO_2 = H_2O_2 + O_2$		1.300×10^{11}	0.0	11.982
15	$H_2O_2 + M = OH + OH + M^c$	k_∞	2.951×10^{14}	0.0	-1629.3
		k_0	1.202×10^{17}	0.0	48.430
16	$H_2O_2 + H = H_2O + OH$		0.241×10^{14}	0.0	3970
17	$H_2O_2 + H = HO_2 + H_2$		0.482×10^{14}	0.0	7950
18	$H_2O_2 + O = OH + HO_2$		9.550×10^{6}	0.0	3970
19	$H_2O_2 + OH = HO_2 + H_2O$		1.000×10^{12}	0.0	0
	$H_2O_2 + OH = HO_2 + H_2O$		5.800×10^{14}	0.0	9557
a	Third body enhancement factor: $H_2 = 2.5$, $H_2O = 12$				
b	Third body enhancement factor: $H_2 = 2$, $H_2O = 11$, $O_2 = 0.78$. Troe parameter: 0.8.				
c	Third body enhancement factor: $H_2 = 2$, $H_2O = 11$. Troe parameter: 0.5				

TABLE 2.3: Li et al. (2004) reduced reaction mechanism for H_2/O_2 where, $k = AT^n exp(-E/RT)$ with nitrogen as main bath gas. The units are cm, moles, s, cal and K.

combustion dynamics of the design. This research focuses on the trapped vortex flame stabilization and flame flashback mechanism of the combustor. A numerical approach is adopted where the numerical models to be employed in this study will be validated with premixed hydrogen combustion experiments performed at the Combustion Research Laboratory, Paul Scherrer Institute, Switzerland (Daniele et al., 2013; Siewert, 2006).

The validation study will help in understanding the merits and shortcomings of the numerical models used in this research for hydrogen combustion and act as a reference for further improvements. The effect of preferential diffusion on turbulent premixed hydrogen flames is studied by running the reactive simulations with a full chemistry well mixed model. The model solves for transport equations for all species thus taking into account the thermo-diffusive instabilities.

The design of the Aerodynamically Trapped Vortex combustor is based on the flashback prediction model by Tober (2019) (sec. 2.4.3 and Lin's correlation (sec. 2.4.4) for critical velocity gradient (sec. 2.4.4). Even though the Damköhler correlation (sec. 2.4.1) shows promising results and requires minimal calculations, it's applicability is limited to the operating conditions it is optimized for. On the other hand, Tober's model can be easily extended to different operating conditions for the given flashback process.

A sensitivity analysis of trapped vortex stabilization of the ATV combustor by varying

inlet flow velocity helps to isolate critical points of instability in the geometry to assist in better flow control. By comparing the behaviour of trapped vortex in cold flow and reactive flow, the effect of heat release on vortex dynamics can be understood. The knowledge gained from this research could serve as a baseline for further development of ATV combustors, thereby contributing towards transition to a sustainable and clean energy future.

3

Validation of Numerical Method

The numerical methods to be used in the study of Aerodynamically Trapped Vortex (ATV) Combustor needs to be validated. In the absence of any publicly accessible experimental results for the ATV combustor, results from experiment performed on similar flows are sought. The numerical setup used in the validation case will also be adopted in the study of ATV Combustor.

The important characteristic of the flow in an ATV combustor is that it is non-swirling, symmetric and that it involves recirculation and reattachment. The reaction simulations in the ATV combustor are to be performed with a 100% hydrogen-air premixed fuel. Therefore it was important to find a similar experimental case study. As a validation case, flow and combustion experiments performed in a generic backward facing step cylindrical combustor setup at the Combustion Research Laboratory, Paul Scherrer Institute (PSI), Switzerland is selected.

3.1. Description

Siewert (2006) performed cold flow experiments in the generic cylindrical combustor setup as shown in figure 3.1. The turbulence is controlled by circular grids placed at different axial positions upstream of the inlet. The flow is visualized and quantified by means of Particle Image Velocimetry (PIV).

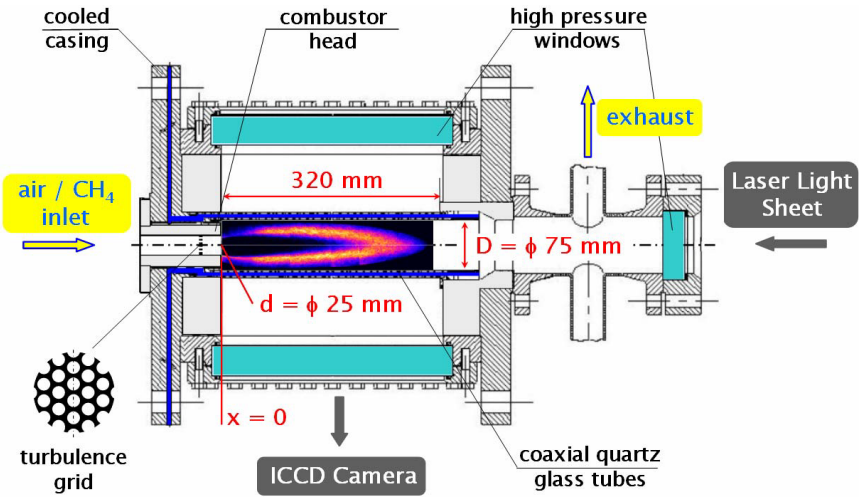

FIGURE 3.1: High pressure combustion chamber Siewert, 2006.

The author performed the experiments in a separate atmospheric test rig similar in geometry to the high pressure test rig shown in figure 3.1. He also varied the inlet velocity

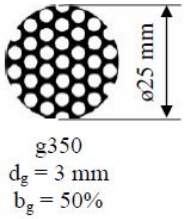

FIGURE 3.2: Turbulence grids; d_g - hole diameter, b_g - blockage ratio.

and the inlet turbulent intensity to study the flow field characteristics. Extensive qualitative and quantitative results are available for the case with a bulk inlet velocity of 40 m/s and a turbulent intensity of 8.1%. The inlet temperature and pressure of the air at the inlet are 293 K and 1 atm respectively. The inlet turbulence was controlled by placing circular plates with varying hole sizes and blockage ratio upstream of the combustor inlet. For the current case, a g350 grid as shown in figure 3.2 is placed at a grid position of 30 mm upstream of the inlet.

The mean flow field (U_mean), the turbulence intensity ($u^{'}$) and the integral length scale of turbulence (L_T) were quantified from the experiments. The effect of turbulence grid and inlet velocity on the turbulence characteristics were also studied by Siewert (2006). Out of the many cases studied, the above case with 40 m/s bulk flow velocity and g350 grid is selected due to two reasons. Firstly both qualitative and quantitative results are available for the case. Secondly, as will be explained in the next paragraph, the same inlet conditions were used for reactive flow experiments in the same combustor setup.

The validation of the reactive models for premixed hydrogen-air combustion is performed by comparing with results from experiment conducted by Daniele et al. (2013) in the same combustor setup. Daniele et al. (2013) studied axisymmetric V-flames of syngas/hydrogen-rich fuel gases to assess turbulent flame speeds (S_T) and stretched laminar flame speeds ($S_{L,k}$). The case of interest here is the experiments performed with premixed 70%/30% H_2/N_2 by vol. fuel. Absence of any hydrocarbon components in the selected fuel makes it the best candidate for the validation of reactive models for pure hydrogen premixed turbulent flames. Flame front corrugation was measured with planar laser-induced fluorescence (PLIF) of the OH* radical, while turbulent velocity ($u^{'}$) and integral length scale in the flame was determined with particle image velocimetry (PIV).

For the cases studied, the flame shape is visualized for a fuel equivalence ratio of $\phi = 0.35$. The average turbulent flame speed (S_T) and turbulent velocity ($u^{'}$) is estimated at the flame front. S_T and $u^{'}$ is also measured for two other cases by varying the equivalence ratio of the fuel. From the cold flow simulations performed by Siewert (2006), it was concluded that changing inlet turbulence has little effect on the turbulence near the flame zone. Thus only equivalence ratio is varied to derive a correlation between $S_T/S_{l,0}$ and $u^{'}/S_{l,0}$. Both the flame shape and turbulent flame speed calculated from the numerical simulations will be compared with that of the experiment in this study.

3.2. Numerical Setup

To reduce the computational cost of simulating the whole combustor, 45^o section of the combustor is selected to run all the simulations for the validation case. A 3D view of the CAD geometry is shown in figure 3.3. The flow is simulated in the section of the combustor downstream of the turbulence grid in the actual experiment. Therefore the CAD geometry includes a small 10mm length and 25 mm diameter cylindrical section added upstream of the combustor inlet.

Since the combustor geometry is not too complicated, a structured mesh setup is selected. A structured grid approach allows for better control over the mesh refinement

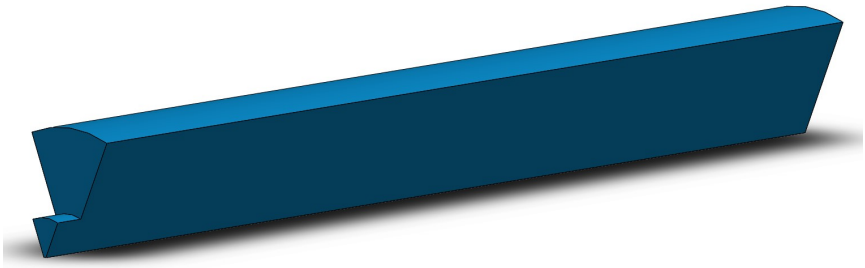

Figure 3.3: CAD geometry of the domain selected for validation simulations.

process and mesh size. A summary of the numerical setup is given in table 3.1 below. Cold flow

	Cold Flow	Reactive Flow
Run mode	Steady	Unsteady
Discretization Scheme	SIMPLE	SIMPLE
Differencing Scheme		
Momentum	AVL Smart Bounded	AVL Smart Bounded
Continuity	Central Differencing	Central Differencing
Turbulence	AVL Smart Bounded	AVL Smart Bounded
Energy	Not activated	AVL Smart Bounded
Convergence Criteria	1e-5	1e-5

Table 3.1: Numerical setup for validation simulations.

simulations are performed with two RANS turbulence models, the standard $k-\epsilon$ model and $k-\zeta-f$ model. The $k-\epsilon$ model is the most common turbulence model used for industrial flow simulations. It is a two equation linear eddy-viscosity model which has shown great promise in flows with small pressure gradients. The k-ζ-f model was proposed by Hanjalic, Popovac, and Hadžiabdić (2004). It is a three equation non-linear eddy-viscosity turbulence model based on Durbin's elliptic relaxation concept (Durbin, 1991) which eliminated the need for empirical damping functions near the wall.

One of the turbulence models is selected for the reactive simulations based on the results from turbulence model validation. Additionally, the modules species transport and General Gas Phase Reactions (GGPR) are activated for the reactive simulations. The module GGPR contains the internal chemistry interpreter where the inputs are chemical reaction mechanism, ignition mechanism, and a turbulence chemistry interaction model. Due to reasons explained in section 2.6, the 9-species, 19 reaction H_2/O_2 mechanism devised by Li et al. (2004) is selected as the reaction mechanism for all the reaction simulations. Since preferential diffusion is an important part of the species transport, it is included in the species conservation equations in two different ways. The first method uses Mixture Averaged Diffusion (MAD) coefficient and the second method uses Multi-component Diffusion (MCD) coefficients. The latter method is also computationally more expensive than the former method due to the additional equations being solved as mentioned in section 2.2.2.

3.3. Boundary Conditions

Table 3.2 gives an overview of the boundary conditions imposed on the domain for the cold flow simulations. A 2D sketch of the geometry with the dimension and types of boundary

conditions at each face is given in figure 3.4. A brief discussion of the choices made for each boundary condition will follow the table.

Cold Flow			
	Inlet	Outlet	Wall
Type	Velocity Inlet	Pressure Outlet	No slip wall
Velocity	User defined	-	0
Pressure	-	1 atm	-
Temperature	298 K	-	Isothermal
Turbulent Intensity	9%	-	-

TABLE 3.2: Summary of boundary conditions for turbulence model validation simulations.

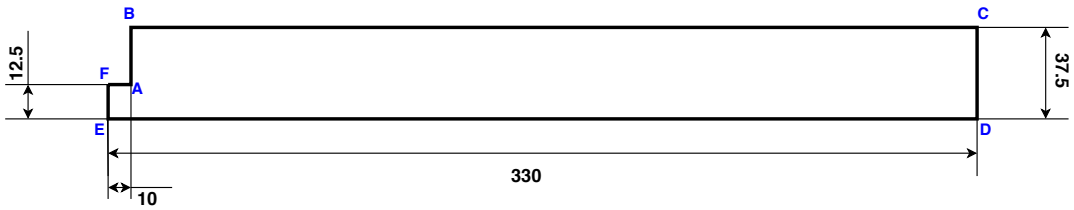

FIGURE 3.4: 2D sketch of domain with boundaries (all lengths in mm).

3.3.1. Inlet Condition

In the experiment, the flow starts at a significant length upstream of the combustor inlet. Since the exact velocity profile at the inlet to the combustor is not known, an iterative approach was selected to derive the correct inlet condition. In the first step a constant axial velocity profile of 40 m/s was given at the inlet. This resulted in an velocity of 41 m/s at the inlet to the combustor. The experimental maximum velocity at the inlet to the combustor is 44.8 m/s. Therefore the velocity profile at the combustor inlet should be that of a partially developed flow with a maximum velocity of 44.8 m/s. With a bulk velocity of 40 m/s and pipe diameter of 25 mm, the Reynolds number of the flow upstream of the combustor inlet is 6.82×10^4. Therefore the flow upstream of the turbulence grid turbulent and therefore a turbulent velocity profile with maximum velocity of 44.8 m/s and average velocity of 40 m/s was selected as the inlet condition just upstream of the turbulence grid. The function for velocity profile was derived using an interpolation of sampled values for a turbulent cylindrical pipe simulation. The sampling points were taken at an axial position in the pipe where the maximum velocity was 44.8 m/s. The radial velocity profile is as given in equation 3.1

$$U_r = a \times exp(\frac{b}{r+c}) + offset \tag{3.1}$$

where r is the radial distance from the center of the inlet; a = -0.86610; b = -0.00647; c = -0.01414 and offset = 44.80068.

From the experimental results, the turbulent intensity at the combustor inlet was calculated as 8.1% of the bulk velocity (40 m/s). To account for dissipation, a value of 9% was given as the inlet turbulent intensity of the flow. This setup ensured that the inlet velocity and turbulence in the experiment was captured to maximum accuracy in the numerical simulation. This assumption is also verified in the turbulent velocity plots in section 3.5.

3.3.2. Other Boundaries

Since the flow is axisymmetric, a symmetric boundary condition was imposed at the lateral sides of the domain for both the cold flow and the reactive flow simulations. The pressure at the outlet of the domain is different for cold flow and reactive flow cases. The outlet pressure for the cold flow case is the atmospheric pressure (1 atm). In the reactive flow case the outlet pressure is set as 2.5 atm or 0.25 MPa. There are three walls in the domain. For both cold flow and reactive flow cases, the walls are rigid and no slip boundary condition is imposed. In the cold flow, the walls are isothermal with a temperature of 298 K. The walls in the reactive flow case is assumed adiabatic ($\dot{q}_w = 0$).

For the reactive case, the air inlet was replaced with premixed hydrogen- air mixture with the same velocity profile. The fuel is a 70%/30% H_2/N_2 by vol mixture. A summary of the boundary condition for the reactive flow simulations is given in table 3.3. Using the fuel equivalence ratios of 0.25, 0.35 and 0.45, the mole fractions of the gases in the mixture was calculated and given as inlet mole fraction at the inlet. The species and their respective mole fractions at the inlet is given in table 3.4.

Reactive Flow			
	Inlet	Outlet	Wall
Type	Velocity Inlet	Pressure Outlet	No slip wall
Velocity	User defined	-	0
Pressure	-	2.5 atm	-
Temperature	623 K	-	Adiabatic
Turbulent Intensity	9%	0%	-
Gas	Fuel-Air mixture [3.4]	Air	-

Table 3.3: Summary of boundary conditions for combustion model validation simulations.

ϕ / Species	H_2	H	O_2	O	OH	H_2O	HO_2	H_2O_2	N_2	Ar
0.25	0.091	0	0.183	0	0	0	0	0	0.726	0.00
0.35	0.121	0	0.174	0	0	0	0	0	0.705	0.00
0.45	0.149	0	0.165	0	0	0	0	0	0.686	0.00

Table 3.4: Species mole fraction of the fuel-air mixture at the inlet.

The whole domain is initialized with premixed fuel-air. A spherical ignition source is placed at the corner indicated by point A as shown in figure 3.4. The properties of the ignition source is given in table 3.5. The flow was ignited at the given location at 0.5 *ms* into the simulation for a duration of 0.5 *ms*.

Location [mm]			Radius [mm]	Energy factor
x	y	z		
12.5	15	0	2.5	0.75

Table 3.5: Properties of ignition source.

3.4. Mesh Independence

A mesh independence study was performed to select the right grid size for the validation studies. Four structured meshes with number of cells of 0.46 MM, 0.86 MM, 1.1 M and 1.5 MM are generated using AVL FAME. Figure 3.5 shows the mesh with around 1.1 MM cells which has approximately 95% hexahedral elements.

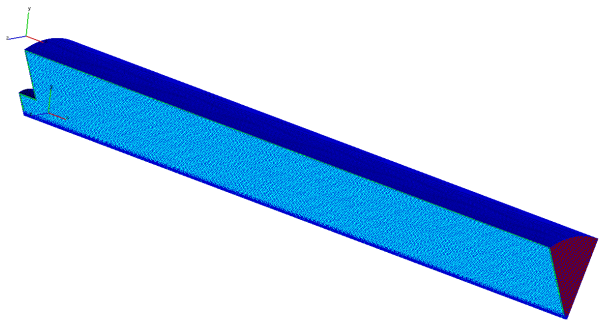

FIGURE 3.5: Structured mesh with around 1.1 million cells.

The numerical setup for the mesh independence study is similar to the numerical setup detailed in the above section. For turbulence modelling, the $k-\epsilon$ model is used with standard wall functions for wall treatment. From the converged results, total velocity was sampled at three axial lines at different radial positions in the domain. This ensured that the mesh is independent of the flow behavior at (25 mm), near (10 mm) and away (3mm) from the recirculation zone. The results of the study performed are shown in figure 3.6. From the results it can be concluded that the results are independent above the mesh size of 1.1 MM cells. Therefore subsequent validation studies are performed with this mesh.

Numerical simulations performed by Pomraning, Richards, and Senecal (2014) revealed the importance of proper grid resolution in the flame zone to accurately capture the flame behaviour. Grid independence studies performed by the author found a grid size of 0.2 mm is sufficient to resolve the sub-grid length scales in the flow.

From the experimental results, the approximate position of the flame is known. Since the equivalence ratio is changed in this study, the flame position is expected to change with different cases. Thus with the flame position for $\phi = 0.35$ as the reference case, the cold flow grid is refined in a wider area surrounding the reference flame. The resulting mesh is shown in figure 3.7.

3.5. Cold Flow

This section is the validation of turbulence models using the results from the cold flow experiments performed by Siewert (2006). The results from the simulations are compared both qualitatively and quantitatively with the results from the experiment. Qualitative analysis of the results is achieved by comparing the velocity contours, streamlines and recirculation bubble length. Further a quantitative analysis of the turbulence models is performed by quantitative comparison of the following results from the experiment.

1. Axial velocity (U_{mean}) profile at y = 0
2. Rms turbulent velocity (u'_{rms}) at y = 0
3. Radial distribution of u'_{rms} at x = 3 mm, 40mm and 150 mm

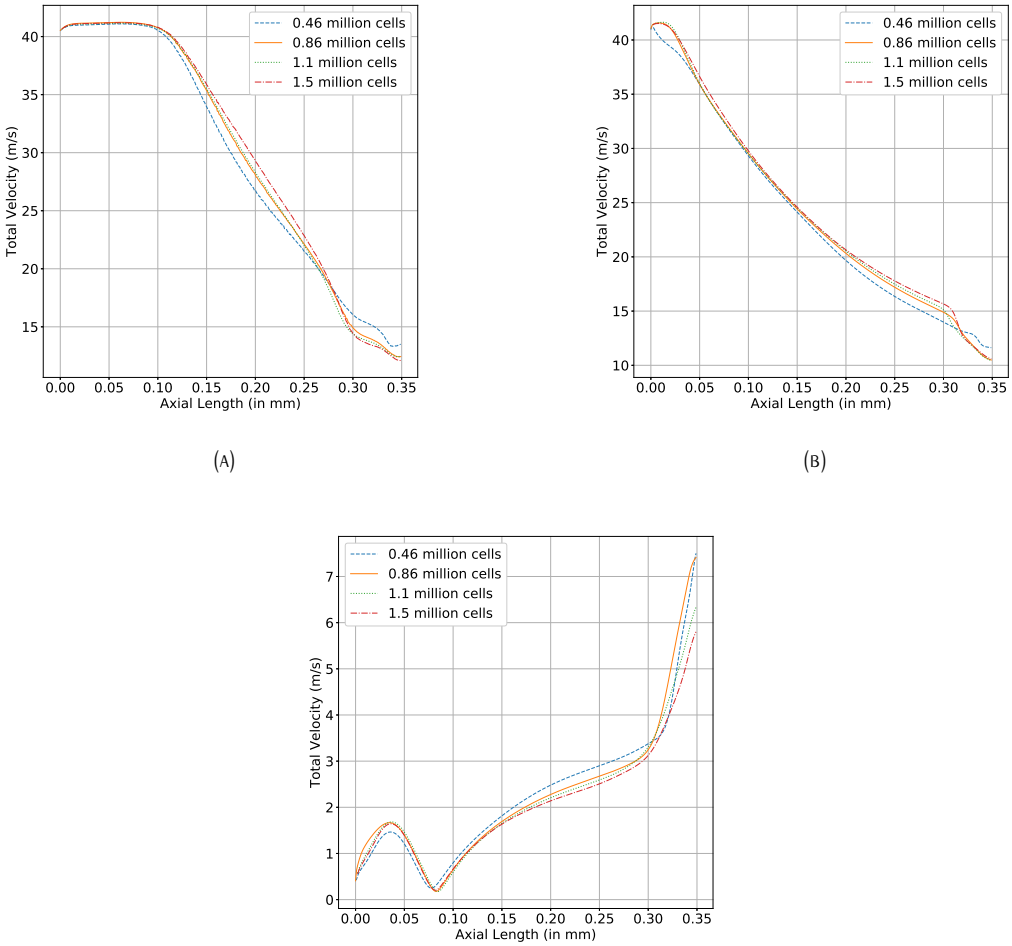

(A)

(B)

(C)

FIGURE 3.6: Mesh independence study by taking velocity data at radial locations. A : r=3 mm; B: r=10 mm; C: r=25 mm.

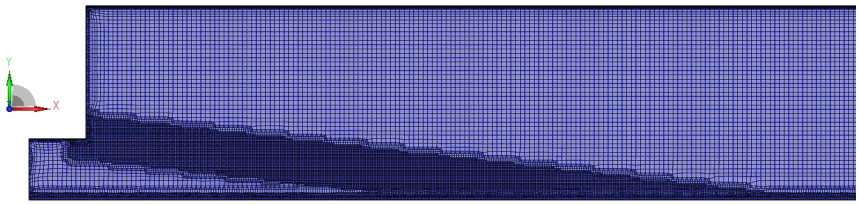

FIGURE 3.7: Mesh for reactive simulation with refinement in the flame zone.

The non-reactive flow simulations with the described numerical setup and boundary conditions was run on the mesh with 1.1 million cells. Modelling of turbulence was achieved by Reynolds Averaged Navier-Stokes models -

1. $k - \epsilon$ model
2. $k - \zeta - f$ model

The axial velocity contour with velocity streamlines for both models and from the experiment are shown in figure 3.8.

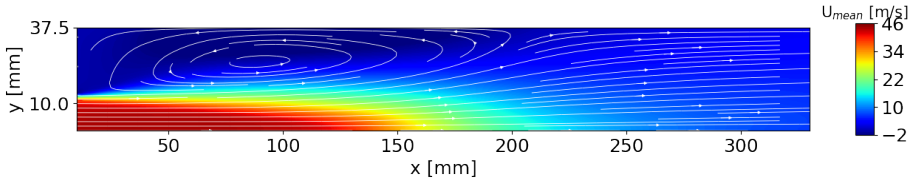

(A) Axial velocity contour and streamline with $k - \epsilon$ model.

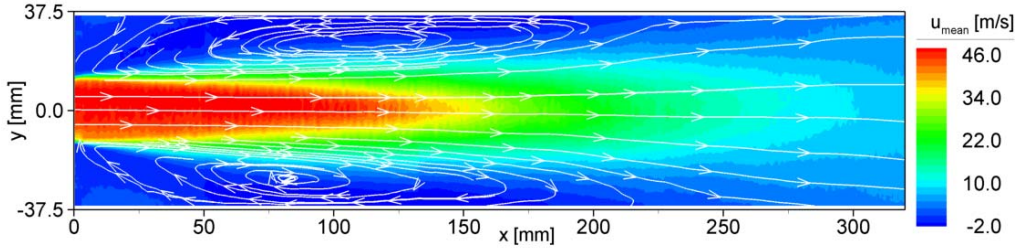

(B) Axial velocity contour and streamline from experiment.

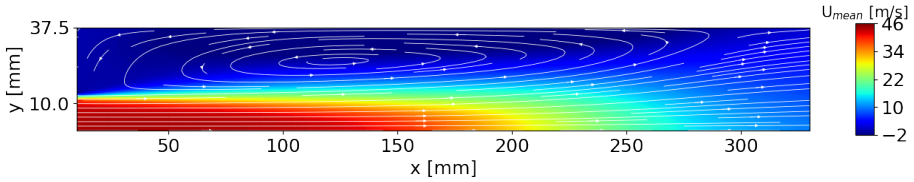

(C) Axial velocity contour and streamline with $k - \zeta - f$ model.

FIGURE 3.8: Comparison of mean flow contour and streamlines from the numerical simulation with experimental results.

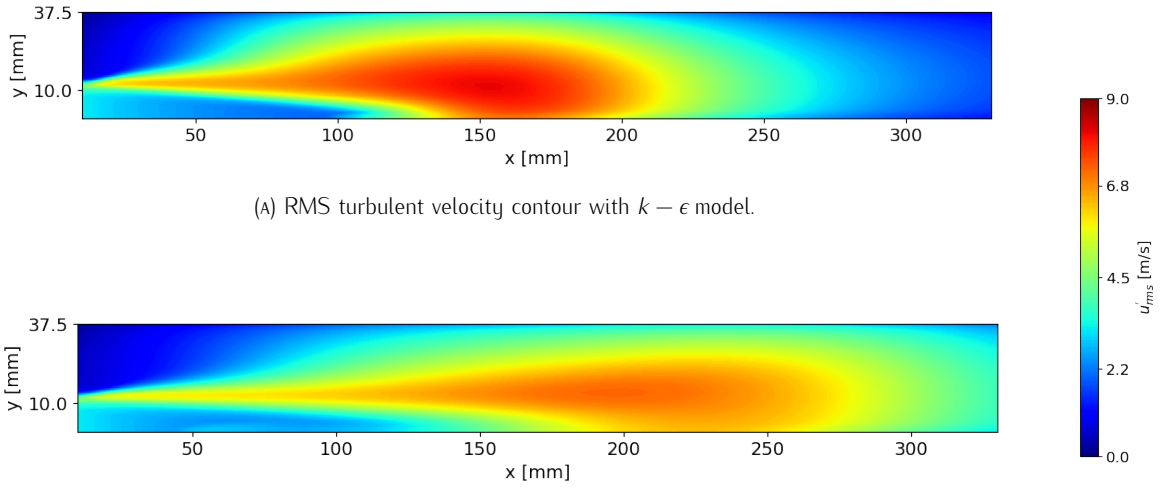

(A) RMS turbulent velocity contour with $k - \epsilon$ model.

(B) RMS turbulent velocity contour with $k - \zeta - f$ model.

FIGURE 3.9: Comparison of rms turbulent velocity fluctuations from the numerical simulation.

Due to the sudden expansion in the combustor geometry, a recirculation zone is formed. The $k - \zeta - f$ model is seen to be over-predicting the length of recirculation zone or the reattachment length compared to the $k - \epsilon$ model. From the experiments, the flow reattaches at a length $R_L = 220\ mm$ downstream of the inlet. This corresponds to $x/D \approx 9$. In the

simulation, the $k-\epsilon$ and $k-\zeta-f$ model predicts a reattachment length of $R_L^{k-\epsilon} \approx 210\,mm$ ($x/D \approx 8.4$) and $R_L^{k-\zeta-f} \approx 290\,mm$ ($x/D \approx 11.6$) respectively.

The turbulent velocity contour in figure 3.9a and 3.9b is representative of the turbulent kinetic energy production and dissipation in the flow with the two models. A shear layer zone is formed with high turbulent intensities close to the combustor inlet which spreads and increases in radial distribution with increasing axial distance. Flow velocity and turbulence data was collected at sampling points similar to the experiment and the results were compared with that of the experiment. Figure 3.11 and 3.10 shows the averaged axial velocity (U_{mean}) and rms turbulent velocity (u'_{rms}) at the centerline of the combustor respectively.

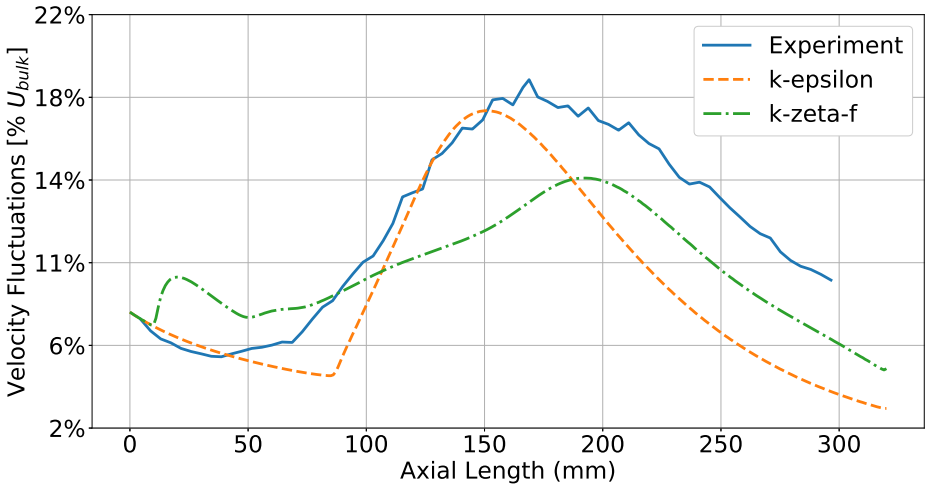

FIGURE 3.10: RMS turbulent velocity fluctuations at the centerline of the combustor.

The turbulence first decreases close to the combustor inlet due dissipation of the turbulence at the inlet. For axial distance x>80 mm, the turbulence increases due to turbulent transport from the shear layer. The turbulence reaches a maximum value at around $x =$ 180 mm. Downstream of this position, dissipation dominates and turbulence decreases rapidly. The $k-\epsilon$ model closely follows the turbulent kinetic energy production and dissipation in the experiment for region with x<150 mm (figure 3.10. The turbulent kinetic energy dissipation rate in the $k-\zeta-f$ model is higher than that in the experiment and the $k-\epsilon$ model. Since the same numerical discretization scheme was used for both turbulence models, the effect of numerical dissipation can be neglected in the comparison. Thus the difference in the dissipation can be attributed to the turbulence model.

The effect of higher dissipation rate in $k-\zeta-f$ model is evident in the mean velocity profile shown in figure 3.11. At the same axial location, the flow predicted by $k-\zeta-f$ model has higher kinetic energy than the flow predicted by $k-\epsilon$ model. Figure 3.12 shows the comparison of the relative error in the numerical results from the experiment along the centerline. The maximum, mean and standard deviation of the relative error in the axial mean velocity predicted by the turbulence models at the centerline is given in table 3.6. The error in the velocity prediction by $k-\zeta-f$ model is more than twice that of $k-\epsilon$ model.

The radial variation of rms turbulent velocity fluctuation at three axial locations is shown in figure 3.13. This is also a quantitative comparison of results from simulation with the values obtained from the experiment. The turbulence is severely under-predicted in figure 3.13a near the recirculation zone (y > 15 mm) by both models. Elsewhere, it can be observed that $k-\epsilon$ model follows the experimental results more closely than $k-\zeta-f$ model at all axial positions.

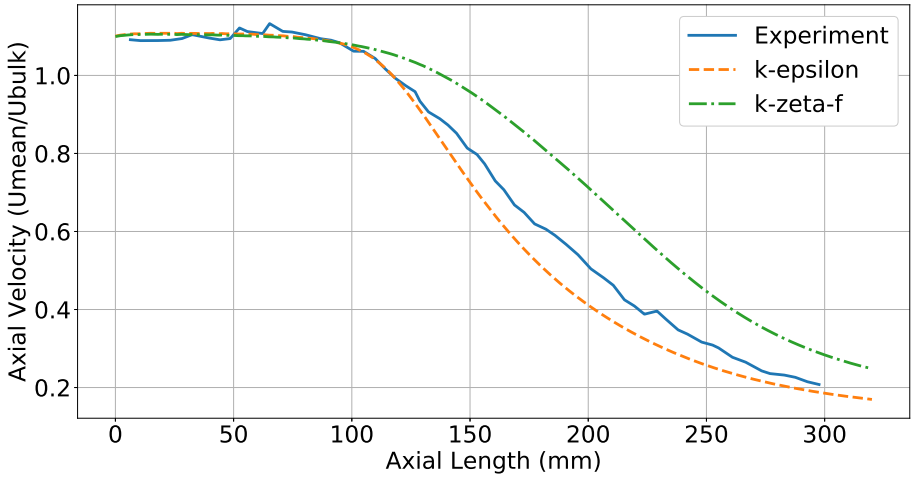

FIGURE 3.11: Center-line profile of mean axial velocity.

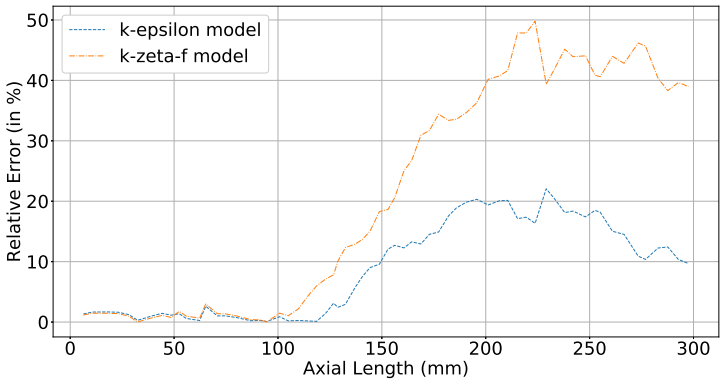

FIGURE 3.12: Relative error in the axial velocity along the centerline

Error (%)	k-epsilon	k-zeta-f
Maximum Error	22.05	49.79
Average Error	8.93	21.21
Standard Deviation of Error	7.59	18.26

TABLE 3.6: Comparison of error in the mean velocity profile predicted by the turbulence models.

3.6. Reactive Flow

In this section, the combustion model is validated for use in further studies. The data available from the experiment (Daniele et al., 2013) for validation are the plot depicting relation between $S_T / S_{l,0}$ and $u^{'} / S_{l,0}$ at three equivalence ratios and flame shape for $\phi = 0.35$. The flame properties are taken as average across the flame front and compared with that of the experiment. The effect of preferential diffusion on the flame is studied by comparing the flame position in the two cases studied with mixture averaged diffusion and multi-component diffusion coefficients.

The reactive flow simulations were run on the mesh refined at the flame zone as explained in 3.4. The numerical setup and boundary conditions are explained in sections 3.2 and 3.3 respectively. The application of detailed chemistry CFD can be quite time consuming.

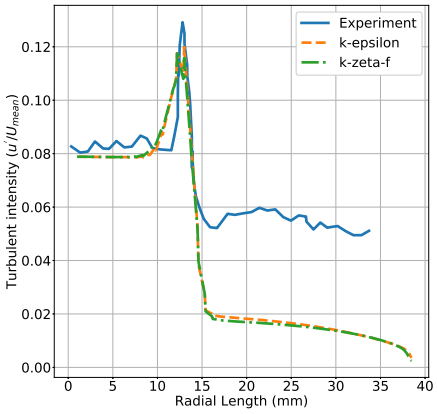

(A)

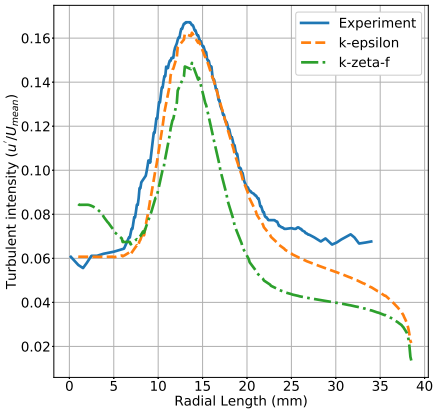

(B)

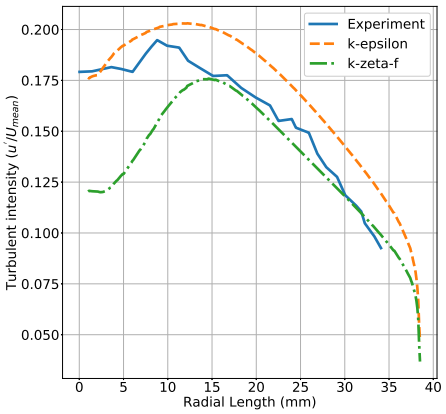

(C)

FIGURE 3.13: Comparison of radial turbulence intensity profile at axial locations. A : x=3 mm; B: x=40 mm; C: x=150 mm.

To decrease the run time, a multi-zone model is used in combination with the combustion model. The multi-zone model identifies and groups cells having similar thermodynamics conditions called clusters. At each time step chemical reactions are solved for the cluster and mapped back to cells. The multi-zone method is applied in a similar manner to that described in Liang, Stevens, and Farrell (2009). Since the simulation is of the unsteady type, the quantities of interest are averaged over the final 50 ms of time steps. The time evolution of the simulation is given in figure 3.14. The ignition is turned on 0.5 ms into the simulation. After another 0.5 ms it is turned off since the mixture ignited properly. After the ignition is turned off, the simulation enters the steady burning phase where the flow and flame slowly develops until it reaches a steady state. Once the fluctuations in the flow disappears, data collection starts at 50 ms into the simulation and continues for another 50 ms. The flow and flame properties are averaged over the data collection time and presented henceforth (Ramaekers et al., 2019).

3.6.1. Effect of equivalence ratio on flame structure

The effect of change in equivalence ratio of the mixture is studied here. The species diffusion coefficients in transport equation is calculated with the mixture averaged approach. First the combustion regime for all three cases is identified on the Borghi-Peters diagram (fig. 3.15).

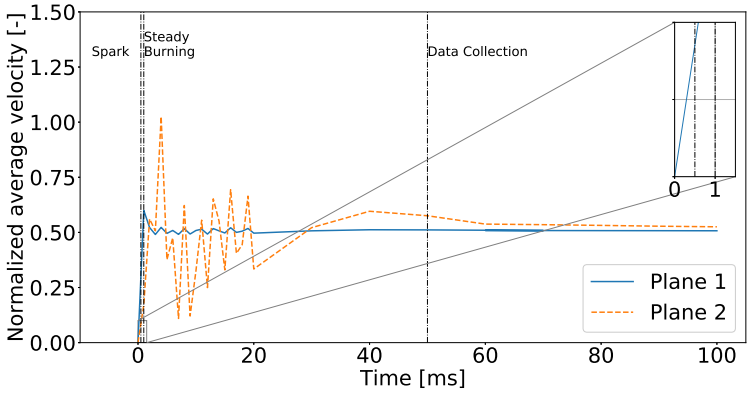

FIGURE 3.14: Time evolution of reaction simulation for combustion model validation.

With increase in equivalence ratio, the combustion regime of the resulting flame moves from

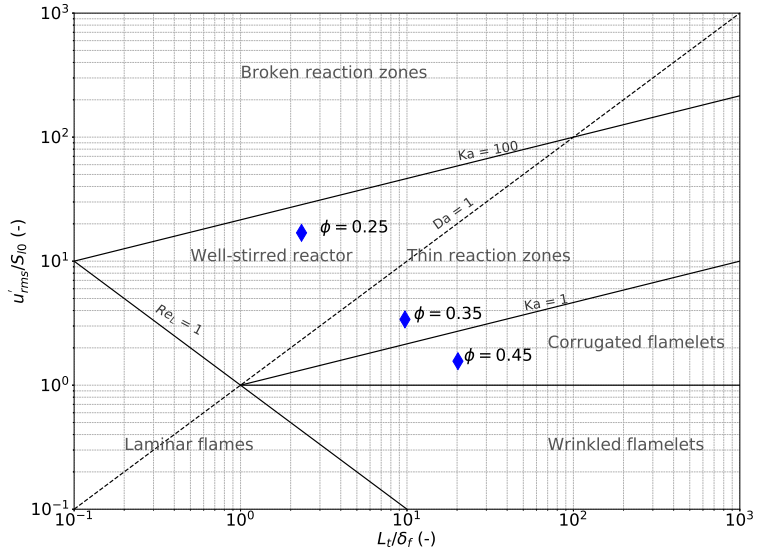

FIGURE 3.15: Combustion regime for the validation cases studied.

well stirred reactor to corrugated flames. Table 3.7 illustrate the main properties of the flame front in different cases.

ϕ	u' [m/s]	L_t [mm]	Re_L	Ka	Da	u'/S_l	L_t/δ_f
0.25	2.74	1.12	39.322	45.62	0.1374	16.9145	2.3249
0.35	2.68	1.03	32.98	2.0	2.8679	3.39133	9.7261
0.45	2.87	0.98	31.67	0.44	12.95	1.562	20.2408

TABLE 3.7: Turbulent flame and their characteristics.

In the well stirred reactor regime, the reactions are controlled by the mixing process since the chemical time scales are larger than the mixing time scale. Decreasing equivalence ratio reduces the laminar flame speed and increases the laminar flame thickness thus increasing the chemical time scale. In the cases studied, the turbulent flow characteristics u' and L_t

remains almost constant. Therefore the mixing time scale ($L_t/u^{'}$) remains similar for all the cases.

In the Peters diagram, the flame with $\phi = 0.25$ and $\phi = 0.35$ falls under the thin reaction zones. In both these cases, the Kolmogorov scales are fine enough to penetrate the preheat zone and influence the mixing process. But when the equivalence ratio was increased further to $\phi = 0.45$, the flame thickness became smaller than the Kolmogorov scales and the flame is only wrinkled by the turbulent fluctuations.

The averaged value of OH mass fraction for different equivalence ratio is given in figure 3.16. In the colorbars, $\widehat{Y_{OH}}$ represents the normalized OH mass fractions. The Y_{OH} values are normalized with maximum OH mass fraction value for the case with equivalence ratio of 0.45, $Y_{OH}^{max}(\phi = 0.45) = 0.00233176$. The extended inlet to the combustor is left out in the contour plots.

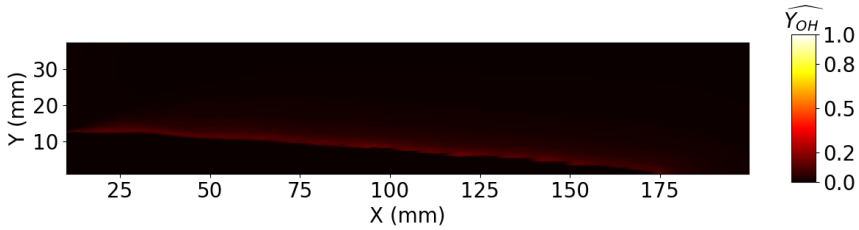

(A) $\phi = 0.25$

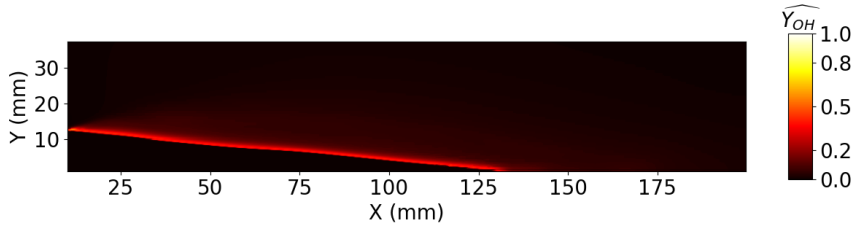

(B) $\phi = 0.35$

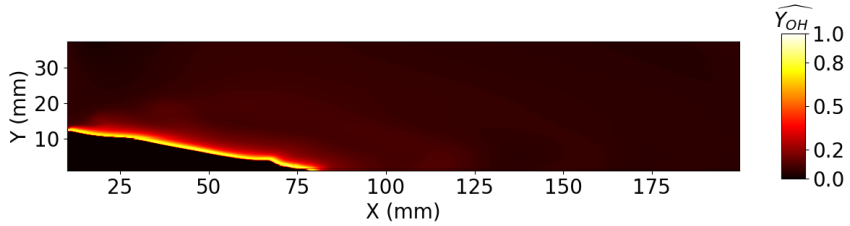

(C) $\phi = 0.45$

FIGURE 3.16: Distribution of OH mass fraction in the domain for different fuel equivalence ratios.

The position of maximum intensity the respective figures is a good indication of flame front. The length of the flame reduces with increasing equivalence ratio. This is due to the increase in turbulent flame speed as a consequence of increase in laminar flame speed. For hydrogen, the equivalence ratios studied falls left of the maximum in laminar flame speed vs equivalence ratio plot. Thus the laminar flame speed increases with equivalence ratio.

3.6.2. Comparison to experiment

After discussing the general characteristics of the flame, the flame obtained from numerical simulation is compared with that of the experiment in this section. The first part compares the flame shape and position for the case of $\phi = 0.35$. In the second section, the $S_T/S_{l,0}$ and $u^{'}/S_{l,0}$ correlation obtained from the numerical simulations are plotted with that obtained from the experiments.

Flame Front

The qualitative validation of the model is performed by comparing the flame front obtained from the numerical simulations with the experiment. In the experiment, the flame surface density of the flame is calculated by taking 400 OH-PLIF measurements of the flame. The flame front is identified as the location where OH radicals appear. Thus for flame front comparison, the flame front is estimated by calculating the OH mass fraction in the domain by setting the condition : $Y_{OH} \geq 0.01 Y_{OH}^{max}$.

In figure 3.17 the shape of the flame obtained from numerical simulation performed with mixture averaged diffusion coefficients is overlaid with the experimental flame surface density image obtained from experiments by Daniele et al. (2013). The intensity on the colorbar refers to the flame intensity which is representative of the flame surface density calculated by taking OH-PLIF measurements. A maximum error of 33% is observed at the combustor axis

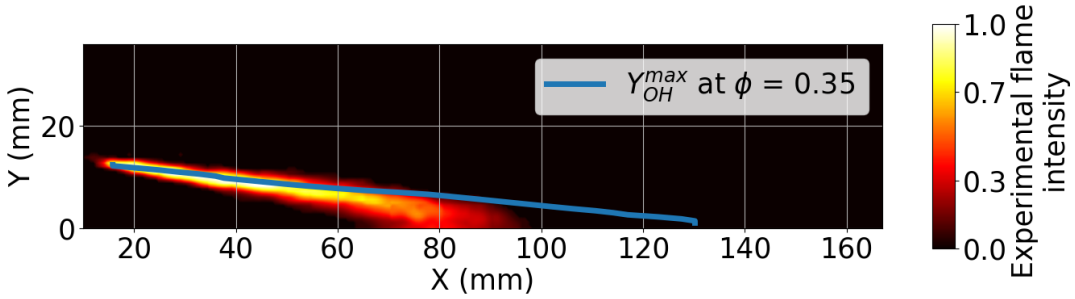

Figure 3.17: Comparison of flame shape in experiment and numerical simulation.

in the flame position predicted by the combustion model. This is due to the under-prediction of reaction rates which reduces the turbulent flame speed. The flame becomes longer with decreasing turbulent flame speed.

Turbulent Flame Speed

In addition to estimating the flame front, the turbulent flame speed and the rms turbulent velocity fluctuation in the flame front is also calculated. These parameters are calculated at a progress variable, $c = 0.05$. The progress variable c is based on the mole fraction of H_2O and is given by equation 3.2.

$$c = \frac{Y_{H_2O} - Y_1}{Y_2 - Y_1} \tag{3.2}$$

where Y_1 and Y_2 are the mole fractions of H_2O in the unburned and burned mixture respectively. Since the inlet contains only fuel and dry air, $Y_1 = 0$.

The turbulent flame speed (S_T) of the flame is calculated by taking the velocity of the flow perpendicular to the flame front at $c = 0.05$ as depicted in figure 3.18. The axial and radial components of velocity u and v are retrieved at the sampling points and the velocity

normal to the flame is calculated using the local slope of the flame front. The respective rms turbulent velocity fluctuation ($u^{'}_{rms}$) at $c = 0.05$ is also calculated.

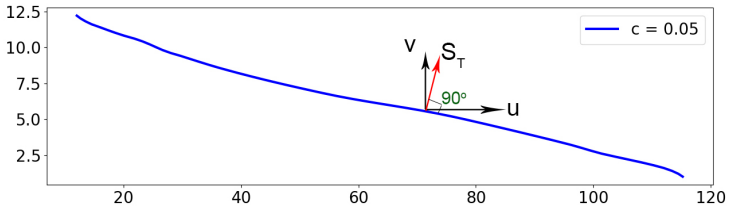

FIGURE 3.18: Estimation of turbulent flame speed from the simulation.

The laminar flame speed is calculated using the Cantera (Goodwin et al., 2018) toolbox in python. These values are used to calculate the normalized turbulent flame speed (S_T / S_L) and normalized turbulence velocity ($u^{'} / S_L$). Figure 3.19a shows the correlation between the normalized values derived from the numerical simulations compared with that obtained from the experiments.

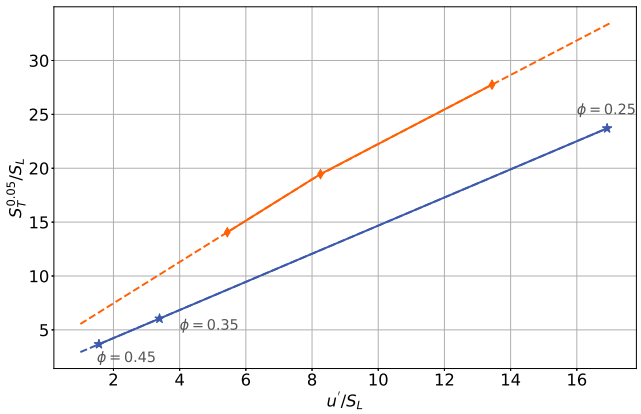

(A) Normalized turbulent flame speed comparison with experiment

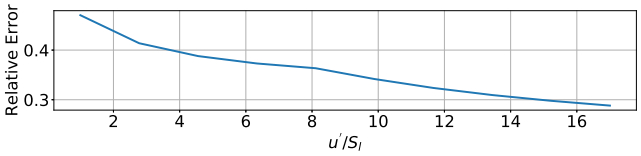

(B) Relative error in turbulent flame speed prediction

FIGURE 3.19: Quantitative validation of model with normalized turbulent flame speed.

In the figure 3.19a the equivalence ratio or the laminar flame speed decreases as we move towards higher values of $u^{'} / S_l$. The average turbulent velocity ($u^{'}$) remains almost constant around 2.89 m/s for all the three cases studied. Thus the turbulent flame speed is dependent on the change in laminar flame speed. The correlation obtained from the experiment

is given in equation 3.3.

$$\frac{S_T}{S_L} = \left[1 + \left(2u'/S_L\right)^2\right]^{0.5} \tag{3.3}$$

From a first look, the absolute error in the prediction of the normalized turbulent flame speed increases with decreasing equivalence ratio. But the relative error given by $\frac{S_T^{exp} - S_T^{num}}{S_T^{exp}}$ shows a different trend. The relative error decreases with decrease in ϕ. This can be explained with the combustion regime diagram in figure 3.15 explained in section 3.6.1.

The combustion model (well mixed model) used in this study assumes the flame to be perfectly stirred and neglects any and all turbulent fluctuations. From the regime diagram it was observed that with decreasing equivalence ratio, the flame moves towards the well stirred reactor regime. Therefore the error in the reaction rates calculated by the well mixed model decreases with reduction in equivalence ratio for the three cases studied.

The species conservation equation source term estimated by the well mixed model is based on the mean temperature and mass fractions of species. Rewriting equation 2.44,

$$\widetilde{\dot{\omega}_r(Y_r, T)} \approx \dot{\omega}_r(\widetilde{Y}_r, \widetilde{T})$$

In the equation, the source term is dependent on the mass fraction of species and the temperature of the mixture. In a perfectly premixed mixture, the fluctuations in mass fraction can be considered negligible (De and Chaudhuri, 2018). According to Reynolds analogy the turbulent momentum is correlated to heat transfer rate. Therefore presence of turbulent fluctuations imply the presence of temperature fluctuations in the domain or equation 3.4 holds.

$$u' \implies T' \tag{3.4}$$

The temperature dependence of species transport source term is dictated by the Arrhenius equation 2.42 rewritten here.

$$k_R = A_i \cdot T^{b_i} \cdot e^{\frac{-E_i}{R \cdot T}}$$

In the fast chemistry limit, the turbulence control the combustion process and fluctuation in temperature carries a lot of importance. The Arrhenius equation for turbulent flows can be written as in eq. 3.5.

$$k_R^{turb} = A_i \cdot (\tilde{T} + T')^{b_i} \cdot e^{\frac{-E_i}{R \cdot (\tilde{T} + T')}} \tag{3.5}$$

where $\tilde{T}$ is the Favre averaged mean temperature and T' the the temperature fluctuations. In the well mixed model, the contribution of temperature fluctuation to the reaction rate constant is omitted by accounting for only the mean temperature in the equation and assuming $T' = 0$. Hence the model fails to predict the turbulent flame speed and flame front similar to that of the experiment.

3.6.3. Effect of Preferential Diffusion

The effect of preferential diffusion on the flame is studied by comparing the flame shapes obtained from the two cases with MAD and MCD coefficients. The result is shown in figure 3.20. The maximum deviation in x-direction of the flame position between the two cases studied is approximately 1 mm. This is negligible compared to the actual length of the flame. Thus it can be concluded that there is no significant difference between diffusion coefficients calculated during the simulations using either methods.

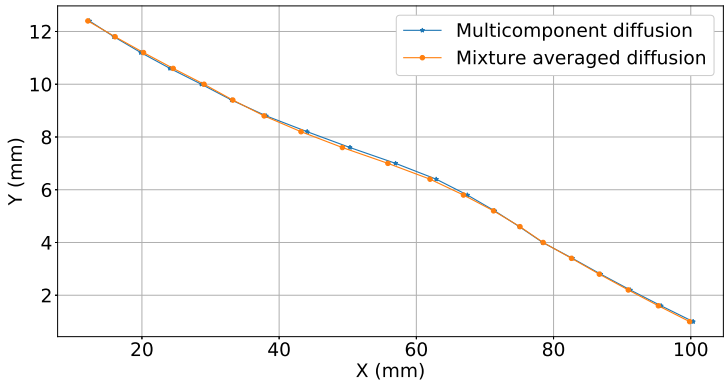

FIGURE 3.20: Comparison of flame shape in cases with MAD and MCD coefficients.

In all the cases studied N_2 is the dominant species in the mixture and can be considered as the diluent. When calculating the multi-component diffusion coefficients and mixture averaged diffusion coefficients, a dominant part of the value is the diffusion coefficient of species with respect to nitrogen. This explains the negligible difference in the diffusion coefficients calculated by the two methods.

Effective Lewis number

The laminar Lewis numbers for species H_2, O_2, N_2 and Ar are calculated using mixture averaged diffusion coefficients in Cantera. The values are calculated at preheat temperature of T = 623 K and inlet pressure of P = 0.25 MPa. In turbulent flows, the turbulent diffusion alters the

Lewis Number			
Species/ϕ	0.25	0.35	0.45
H_2	0.3480	0.3635	0.376
O_2	1.34	1.408	1.47
N_2	1.26	1.36	1.46
Ar	1.34	1.408	1.47

TABLE 3.8: Lewis number of species at T = 623 K and P = 0.25 MPa.

effective Lewis number of the species involved. Since the Lewis number of all other species except H_2 is close to 1, we only consider the case of H_2 in this study. The laminar and turbulent mass diffusion coefficients of H_2 and O_2 are calculated from the numerical results at a radial distance of y = 6 mm from the axis. The results of the calculation are represented in figure 3.21.

The left axis of fig 3.21 shows the ratio of the mixture averaged diffusion coefficient of hydrogen ($D_{H_2,m}$) to the turbulent diffusion coefficient (ν_t / Sc_t). The molecular diffusion coefficient ranges from 6-14% of the turbulent mass diffusion coefficient in the flame zone as the temperature increases from the unburnt to burnt gases. The right axis in the same figure represents the ratio of the total turbulent diffusion coefficient ($\Gamma_{k,m}$) of H_2 and O_2. The total diffusion coefficient is the sum of species molecular diffusivity ($\rho D_{k,j}$) and the ratio of turbulent diffusivity given by ratio of turbulent viscosity to Schmidt number ($\frac{\mu_t}{Sc_t}$) as given in equation 3.6.

$$\Gamma_{y_k} = \left(\rho D_{k,m} + \frac{\mu_t}{Sc_t}\right) \tag{3.6}$$

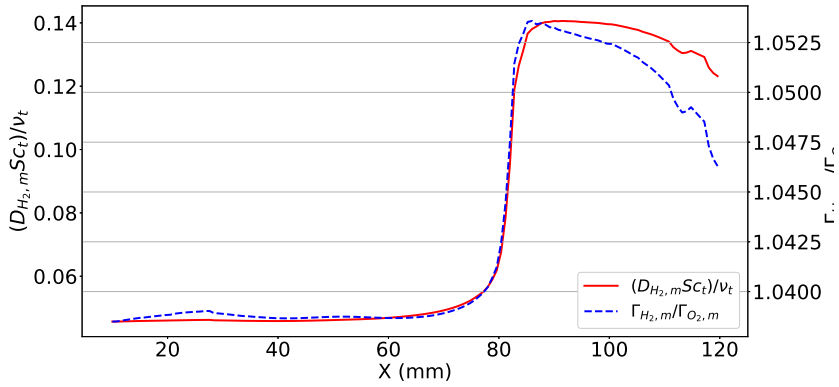

FIGURE 3.21: Ratio of diffusion coefficient of H_2 and O_2.

The maximum value of $\Gamma_{H_2,m}/\Gamma_{O_2,m}$ is less than 1.06. On the other hand, the ratio between molecular diffusivity of H_2 and O_2, $D_{H_2,m}/D_{O_2,m}$ is well above 3. Thus the diffusion process in the flame is dominated by turbulent mass diffusion.

Similar to mass diffusion coefficient, the total thermal diffusion coefficient is given by equation 3.7.

$$\Theta = \left(\rho\alpha + \frac{\mu_t}{Pr_t}\right) \tag{3.7}$$

Since the value of Pr_t and Sc_t is similar and equal to 0.7, the turbulent thermal diffusivity is same as the turbulent mass diffusivity. From these results the effective Lewis number of species i can be calculated by using equation 3.8.

$$Le_i^{eff} = \frac{\alpha + \frac{\nu_t}{Pr_t}}{D + \frac{\nu_t}{Sc_t}} = \frac{Le_i + \frac{\nu_t/Pr_t}{D}}{1 + \frac{\nu_t/Sc_t}{D}} \tag{3.8}$$

Taking the maximum value for $\frac{\nu_t}{Pr_t}/D$, the effective Lewis numbers are calculated for the three cases studied. Since the flow properties remained similar for all three cases studied, the only change is observed in the laminar Lewis numbers in all three cases. The calculated effective Lewis numbers for H_2 are given in table 3.9. From the values in the table below,

ϕ	0.25	0.35	0.45
Le_i^{eff}	0.91	0.912	0.914

TABLE 3.9: Effective Lewis number for H_2 in the premixed turbulent flame.

the effective Lewis number can be approximated to 1. Thus the effect of thermo-diffusive instabilities is not included in the model. The Reynolds number for the flow in the combustor is 4.02×10^4. When the Reynolds number or the turbulence increases in the flow, the effect of molecular diffusion on the total diffusion reduces. But from section 2.2.2 thermo-diffusive instabilities were found even in high turbulent flows having flow Reynolds number close to the validation case. Hence the well mixed model failed to capture the preferential diffusive-thermal instabilities in premixed turbulent hydrogen flames.

3.7. Conclusion

In this chapter the RANS turbulence models and combustion models were validated against two separate experiments performed at Paul Scherrer Institute. Both experiments were performed

with the same combustor setup. It is a symmetric cylindrical backward facing step combustor. The turbulence models were validated with flow field results obtained by Siewert (2006) using PIV.

The two turbulence models compared were the $k-\epsilon$ model and the $k-\zeta-f$ model. The $k-\epsilon$ model was observed to perform better than $k-\zeta-f$ model even though in theory the latter is better. The maximum relative error in estimation of mean velocity profile for $k-\epsilon$ model and $k-\zeta-f$ model was found to be 22.05 % and 49.79 % respectively.

The combustion experiments performed by Daniele et al. (2013) with premixed 70%/30% H_2/N_2 by vol. fuel was selected for the validation of the combustion model. The numerical simulations with the given fuel was performed at three equivalence ratios of $\phi = 0.25$, 0.35 and 0.45. The turbulence is modelled with the $k-\epsilon$ model and combustion with the well mixed model. A qualitative comparison of the results was performed by comparing the flame shape at $\phi = 0.35$ obtained with experiment and numerical simulation. The flame position predicted by the simulation had a maximum error of 33 %. The error in the flame speed estimated from the numerical simulation was observed to reduce with equivalence ratio from 50 % to less than 30 %.

The thermo-diffusive instabilities, typical of lean hydrogen flames was studied by estimating the effective Lewis number of the deficient species H_2. The laminar Lewis number at preheat temperature $T = 623\ K$ and pressure $P = 0.25\ MPa$ is around 0.36. In the presence of turbulence at a flow Reynolds number of 4.02×10^4 the effective Lewis number becomes 0.91. This observation is contradicting the findings from several experiments Wu et al. (1990) and Nakahara and Kido (1998). Thus the well mixed model could not capture the full effect of preferential diffusive-thermal instabilities in premixed turbulent hydrogen flames. This also results in under prediction of turbulent flame speed evident from the results obtained.

4

Design of Hydrogen Combustor

This chapter focuses on the design of the Aerodynamically Trapped Vortex Combustor. A sample 2-D sketch of the ATV combustor is given in figure 4.1. The flow enters the combustor through two inlets as shown in the figure. The flow through the central part of the combustor indicated by section **B'-B** is a high swirl flow and will be referenced in the rest of the document as inner flow. The flow through the section **A'-A** is non-swirling axial flow and will be referenced in the rest of the document as the outer flow.

The outer flow enters the combustor through section **A'-A** and proceeds downstream along the dome **d-e** causing a separation at the edge **c**. The separation results in the formation of a recirculation zone at the wall **b-c**. The vortex is stabilized in the section indicated by section **C'-C**. The recirculation zone helps in stabilizing the flame. Similarly the swirling flow through the section **B'-B** also stabilizes the flame by forming an inner recirculation zone as explained in section 2.5.1. These two flame stabilization zones act as the primary zones of combustion in the combustor. The combustion products from the primary zone are diluted with the dilution air further downstream of the combustor decreasing the overall temperature of the burned gas to prescribed turbine inlet temperature. Since the effect of dilution air is not considered for this analysis, the dilution holes are not depicted in the figure below.

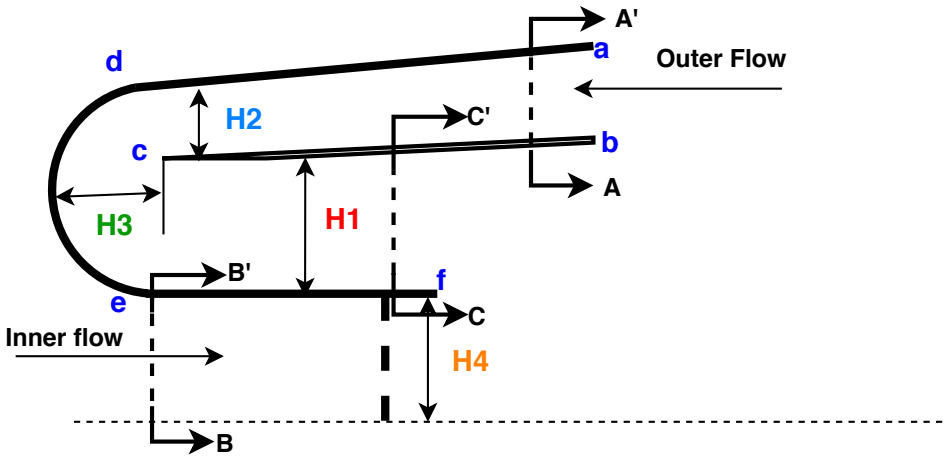

FIGURE 4.1: Schematic diagram of ATV combustor section investigated.

4.1. Basis of Design

This section describes the assumptions and criteria used to design the Aerodynamically Trapped Vortex Combustor for 100% premixed hydrogen combustion.

4.1.1. Assumptions

1. The inner flow is reduced to a non-swirling axial turbulent flow.
   The originally high swirl inner flow is reduced to a non-swirling axial flow to simplify the analysis. Since the focus of this research is on the characteristics of the outer flow, this can be considered a valid assumption. The drawback is the inability to study the interaction of the swirling flow with the outer flow. This can be considered in future studies.

2. The flow through the dome wall **d-e** is fully developed turbulent pipe flow.
   The geometry of the combustor through the section **A'-A** and **d-e** is assumed to be that of a pipe with diameter equal to width of the section at the respective position. The inlet to the outer flow is kept sufficiently upstream to assume a fully developed turbulent flow.

3. Flashback in the combustor is only due to boundary layer flashback.
   The flow through the combustor is bounded and hence the risk of boundary layer flashback is high. The core flow velocity in typical combustors are high enough to prevent core flow flashback (ref. 2.3). The absence of swirl in the outer flow removes the possibility of flashback due to combustion induced vortex breakdown. The flashback due to combustion instabilities is an important part of ultra lean combustion. But this is out of scope of this research and is recommended for future studies.

4.1.2. Design Criteria

One of the main challenges in premixed turbulent combustion of hydrogen fuel is the risk of flashback. Therefore the main requirement for the current combustor is the flashback resistance at full load conditions. In this design routine, the two quantities characterizing flashback resistance are critical velocity gradient at the wall and flashback resistance velocity.

The flame is expected to stabilize close to the separation point **c**. Thus there is a possibility of boundary layer flashback into the upstream of the corner into the outer flow. Thus the bulk flow velocity upstream of point **c** should be high enough to counter boundary layer flame flashback. The bulk flow velocity required to prevent boundary layer flashback or the flashback resistance velocity is estimated by using the modified Hoferichter's model (Hoferichter, Hirsch, and Sattelmayer, 2016)(ref 2.4.3) by Tober (2019).

Flame flashback can also occur through the dome wall represented by edge **d-e**. The combustion instabilities at the inlet to the dome could cause the flame to travel close to the dome wall. If the flow conditions in the vicinity of the dome wall is favourable for the flame to anchor, it could result in boundary layer flashback and other upstream effects due to the effects of combustion. Thus the wall velocity gradient at the dome wall should be above the critical velocity gradient (g_c) for hydrogen flames. The wall velocity gradient at the dome wall is calculated using the Blasius equation for fully developed turbulent pipe flow. The critical velocity gradient is based on the turbulent flame speed (S_T) and laminar flame thickness (δ_f). The calculations of these quantities will be explained in detail in section 4.2.2.

4.2. Design Process

In this section, the design methodology of the basic combustor geometry is explained. The design procedure can be categorized into three sections - engine performance calculations, flashback limit prediction and geometrical parameter derivation. The engine calculations are

performed by taking the engine operating conditions same as OPRA OP16-3B gas turbine. The operating condition of OPRA OP16-3B gas turbine is given in table 4.1.

Mass flow rate	8.8 kg/s
Compressor pressure ratio	6.7
Ambient pressure	1 atm
Ambient temperature	298 K
Combustor inlet temperature	$\approx$ 550 K

TABLE 4.1: OPRA OP16-3B gas turbine operating conditions

The gas turbine consists of 4 can combustors. Thus the mass flow into each combustor is calculated. While calculating the combustor inlet temperature, the effect of preheating due to wall heat transfer from the liner is taken into consideration. The design procedure for the ATV combustor geometry will be referred as 'routine' from here on.

4.2.1. Engine Calculations

The first step in engine calculations is the estimation of overall equivalence ratio or fuel/air ratio required in the hypothetical combustor at different engine loads. The calculation was performed using an in-house performance tool for the fully premixed DLN OPRA-3B combustor with 100% hydrogen fuel. For the full load or 100% load condition of 1.8 MW, the overall equivalence ratio in the combustor is calculated and the value is withheld due to confidentiality reasons.

The overall equivalence ratio gives limited information about the fuel/air composition at the primary zone. Air flow in a premixed combustor is split between the primary zone and dilution zone. The premixed mixture undergoes combustion in the primary zone and the high temperature gases are brought down to desired temperature with dilution air downstream of the primary zone. Thus the primary zone equivalence ratio is determined by the air split ratio. The air split ratio is given by equation 4.1:

$$r = \frac{\dot{m}_{\text{primary air}}}{\dot{m}_{\text{dilution air}}} \tag{4.1}$$

The preliminary combustor calculations are performed with an OPRA inhouse tool based on Cantera (Goodwin et al., 2018). The tool is a combination of fuel-air mixer and reactor network. The fuel and air are mixed at given conditions which are equal to the inlet conditions of the combustor inlet. The properties and compositions of the fuel-air mixture are calculated by the mixing tool. The resulting mixture is passed into the reactor network. The reactor network consists of a constant pressure reactor where the mixture is ignited. The exhaust gas mixture from the constant pressure reactor flows into the dilution zone where it is mixed with the cooling air. The amount of air flowing into the dilution zone is controlled by the air split ratio. The temperature of the gas at both reactor exit is recorded for further study.

The limits for air split ratio is set by two temperature constraints - primary zone temperature and turbine inlet temperature. An upper limit for fuel/air ratio in the primary zone is set by the temperature at which thermal NO_x mechanism becomes the dominant NO_x production mechanism. Thus the upper limit of temperature at the primary zone is set to 1800 K. The exit temperature at the end of dilution zone represents the turbine inlet temperature. Using the above conditions, an air split ratio is calculated and the mass flow into the outer flow and inner flow is set. The equivalence ratio of hydrogen-air mixture in the primary zone is calculated as 0.4. It results in a maximum primary zone temperature of 1656 K satisfying the primary zone temperature condition.

4.2.2. Flashback Limit Prediction

Here we look at two regions of the geometry through which boundary layer flashback is possible. The two regions are the section represented by letters **abcd**. The bulk flow velocity through the section **A'-A** to the corner **c** should be well above the flashback resistance velocity to prevent any sort of boundary layer flashback into the premixer upstream of the outer flow inlet. The second region considered is the dome wall represented by edge **d-e**. An increase in cross section area and 180^o turn in the flow causes a local decrease in velocity through this section. The critical velocity gradient criteria is applied here to predict flashback limits.

Flashback resistance velocity

To prevent flashback through the boundary layer, the flashback resistance velocity of the current setup has to be predicted. The flow through the section **A'-A** is considered as a fully developed turbulent pipe flow as explained in section 4.1.1. Therefore the modified Hoferichter's model devised by Tober (2019), Tober's model for a pipe is used to predict flashback velocity at the target equivalence ratio.

For pipe geometry, the model and experimental results are only available at an inlet temperature of $T_0 = 298K$ and inlet pressure $P_0 = 1atm$. The flashback resistance velocity (U_{FB}) is dependent on the turbulent flame speed as explained in section 2.4.2. Lin (2014) studied the pressure and temperature dependence of turbulent flame speed in high hydrogen flames. The normalized turbulent flame speed (S_T / S_{l0}) is proportional to $P^{0.84}$ and $T^{-4.7}$ where P and T are initial pressure and temperature of the unburned mixture. Lin's correlation for turbulent flame speed is given in equation 4.2.

$$S_T / S_{l0} \sim (P / P_R)^{0.84} \times (T / T_R)^{-4.7}) \tag{4.2}$$

where T_R and P_R are the reference temperature (298 K) and reference pressure (0.1 MPa) respectively. But both these relations are dominated by dependence of laminar flame speed (S_{l0}) on pressure ($P^{-0.83}$) and temperature (($T^{5.1}$). Thus the correlations formed for turbulent flame speed in Joeri's model can be used for higher temperatures and pressures with minimal error.

Critical velocity gradient (g_c)

The equation 2.8 gives the equation for critical velocity gradient. But the values of flame speed S_f at $y = y_b$ penetration depth δ_b are unknowns. Lin (2014) suggests a correlation for g_c using the characteristic velocity (S_f) as turbulent flame speed, S_T and length scale δ_b as the unstretched laminar flame width, δ_f. The effect of Lewis number on critical velocity gradient observed in Wohl (1953) is also incorporated into the correlation. The proposed equation for critical velocity gradient (g_c) is given in eq 4.3. The Lewis number is evaluated using the multi-component diffusion coefficient for the H_2-air mixture. The thus calculated Lewis number of the deficient reactant H_2 is 0.374.

$$g_c = \frac{S_T}{Le\delta_f} \tag{4.3}$$

Velocity gradient of the flow (g_f)

The velocity gradient of the flow along the dome is calculated using equation 2.3 for fully turbulent pipe flow reiterated below.

$$g_f = 0.03955 \times u_0^{7/4} \times \nu^{-3/4} \times d^{-1/4} \tag{4.4}$$

where u_0, ν and d are the bulk flow velocity at dome inlet, the kinematic viscosity of unburned mixture and diameter of pipe respectively. The diameter of the pipe, d is taken as the width

of the channel and the bulk velocity, u_0 is calculated as the bulk flow velocity for a pipe with similar diameter. A drawback of this assumption is that, the flow is not fully developed turbulent flow along the dome wall section and the estimated value of g_f contains error. Therefore the calculated velocity might not be sufficiently high enough to counter boundary layer flashback through the dome wall. The error will be estimated later during the analysis of cold flow results in section 5.4.1.

Prediction

An inverse approach as depicted in the flowchart 4.2 is followed to estimate the flashback resistance velocity, critical velocity gradient and flow velocity gradient. To reduce the complexity of calculation one of the widths in figure 4.1 is varied and other geometrical lengths $H2$, $H3$ and $H4$ are related to $H1$ by fixed ratios given in table 4.2. These ratios are derived directly from the suggestions made in Peter John Stuttaford, Jorgensen, et al. (2017).

H2/H1	H3/H1	H4/H1
0.3	0.5	1

Table 4.2: Geometrical ratios for ATV combustor (Peter John Stuttaford, Jorgensen, et al., 2017).

4.2.3. Geometric Parameter Calculation

In the current approach the length $H2$ is representative of the diameter of the pipe for flashback resistance velocity calculation. The width $H3$ is used as diameter of pipe for flow velocity gradient calculation along the dome wall. The initial known parameters of mixture temperature, pressure, and equivalence ratio are set according to the results obtained from the engine calculations.

After setting all the inlet conditions, an initial value for the length $H1$ is assumed. Using this value and the ratios given in table 4.2 and the fixed mass flow rate, the velocity of the fuel-air mixture (V_f) through the combustor inlet is calculated. Parallel to this step, using the fixed fuel equivalence ratio derived from the engine calculations and a pipe diameter of $H2$, the flashback velocity is calculated. The bulk flow velocity through the section and the flashback velocity are then compared to satisfy the condition $V_f > 2.0\ V_b$. A safety limit of 2.0 times the predicted flashback velocity is set to account for preferential diffusion, improper mixing, combustion instabilities, adverse pressure gradients and possible errors in the prediction model.

For calculating the flow velocity gradient, the bulk flow velocity at the inlet to the dome section needs to be estimated. This is estimated using the continuity equation. Neglecting the compressibility effects, the bulk flow velocity at dome inlet (V_D) is given by:

$$V_D = V_f * A_2 / A_3$$

where A_2 and A_3 are cross sectional area of section at the combustor inlet and dome inlet respectively. The presence of flame increases the temperature of the fluid and decreases the density. Thus the local flow velocity will be higher than the estimated value according to the continuity equation. This results in higher wall velocity gradient and decreases the chance of boundary layer flashback. The calculated flow velocity gradient (g_f) needs to be greater than the critical velocity gradient (g_c) for hydrogen flames. Therefore, the second criteria is given as $g_f > 2.0\ g_c$. Similar to the above condition, a safety factor of 2.0 is set for this condition also.

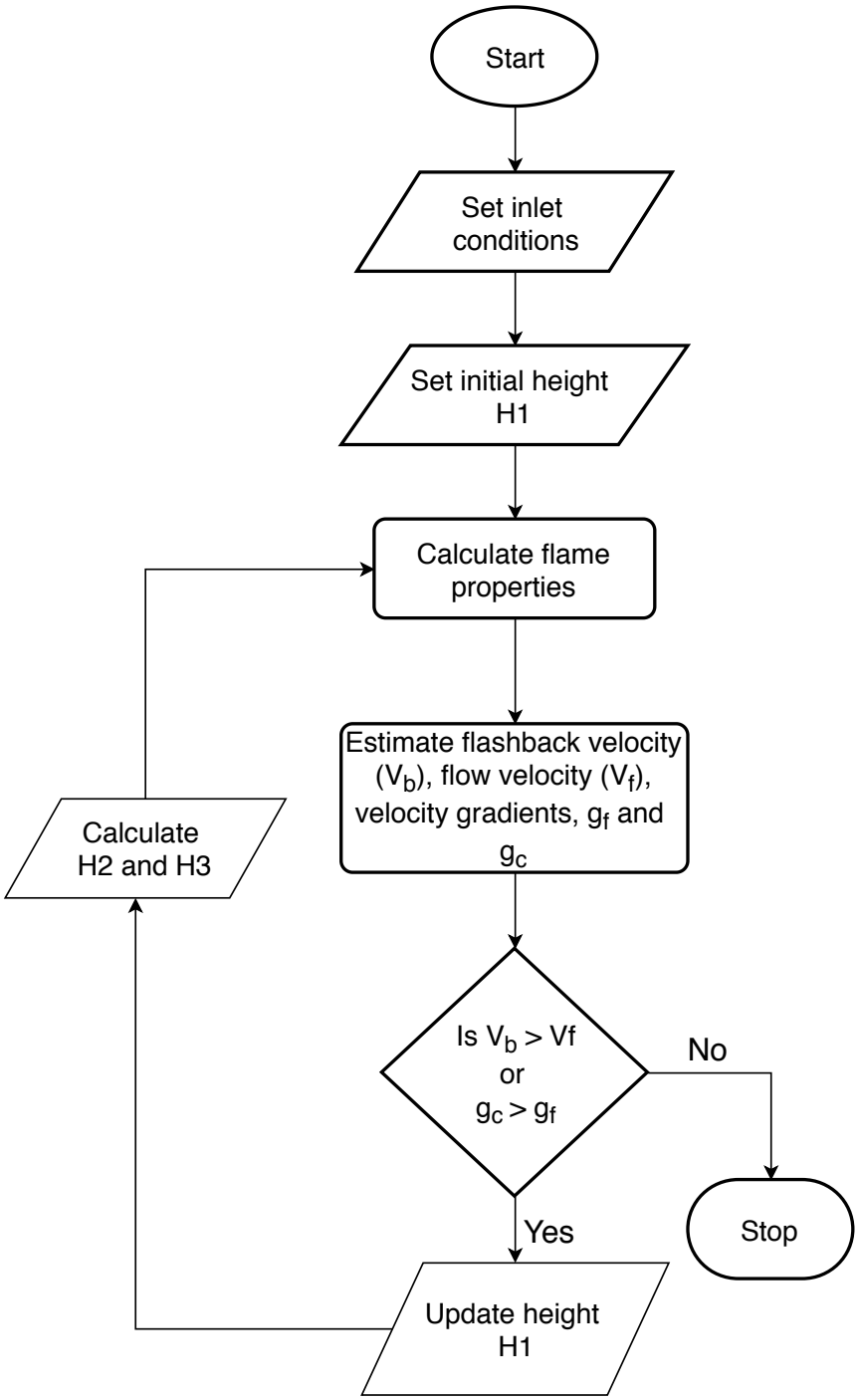

FIGURE 4.2: Flowchart for geometry calculation.

The length $H1$ (in mm) is incremented or decremented based on the condition given in eq. 4.5. The algorithm converges when one of the conditions are satisfied.

$$\text{if } V_f < 2.0 \times V_b \text{ or } g_f < 2.0 \times g_c \text{ then } H1 = H1 - H1/100 \text{ else } H1 = H1 + H1/100 \tag{4.5}$$

With the above condition, the length $H1$ (in mm) is calculated at different equivalence ratio (ϕ) and similar inlet flow conditions. The variation of estimated $H1$ with ϕ is given in figure 4.3. The critical velocity gradient calculated using Lin's model (Lin, 2014) on the dome wall

imposes a stricter limit on the geometry than the Tober's model. Thus the flashback resistance velocity calculated using Lin's model is higher than the values obtained with Tober's model.

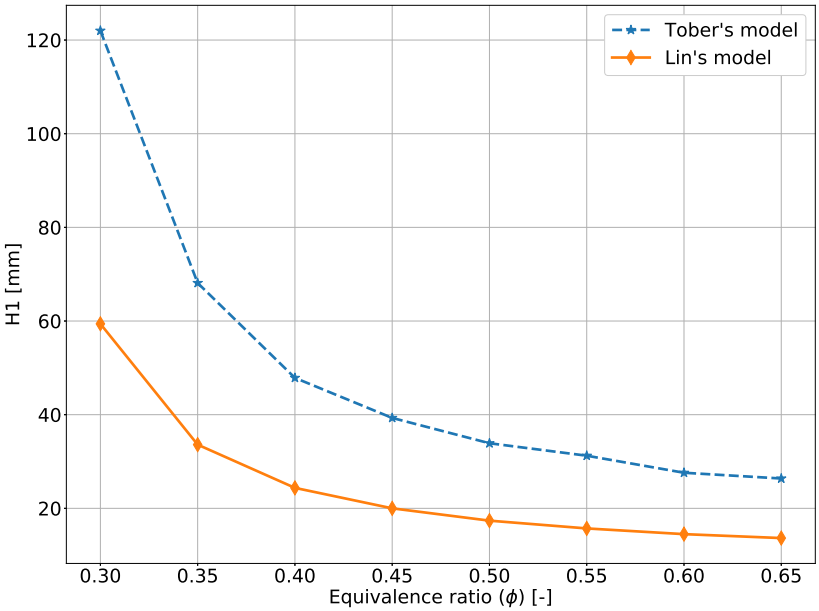

FIGURE 4.3: Variation of width H1 calculated with equivalence ratio.

4.2.4. Final Geometry

The inlet conditions and the converged results from the routine is listed in table 4.3. The geometry is calculated using the value of $H1$ obtained at $\phi = 0.4$. This value satisfies the flashback resistance condition upstream of point **c** for equivalence ratio till $\phi = 0.65$ (fig. 4.3).

The 2D sketch of the ATV combustor with the calculated parameters is shown in figure

Inlet conditions		**Results**	
Quantity	Value	Length	Value [mm]
Inlet temperature (T_0)	550 K	H1	25
Inlet pressure (P_0)	6.7 atm	H2	8
Mass flow rate ($\dot{m}$)	0.65 kg/s	H3	13
Equivalence ratio (ϕ)	0.4	H4	25

TABLE 4.3: Input and output from the geometry selection routine.

4.4. The separation point is represented by point **G**. The contoured liner represented by **FGH** follows the same design as the optimized contoured liner presented in Peter John Stuttaford and Rizkalla (2018) for ideal separation. The length of the combustor is taken as 2 times the diameter of the liner. The dome is represented by edge **BC**. This section is made out of three arcs of different radius. The radius and centre for each arc is selected so as to keep an almost constant normal distance from the separation point **G**.

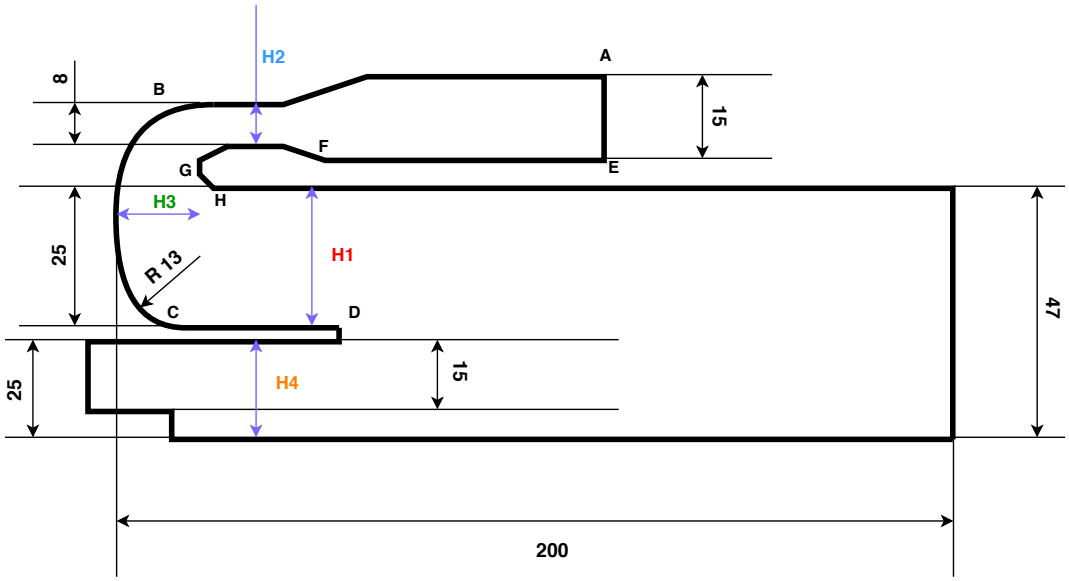

FIGURE 4.4: 2D sketch of ATV Combustor (all lengths in mm).

5

Aerodynamically Trapped Vortex Combustor

This chapter looks into the flow behaviour and flame stabilization mechanism in Aerodynamically Trapped Vortex (ATV) combustor. The chapter starts with detailed description of the numerical setup and boundary conditions used for the analysis. The general setup remains similar to the validation case and the MAD model is used for solving species transport equations.

The study of flow behavior involves performing cold flow simulations and sensitivity analysis on the combustor. The parameters varied in the sensitivity analysis are inlet mass flow rate or inlet velocity and inlet turbulence intensity. The flow characteristics of focus in this study are total velocity, turbulence intensity and wall velocity gradient (g_f).

In the second part of the chapter, the results from the reactive flow simulations with 100 % premixed hydrogen fuel is discussed. The effect of flame on the trapped vortex and critical velocity gradient is studied. The combustion regime of the flame is also identified in the analysis.

5.1. Numerical Setup

A method similar to that followed in the validation cases is followed for ATV combustor simulations. From the 2-D sketch in figure 4.4 a 45^o section of the combustor is created to run all the simulations. A 3D view of the CAD geometry is shown in figure 5.1.

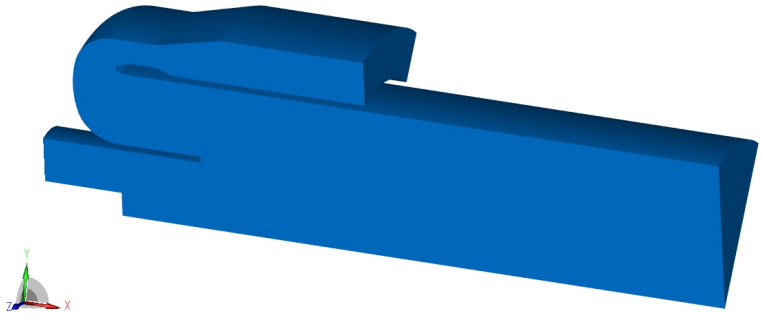

Figure 5.1: CAD geometry of the domain selected for ATV combustor simulations.

A structured mesh setup is selected for meshing the domain. The whole domain is meshed with constant cell width and refinements are applied at corners to better capture the complex parts of the geometry. Since the exact flame position is not known *a priori*, refinement is not performed for reactive flow simulations. Although an adaptive mesh refinement method is recommended in further studies. A summary of the numerical setup is given in table 5.1 below. Cold flow simulations are run with standard $k-\epsilon$ model. The selection of the turbulence

	Cold Flow	Reactive Flow
Run mode	Steady	Unsteady
Discretization Scheme	SIMPLE	SIMPLE
Differencing Scheme		
Momentum	AVL Smart Bounded	AVL Smart Bounded
Continuity	Central Differencing	Central Differencing
Turbulence	AVL Smart Bounded	AVL Smart Bounded
Energy	Not activated	AVL Smart Bounded
Convergence Criteria	1e-5	1e-5

TABLE 5.1: Numerical setup for ATV combustor simulations.

model was based on the results from the validation studies explained in section 3.7. Similarly the reaction simulations are performed with the final model (detailed chemistry with mixture averaged diffusion) as suggested in section 3.7. The 9-species, 19 reaction H_2/O_2 mechanism devised by Li et al. (2004) is selected as the reaction mechanism for all the reaction simulations.

5.2. Boundary Conditions

A 2D sketch of the geometry with color coded types of boundary at each face is given in figure 5.2. Flow enters the combustor through the outer flow inlet and the inner flow inlet. In the current study, fuel is mixed with the outer flow and the inner flow is kept as air. The mixture undergoes reaction inside the combustor and the burnt gases exits through the outlet. Symmetric boundary conditions are imposed on both lateral sides of the 45^o section. Table

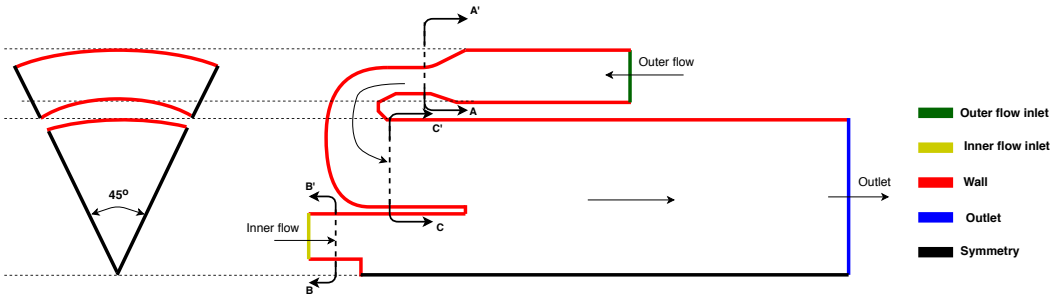

FIGURE 5.2: Type of boundary condition on the ATV combustor depicted by 2D sketch.

5.2 gives an overview of the boundary conditions imposed on the domain for the cold flow simulations. A brief discussion of the choices made for each boundary condition will follow the table. The inlet conditions at the outer flow and inner flow mass flow inlet are same. The inlet temperature of the mixture at both inlets are set to 550 K. An inlet turbulence of 5% is given at both inlets. The outlet pressure is set to 6.7 atm.

The reactive cases are performed with 100% hydrogen-air mixture. It is assumed that the flow into the trapped vortex region is completely premixed. Therefore the outer flow inlet is

Cold Flow/ Reactive Flow				
	Outer flow inlet	Inner flow inlet	Outlet	Wall
Type	Mass flow inlet	Mass flow inlet	Pressure Outlet	No slip wall
Mass flow [kg/s]	0.08125	0.08125	-	0
Pressure	-	-	6.7 atm	-
Temperature	550 K	550 K	-	Isothermal/ Adiabatic
Turbulent Intensity	5%	5%	-	-

TABLE 5.2: Summary of boundary conditions for ATV combustor cold flow simulations.

set as premixed $H_2 - air$ mixture with equivalence ratio of 0.4. Using the fuel equivalence ratio of 0.4, the mole fractions of the gases in the mixture was calculated and given as inlet mole fraction at the inlet. The species and their respective mole fractions at the inlet is given in table 5.3.

Species	H_2	H	O_2	O	OH	H_2O	HO_2	H_2O_2	N_2	Ar
Mole Fraction	0.1438	0	0.1797	0	0	0	0	0	0.6685	0.008

TABLE 5.3: Species mole fraction of the fuel-air mixture at the inlet.

Similar to the validation case, the whole domain is initialized with premixed fuel-air. A spherical ignition source is placed at the position indicated by point A as shown in figure 5.2. The properties of the ignition source is given in table 5.4. The flow was ignited at the given location at 0.5 ms into the simulation for a duration of 4.5 ms. A higher energy factor was required to properly ignite the mixture and get the combustion started. The wall boundary condition was changed to a no-slip adiabatic wall. All the other boundary conditions remains similar to the cold flow case.

Location [mm]			Radius [mm]	Energy factor
x	y	z		
27.5	37.5	0	8.75	1.75

TABLE 5.4: Properties of ignition source for ATV combustor reactive simulations.

5.3. Mesh Independence

A mesh independence study was performed to select the right grid size for the simulations. Four structured meshes with number of cells of 0.85 MM, 1.6 MM, 2.5 M and 3.5 MM are generated using AVL FAME. The wall grid spacing is set to 1×10^{-6}. For the set wall grid spacing, the y^+ value along the dome wall is given in figure 5.3. The minimum y^+ along the wall is approximately 10 and the maximum is 30. Therefore the wall adjacent grid height reside in the log law region and the wall functions retain their validity.

The mesh shown in figure 5.4 consists of 2.5 MM cells with nearly 95% hexahedral elements. The setup for the mesh independence study is same as the numerical setup detailed in the above section. For turbulence modelling, the $k - \epsilon$ model was used with standard wall functions. From the converged results, total velocity was sampled at the locations shown in figure 4.4. The results of the study performed are shown in figure 5.5. From the results it can

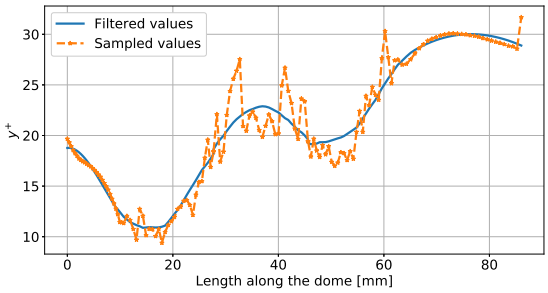

FIGURE 5.3: Sampled and filtered y^+ along the dome wall

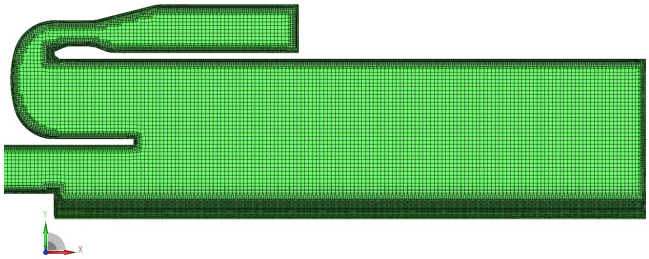

FIGURE 5.4: Structured mesh with around 2.5 million cells.

be inferred that the results are independent above the mesh size of 2.5 MM cells. Therefore subsequent studies are performed with this mesh.

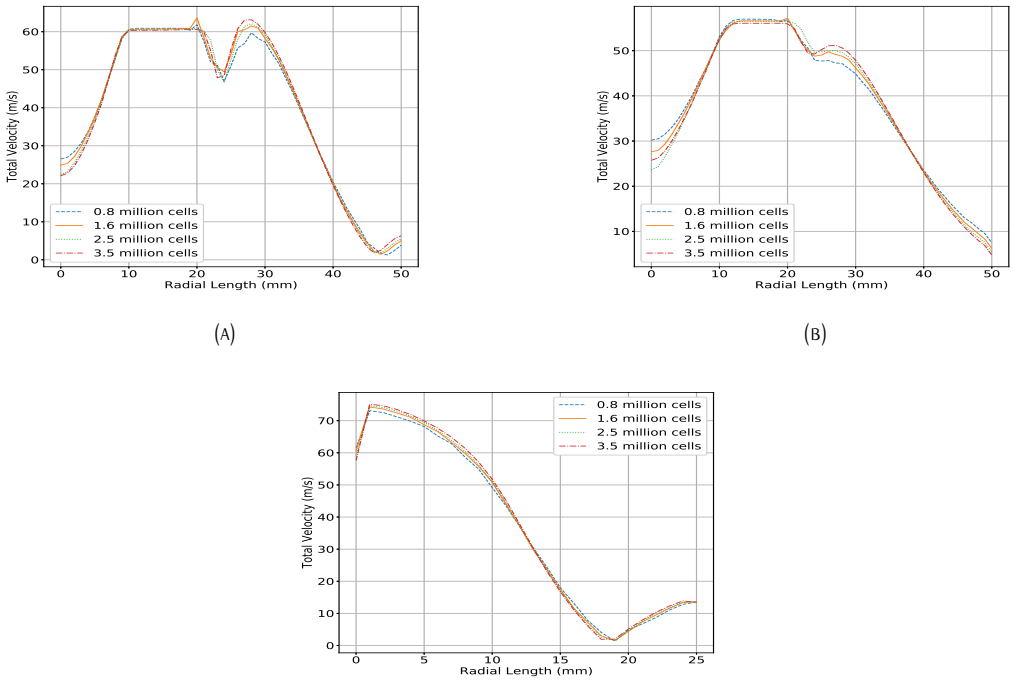

(A) (B)

(C)

FIGURE 5.5: Velocity data obtained at axial locations. A : x=74 mm; B: x=100 mm; C: x=130 mm.

5.4. Results

This section presents the results obtained from a number of simulations performed on the ATV combustor. First section 5.4.1 covers the cold flow results with sensitivity analysis for inlet mass flow rate and inlet turbulence. Primary focus is given to the dome wall where the possibility of flashback is high. Since the geometry is fixed, the inlet mass flow rate is varied to study the effect of inlet bulk velocity on the flow dynamics along the dome wall and recirculation zone. Another factor considered is the inlet turbulence which varies in a real combustor inlet due to different factors.

The second section 5.4.2 studies the flame stabilization mechanism and effect of hydrogen-air reaction on the flow in the combustor. The effect of fuel concentration on the combustion dynamics is also studied by varying the equivalence ratio.

5.4.1. Cold Flow

The first set of analysis was performed with the boundary condition given in table 5.2. This was performed to study the general flow behaviour in the ATV combustor. The quantities of interest were the wall velocity gradient, size of recirculation bubble and flow velocity along the dome.

The total velocity contour and the streamlines are shown in figure 5.6. The flow enters the combustor through the outer flow inlet at a bulk flow velocity of 28 m/s. The flow then accelerates through the section A'-A to a maximum velocity of 67 m/s upstream of the separation point due to change in area of the inlet pipe. Such high velocity near the separation point are critical for avoiding flashback through that location.

The flow separates at the corner and enters the dome section. In the dome the flow quickly decelerates towards the wall in radial direction. The flow reattaches at a length of around 60 mm downstream of the separation point. The recirculation bubble formed covers almost half of the flame stabilization zone. The low velocity flow through the dome accelerates through the section C'-C due to the constriction caused by the recirculation zone. The high velocity region formed between the recirculation bubble and the wall prevents the flame from reaching the wall reducing the chance of flashback through that section.

The core inlet flow through section B'-B is assumed to be non-swirling axial flow. The flow through this part of the combustor is similar to the flow in validation case. Thus a small recirculation zone is formed at the axis of the combustor. The streamlines reveal that the flow is parallel at the interface between the flow coming from the outer flow inlet and the inner flow inlet. Changes in inlet condition at both inlets might cause a deviation from this behaviour. This factor must be taken into consideration while designing the combustor.

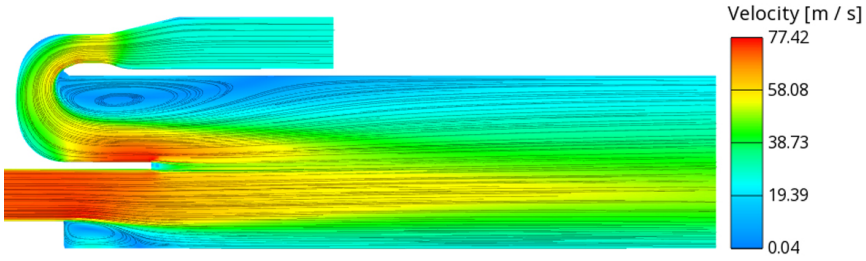

Figure 5.6: Velocity contour with streamlines in ATV combustor.

The mean velocity and the turbulent velocity fluctuations along the 5 lines is plotted in figure 5.8. The sampling lines A-E are marked in figure 5.7. The velocity is scaled with inlet bulk velocity of 28 m/s. The flow decelerates to very low velocities near the wall downstream of point A. The minimum velocity near the dome wall is almost 10 m/s. After reaching a minimum, the flow accelerates through the middle of the dome before slowing down along the

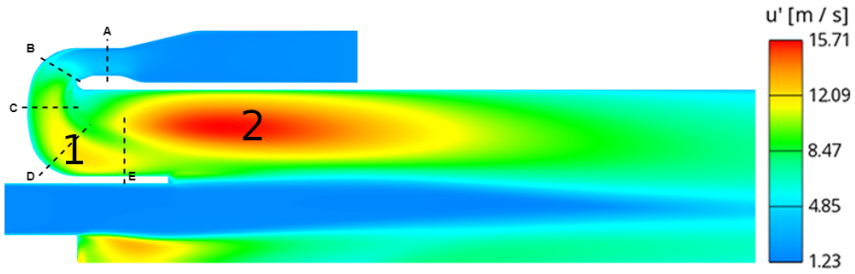

FIGURE 5.7: RMS turbulent velocity fluctuation contour in ATV combustor.

final corner of the dome. At the final corner, the reduction in velocity is similar to that in the first corner. Even though the flow velocity increases further away from the wall, the velocity gradient along the dome is critical.

The turbulent velocity contour is shown in figure 5.7. A sickle shaped shear layer 1 is formed downstream of the separation point along the dome. The shear layer is initially thin and increases in width along the dome to point D. Another high turbulence zone (zone 2) is formed near the recirculation zone. It has an elliptical shape with a length of almost 3 times the width of the section **C'-C**. Further downstream the turbulence decreases due to dissipation. The variation in turbulence along the dome wall can be observed from the figures 5.8a - 5.8e. The turbulence increases along the dome wall from line A to line B. From line C to line E the turbulence in the shear layer dictates the turbulence in the flow and the turbulence intensity remains almost constant at 40 %. A peak in turbulence is observed on line D which falls in the middle of shear layer 1.

The variation in wall velocity gradient along the dome wall is shown in figure 5.9. The wall velocity gradient is calculated using the velocity parallel to the wall at two boundary grid layers near the wall. Between points B and D, the minimum wall velocity gradient reaches a values of around 1×10^4 with the values staying below 4×10^4. Referring to figure 2.4, these values are well below the predicted critical velocity gradient (g_c) of 1.09×10^5 estimated in the design process 4.2.2. Low velocity regions combined with wall velocity gradient below g_c, combustion instabilities at the section A'-A could cause the flame to travel closer to the dome wall. This increases the risk of boundary layer flashback and localized burning of the mixture near the dome wall.

Effect of inlet velocity

The effect of the inlet velocity on the flow characteristics is studied by varying the inlet mass flow rate. Apart from the reference case analysed in previous section, simulation were run for two mass more mass flow rates higher and lower than the reference case.

The influence of U_{bulk} on relative turbulence intensity (u'/U_{bulk}) and the relative mean axial velocity (U_{center}/U_{bulk}) are shown for inlet mass flow rate variation from 0.6 kg/s - 0.8 kg/s in figure 5.10. For all 3 mass flow rate cases, both axial profiles of u'/U_{bulk} and U_{center}/U_{bulk} collapse on one curve. This indicates that u' and U_{center} are proportional to the inlet bulk velocity or the inlet mass flow rate. Higher velocities lead to higher velocity gradients in the shear layer. These higher velocity gradients which roughly scale linearly with the inlet velocity are responsible for production of turbulence.

In figure 5.11, the influence of U_{bulk} on wall velocity gradient (g_f) is shown for the same variation in mass flow rate. The wall velocity gradient increases slightly with increasing mass flow rate or increasing bulk flow velocity. This behaviour is expected since increase in bulk flow velocity in a bounded flow increases the wall velocity gradient.

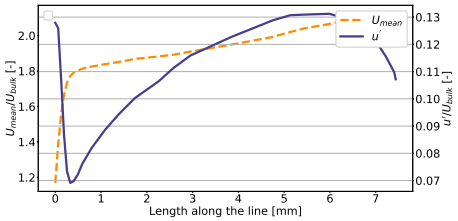

(A) Line A

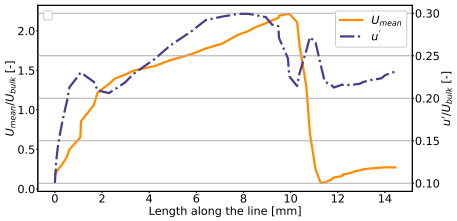

(B) Line B

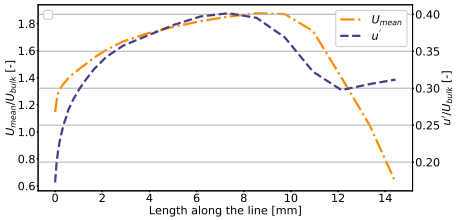

(C) Line C

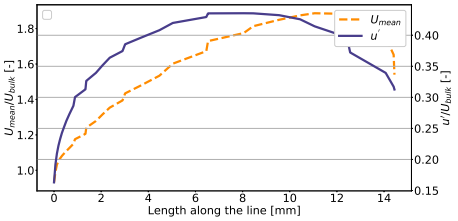

(D) Line D

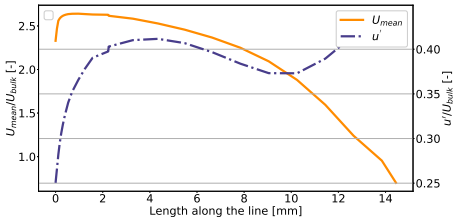

(E) Line E

FIGURE 5.8: Variation of total velocity and turbulent velocity fluctuations along the radial lines A to E.

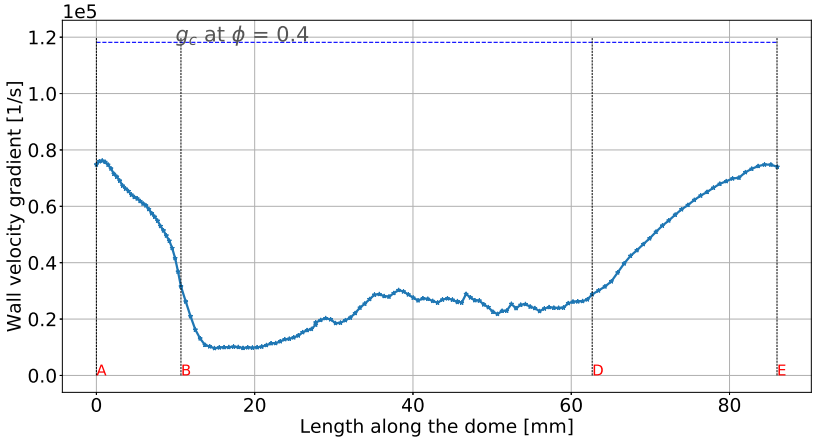

FIGURE 5.9: Velocity gradient along the dome wall.

Effect of inlet turbulence

The effect of inlet turbulence on the flow characteristics is studied by varying the inlet turbulence intensity from 6 % - 24 % and keeping all other inlet conditions similar. Figure 5.12 shows the effect of this variation on the scaled center-dome velocity (U_{center} /U_{bulk}) and relative turbulence intensity (u'/U_{bulk}) along the lines from A - E.

The change in inlet turbulence has no effect on the mean velocity along the radial lines. On the other hand the variation in inlet turbulence has significant effect on the u'/U_{bulk}

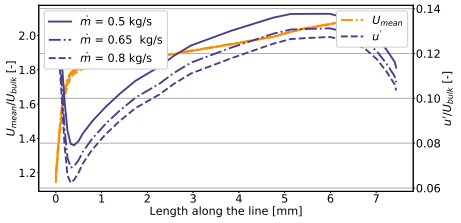

(A) Line A

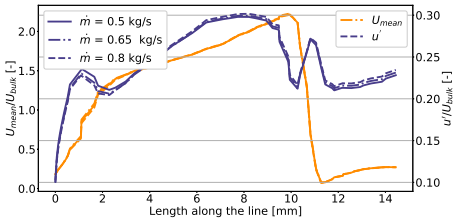

(B) Line B

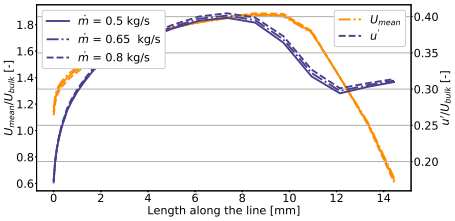

(C) Line C

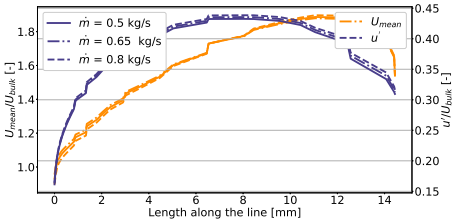

(D) Line D

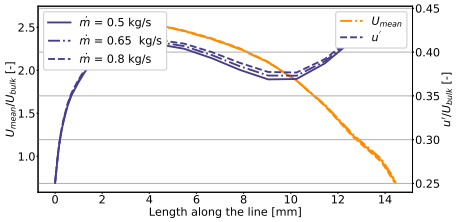

(E) Line E

FIGURE 5.10: Sensitivity of total velocity and turbulent velocity fluctuations along the radial lines A to E to change in mass flow rate.

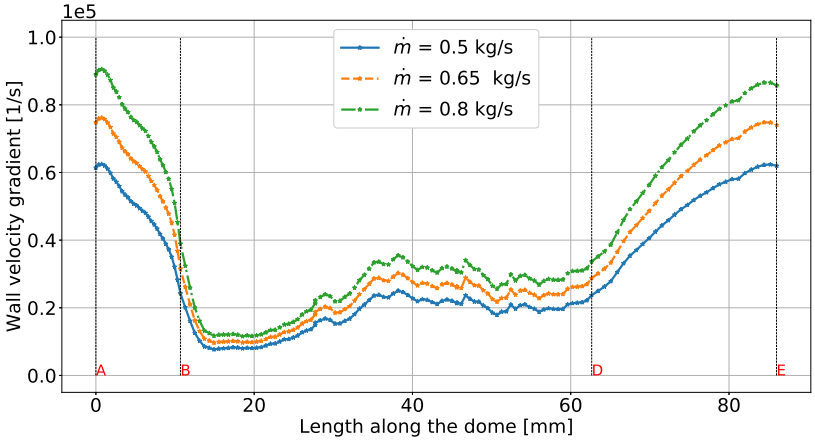

FIGURE 5.11: Variation in velocity gradient along the dome wall with outer flow mass flow rate.

profile. The effect is visible for section A-C and partially in section C-D. From point A to C the increase in inlet turbulence increase the turbulent intensity along the radial lines. From C to D the presence of shear layer 1 masks the turbulence in the inlet. Thus downstream of point C, the effect of inlet turbulence reduces gradually and the shear layer turbulence completely dominates from point D.

The flame stabilization is enhanced by intense turbulence transport and mixing of hot

combustion products into fresh mixture. Therefore the flame stabilization can be influenced by changing the turbulence in the shear layer. But changing the inlet turbulence seems to have little effect on the shear layer turbulence. Thus other methods have to be sought to influence the turbulence at the flame front.

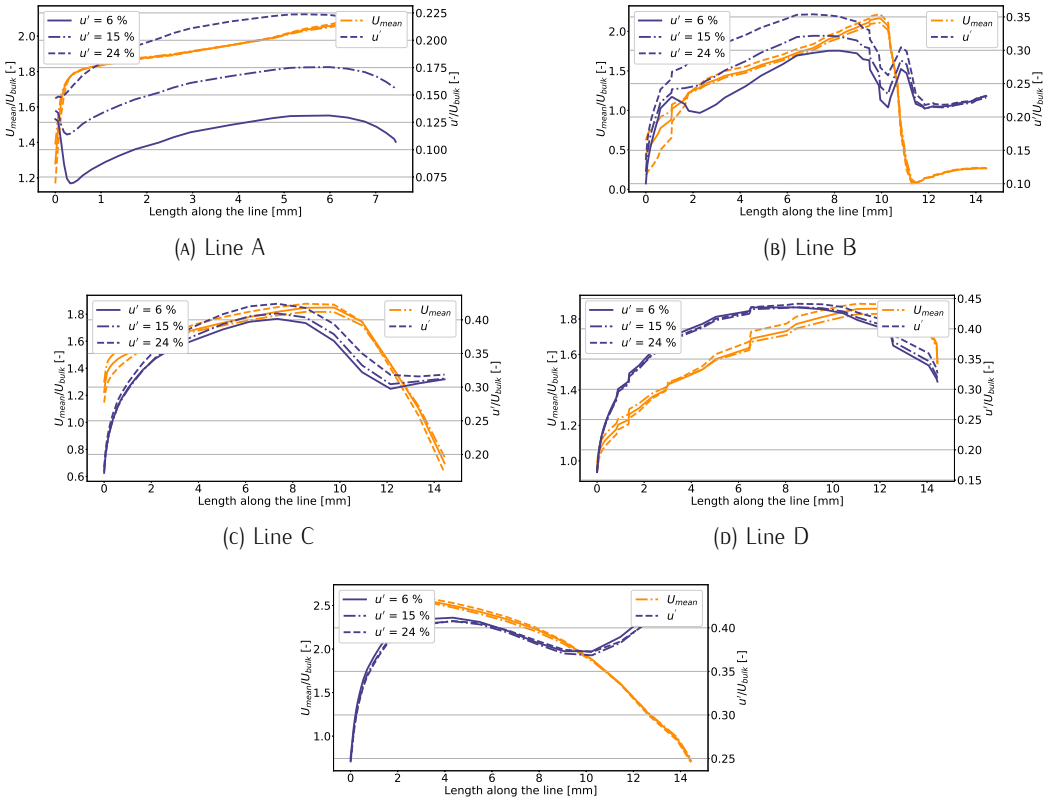

(A) Line A

(B) Line B

(C) Line C

(D) Line D

(E) Line E

FIGURE 5.12: Sensitivity of total velocity and turbulent velocity fluctuations along the radial lines A to E to change in inlet turbulence.

Similar to previous sensitivity analysis with inlet velocity, the effect of inlet turbulence on wall velocity gradient along the dome is also analysed. A visible change in values of wall velocity gradient is seen for length of dome $l_d < 30mm$. For an 5 times increase in turbulence intensity, a 100% maximum increase in wall velocity gradient is seen at $l_d = 15mm$ For $l_d > 30mm$ the shear layer turbulence masks the effect of inlet turbulence and the wall velocity gradient curves collapses on one curve. The ability to change wall velocity gradient along the dome wall is important to prevent flashback. From this analysis it can be concluded that changing inlet turbulence only effects less than half of the dome wall and the values downstream of this point is dictated by the turbulence in the shear layer.

5.4.2. Reactive Flow

The reactive flow simulations for 100% premixed hydrogen was run for two fuel equivalence ratio - 0.4 and 0.5. The flame stabilization and reactive flow characteristic are analysed using the reference case with $\phi = 0.4$. The numerical setup and boundary conditions for the simulations are explained in section 5.1 and 5.2 respectively. The time evolution of the unsteady RANS simulation is given in figure 5.14. The mixture is ignited at 0.5 ms for a period of 4.5 ms. The solver runs for another 15 ms for the fluctuations to settle and the data collection starts at 20 ms for a period of 30 ms. Thus all the results presented henceforth are based on quantities averaged from the data collected over the last 30 ms of the simulation.

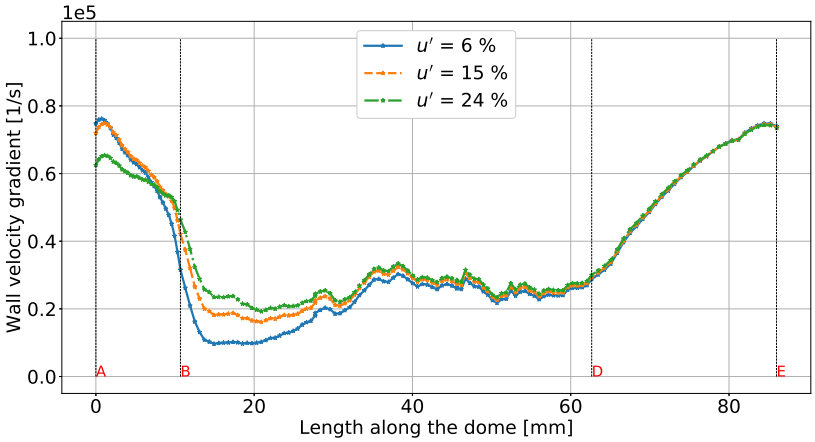

FIGURE 5.13: Variation in velocity gradient along the dome wall with outer flow inlet turbulence.

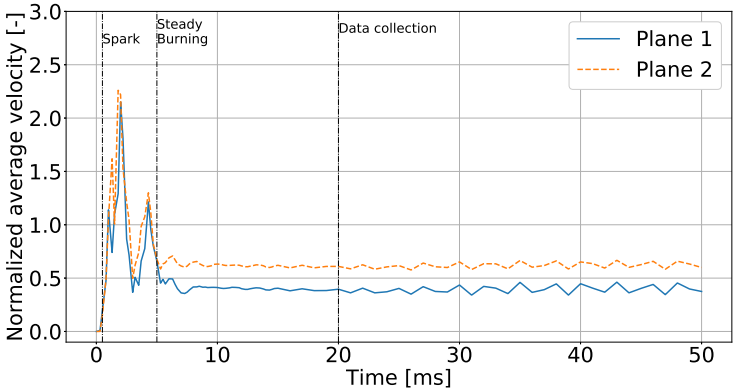

FIGURE 5.14: Time evolution of reaction simulation for ATV combustor.

Combustion Regime

The combustion regime of the two flames at equivalence ratio $\phi = 0.4$ and 0.5 is identified in this section. The parameters required for the process are the laminar flame parameters, laminar flame speed (S_l) and laminar flame thickness (δ_l) and turbulent flow properties, integral length scale (L_t) and turbulent fluctuations ($u^{'}$). These parameters are calculated at progress variable $c = 0.05$ similar to validation case 3.6.2 and averaged over the entire flame length. The results of this calculation are shown in figure 5.15 where the two reactive cases are plotted as points in the Borghi-Peters diagram.

Both flames falls under the thin reaction zones indicating that the Kolmogorov scales is smaller than the flame thickness and scalar mixing is enhanced in the preheat zone. The decrease in equivalence ratio moves the flame away from the $Ka = 1$ limit. The case with $\phi = 0.4$ lies left of $Da = 1$ in the well stirred reactor zone. The well mixed model works better for flames in this region and thus the results from this case contains less relative error than the $\phi = 0.5$ case. As the fuel gets leaner, the combustion model gets more and more accurate.

Flame Stabilization

To identify the flame stabilization mechanism, the OH mole fraction distribution for the two reactive cases are displayed in figure 5.16. The flame looks similar to the V-flame in the PSI combustor studied in section 3.6. Thus the flame is stabilized because of the recirculation of

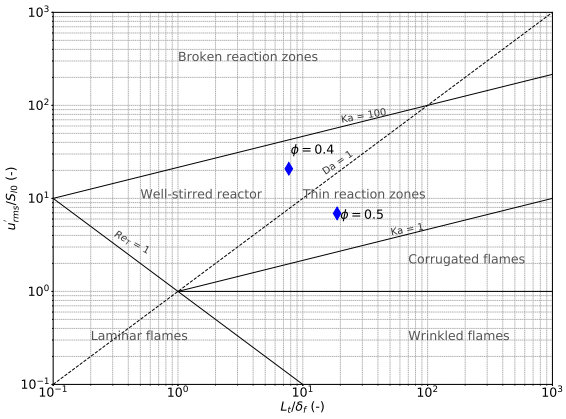

FIGURE 5.15: Combustion regime for the flames in ATV combustor.

hot products by the trapped vortex formed at the wall of the combustor. The flame is anchored

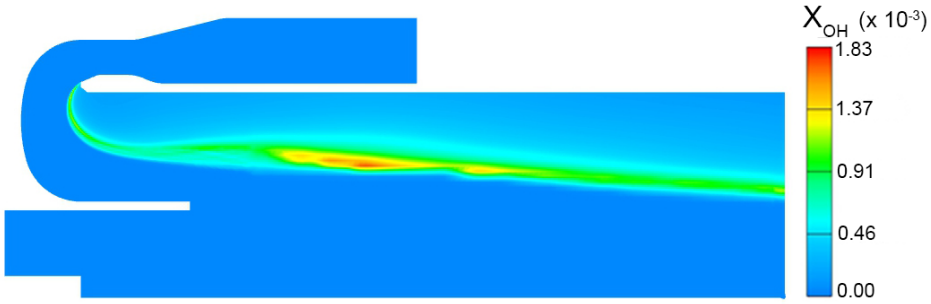

(A) $\phi = 0.4$

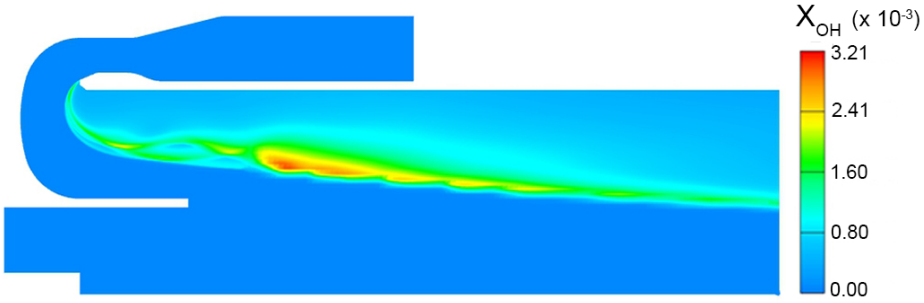

(B) $\phi = 0.5$

FIGURE 5.16: OH mole fraction contours for ATV combustor

from the separation point starting as a thin flame and increasing in thickness as we move away from the separation point. It can also be observed that the flame moves closer towards the axis with increase in equivalence ratio. Moving closer to the axis decreases the total length of the flame and increases the turbulent flame speed. Figure 5.17 shows the mole fraction contour for hydrogen at $\phi = 0.4$ for the ATV combustor. The exhaust of the present combustor contains hydrogen. This can be due to several reasons. One of the primary reasons is the under-prediction of reaction rates by the combustion model and thus not all all fuel is burned. Another reason can be the insufficient length of the combustor to burn all the fuel resulting in incomplete combustion. Absence of core flow combustion can also be cited as one of the reasons. Reaction can be quenched by the cold flow from the core flow and reduce

the reactivity of the flame. It is expected that a hot swirling core flow flame would interact with the outer flame and help in burning all the fuel. The flame would be closed instead of an open flame extending towards the combustor exit in this case.

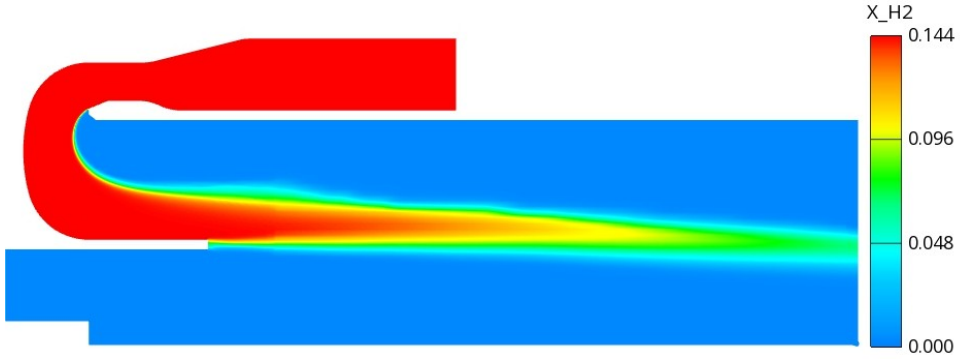

FIGURE 5.17: H_2 mole fraction contour for ATV combustor at $\phi = 0.4$.

Wall Velocity Gradient

The total velocity contour with the streamlines are shown in figure 5.18. The result shown corresponds to the case with equivalence ratio of 0.4. Due to the presence of flame the flow heats up and the kinetic energy increases. This results in acceleration of the flow close to the flame front. The presence of flame also caused upstream effects on the flow near the dome wall. The wall velocity gradient on the dome wall with and without the flame for three

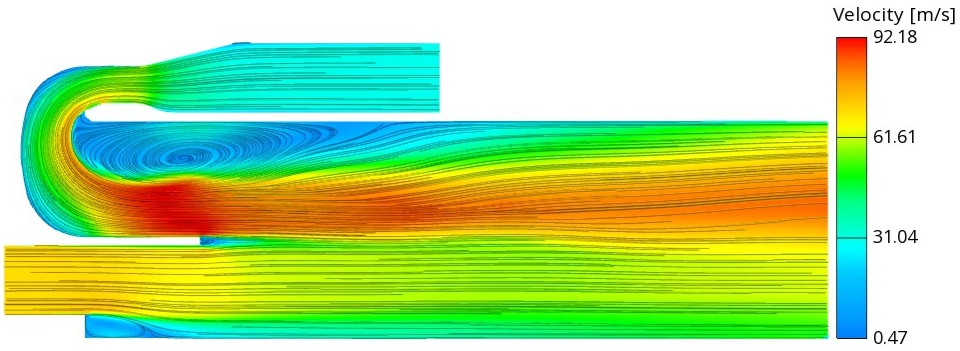

FIGURE 5.18: Velocity contour at $\phi = 0.4$.

cases are shown in figure 5.19. The $\phi = 0$ case corresponds to results from the cold flow for comparison. The flame has limited effect on the wall velocity gradient at the section from A to B. Downstream of point B, the wall velocity gradient increases by an order of magnitude and is well above the critical velocity gradient of 1.09×10^5 estimated for hydrogen flames in the design process. The wall velocity gradient also increases by a small percent with increase in equivalence ratio. Extrapolating the data, the wall velocity gradient is expected to decrease with decrease in equivalence ratio. Estimation of this change is important since this affects the startup of the combustor from zero load to full load.

5.5. Conclusion

This chapter comprised the detailed analysis of Aerodynamically Trapped Vortex (ATV) combustor for 100 % hydrogen operation. The preliminary design of the combustor was based on the critical velocity gradient of premixed turbulent hydrogen flames at critical points in the combustor.

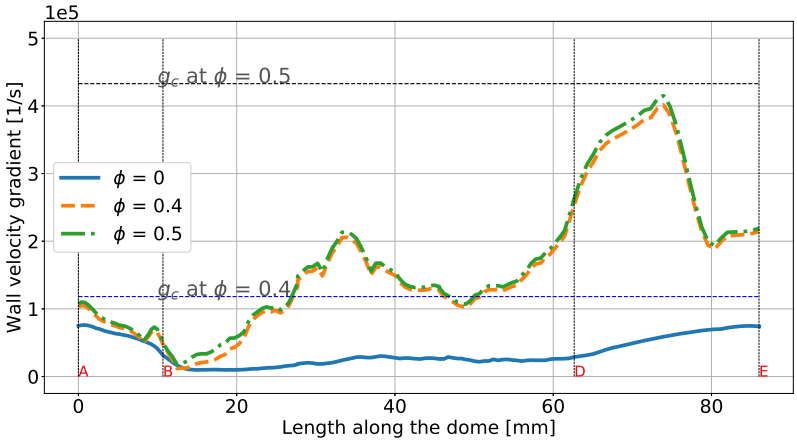

FIGURE 5.19: Variation in velocity gradient along the dome wall due to presence of hydrogen flame.

A set of cold flow simulations were performed on the ATV combustor. The section with the highest risk for flashback is the dome wall. The flow velocity gradient in this section is one order of magnitude less than critical velocity gradient for hydrogen flames. The combustor contains two shear layer zones, one at the dome wall and another near the recirculation bubble. The recirculation zone helps in recirculating the combustion products to stabilize the flame.

A sensitivity analysis was performed by varying the inlet turbulence and inlet velocity into the combustor. Both parameters have minimal effect on the wall velocity gradients and flow parameters at the dome wall and recirculation zone. Thus other methods have to be sought to control the flow parameters at these sections.

Reactive flow simulations were performed at equivalence ratios $\phi = 0.4$ and 0.5. Both flames falls under the thin reaction zone in the Peters diagram. The flame anchors from the separation point and extends till the exit of the combustor. The presence of flame increased the wall velocity gradient in the second half of the dome wall above critical velocity gradient.

6

Conclusions and recommendations

Hydrogen combustion for energy production provides a pathway to smooth transition from conventional fuels to renewable energy. In addition to elimination of carbon emission, using a premixed type of combustion minimizes the harmful NO_x emissions. Premixed turbulent hydrogen combustion is met with the challenge of flame flashback due to the inherent properties of hydrogen flames discussed in chapter 2. The combustion modelling of premixed hydrogen flames are also challenging due to preferential diffusion and Lewis number effects. To tackle the challenge of flame flashback a combustor design based on trapped vortex flame stabilization concept was proposed and analyzed. The turbulence and combustion models used in this research is also validated against premixed turbulent hydrogen flames in a axial dump stabilized combustor (Siewert, 2006; Daniele et al., 2013). This chapter draws important conclusion from this research in section 6.1 followed by recommendations in section 6.2.

6.1. Conclusions

This section is divided into two parts - validation of numerical models (sec. 6.1.1) and analysis of hydrogen combustor (sec. 6.1.2).

6.1.1. Validation of numerical methods

The turbulence model and combustion models were validated using the experiments performed by Siewert (2006) and Daniele et al. (2013) respectively. The turbulence models used were $k-\epsilon$ and $k-\zeta-f$ models. The well mixed model was used for modelling the combustion.

1. For non-swirling flows backward facing step flows, the $k-\epsilon$ model performed better than the $k-\zeta-f$ model. The maximum error in estimation of mean axial velocity along the centerline of the combustor using $k-\epsilon$ and $k-\zeta-f$ models were 22.05 % and 49.79 % respectively. The $k-\zeta-f$ model was found to be too dissipative than the $k-\epsilon$ model. Since the $k-\zeta-f$ model involved solving two additional equation compared to $k-\epsilon$ model, it is much more computationally expensive.

2. The $k-\epsilon$ model was able to predict the mean velocity and turbulence intensities over a large part of the domain. It showed large deviations in turbulence prediction from the experimental results beyond $3/4^{th}$ length of the combustor and in the recirculation zone. Nevertheless it performed significantly better than the $k-\zeta-f$ model.

3. The well mixed model used for modelling combustion failed to capture the exact flame front for the case with $\phi = 0.35$. As the turbulent flame speed decreases, the flame becomes longer. The numerical results showed a longer flame than the experimental

flame. Therefore it can be attributed to the under-prediction of reaction rate and thus turbulent flame speeds

4. A quantitative comparison of the model was performed by running additional simulation at $\phi = 0.25$ and $\phi = 0.45$. The normalized turbulence flame speed from the experiment and numerical simulation were compared and relative errors estimated. The relative error in turbulent flame speed (S_T) reduces with decrease in equivalence ratio from 50 % to less than 30 %.

5. The combustion regime of the flame varied from corrugated flamelets for $\phi = 0.45$ to well stirred reactor for $\phi = 0.25$ as shown in figure 3.15. Since the well mixed model works best for flames in the well stirred reactor regime, this explains the decrease in relative error in S_T with decrease in equivalence ratio.

6. The flow Reynolds number for the cases studied is 4.01×10^4 and the Karlovitz number ranges from 0.434 to 45.62. Wu et al. (1990) and Nakahara and Kido (1998) observed thermo-diffusive instabilities to be significant under similar conditions for premixed turbulent hydrogen flames. The detailed chemistry approach with $k - \epsilon$ model could not capture these effects completely in the simulations as evidenced by the near unity effective Lewis numbers calculated in section 3.6.3.

7. The diffusive coefficients calculated by mixture averaged approach and multi component approach showed no significant difference in the cases studied. Thus the less expensive mixture averaged approach can be used for further studies.

8. The error in the combustion model is attributed to the absence of turbulence chemistry interaction and Lewis number effects.

6.1.2. Analysis of Aerodynamically Trapped Vortex combustor

A preliminary design of a combustor based on aerodynamically trapped vortex flame stabilization concept was developed. The design is based on achieving wall velocity gradients higher than critical velocity gradient of premixed turbulent hydrogen flames near flame stabilization point in the combustor. A fully developed turbulent flow is assumed at the inlet and along the dome section of the combustor. The wall velocity gradients were calculated using the Blasius correlation for pipe flow (eq. 2.3). A detailed analysis of the developed design is performed afterwards and the conclusion are presented here.

1. The section of the combustor with highest risk of flame flashback was identified as the dome wall where the flow velocities and wall velocity gradients are below critical values.

2. The change in inlet mass flow and inlet turbulent intensity had minimal effect on improving the flow properties at the dome wall. It also didn't have any effect on the flow properties near the flame stabilization region.

3. The flame anchored from the separation point is stabilized by recirculation of hot combustion products by the trapped vortex. The combustion regime for the flames with equivalence ratio of $\phi = 0.4$ and 0.5 was identified in the thin reaction zone.

4. The flow along the dome wall is affected by the upstream effects of the flame. There was a significant increase in wall velocity gradient in the second half of the dome wall well above the critical velocity gradient. This is due to the presence of flame causing a partial blockage of the dome section increasing bulk flow velocity. However the values of wall velocity gradient near the entry into the dome wall section saw no improvement.

5. A high temperature region is formed near the wall of the combustor due to the presence of the flame which increases with fuel equivalence ratio. This calls for proper cooling of the combustor walls to prevent any damage to the equipment.

6. The combustor exhaust contained unburned hydrogen indicating incomplete combustion. This can be attributed to absence of core flow combustion or the poor prediction of reaction rates by the well mixed model.

6.2. Recommendations

Recommendations for further research includes :

1. Advanced reaction modelling : The premixed hydrogen-air flames needs to be simulated with a more advanced model capable of including both turbulence chemistry interaction and Lewis number effects. Possible candidates for combustion models capable of including detailed chemistry are the presumed PDF approach and the Flamelet Generated Manifold (FGM). In case of limited computational capability, reduced models should be used to model the combustion.

2. Validation of the numerical model : The combustion models like the one mentioned in recommendation 1 needs to be validated with more experimental cases. The experimental cases should range various operating conditions like preheat temperature, pressure, and equivalence ratio, and burner types such as high swirl burner, low swirl burner etc. The choice of turbulence model is dependent on the type of flow and the combustion model is dependent on the flame regime. Therefore a thorough validation of numerical models at different experimental cases will help identify the best model for various types of flames.

3. Design of the combustor : A better analytical method needs to be developed based on the cold flow results to predict the wall velocity gradients along the dome wall. In the design procedure a fully developed pipe flow is assumed in the entire design space. This assumption need to be validated by experiments and if necessary modified to reflect the exact flow behaviour. The flow simulations needs to be performed for multiple configurations of the dome wall to optimize the geometry for flashback resistance. The objective function in the optimization problem should try to maximize the wall velocity gradient and flow velocity close to the dome wall. Other factors affecting flashback resistance of the combustor should also be investigated through detailed experiments and be incorporated into the optimization problem.

4. Analysis of the ATV combustor : To capture the flow instabilities and smaller scales of the flow, LES simulations needs to be performed. The effect of core flow needs to be included in the analysis by introducing the swirl inlet instead of non-swirling axial flow inlet. Accordingly a sensitivity analysis needs to be performed with this swirl flow.

5. Reactive simulations for the ATV combustor : Further studies should include the effect of swirl flow flame at the core on the trapped vortex flame. The numerical simulations should be performed with a better model validated as mentioned in recommendation 1. The combustion dynamics or the acoustics of the flame should be studied. Studies should be performed at fuel equivalence ratio corresponding to low to high load conditions. The results from the numerical study should be validated with combustor tests.

6. Fuel and Emission : The reactive flow studies should also be performed with fuel other than hydrogen such as methane, syngas etc. This helps to determine the fuel flexibility of the combustor and better optimize the combustor for various types of fuels. To predict the emissions, NO_x and CO mechanisms should be included in the chemistry.

A

Additional Theory

A.1. Hoferichter's model

The Hoferichter's Model for confined flames was developed at TU Munich, Germany by Hoferichter, Hirsch, and Sattelmayer (2016) and is based on onset of flashback in the event of boundary layer separation upstream of flame tip. According to this idea, the flashback is predicted by calculating the minimum pressure rise upstream of flame tip which causes flow separation (Hoferichter, Hirsch, and Sattelmayer, 2016). The author used Stratford's criteria to predict boundary layer separation due to pressure rise upstream induced by flame given by equation A.1.

$$C_p\left(x\frac{dC_p}{dx}\right)^{1/2} = 0.39 \tag{A.1}$$

$$p(x) = p(0) + \frac{\Delta p x^2}{x_f^2} \tag{A.2}$$

$$C_p(x) = \frac{p(x) - p(0)}{0.5.\rho_u U^2} \tag{A.3}$$

$$= \frac{2.\Delta p x^2}{\rho_u U^2 x_f^2} \tag{A.4}$$

$$\frac{dC_p}{dx} = \frac{4.\Delta p x}{\rho_u U^2 x_f^2} \tag{A.5}$$

In these equation, x_f stands for distance from flame tip to point of separation of the flow. ρ_u is the unburned gas density and U is the centerline velocity, which corresponds to the flashback velocity U_{FB}. Substituting the equation A.4 and A.5 in equation A.1, we get,

$$\sqrt{2}\left(\frac{2.\Delta p}{\rho_u U_{FB}^2}\right)^{3/2} = 0.39 \tag{A.6}$$

In calculating the pressure rise, the turbulent flame speed of the H_2-air flame is calculated by taking flame stretch effects into consideration. The back pressure Δp is derived by using continuity and momentum conservation in the flame zone. Setting the unburned gas velocity

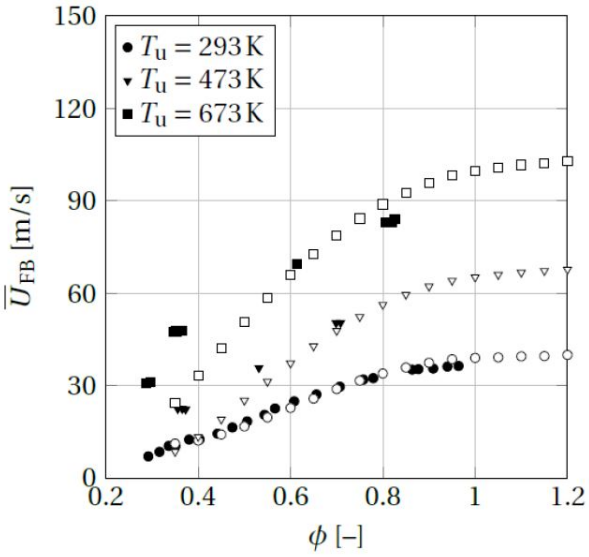

FIGURE A.1: Validation of predicted velocity at flashback with experimental data at atmospheric conditions for channel flow. Filled symbols : experimental data; Empty symbols : predicted values (Hoferichter, Hirsch, and Sattelmayer, 2016).

as the turbulent flame speed S_T,

$$\rho_u u_u = \rho_b u_b \tag{A.7}$$

$$\rho_u u_u^2 + p_u = \rho_b u_b^2 + p_b \tag{A.8}$$

$$p_u - p_b = \Delta p = \rho_b u_b^2 - \rho_u u_u^2 \tag{A.9}$$

$$= \rho_u S_T^2 \left(\frac{\rho_u}{\rho_b} - 1 \right) \tag{A.10}$$

Equations A.6 and A.10 together calculates the free flow velocity needed to prevent flashback. The prediction model was validated with experimental flashback studies conducted by Eichler (2011) for premixed hydrogen air in rectangular channel at different preheating temperatures. The comparison of model predicted flashback limits and that obtained from experiments is shown in figure A.1. Although Hoferichter's Model gave excellent prediction of flashback velocity at room temperature, at higher temperature, large deviations were observed.

B

ATV Design Procedure Source Code

```
1
2  import numpy as np
3  from scipy.optimize import fsolve
4  import cantera as ct
5
6
7  def LFS(phi, Tin, Pin):
8
9      # Inlet pressure
10     p = ct.one_atm * Pin
11
12     # Preheat temperature
13     tburner = Tin
14
15     # Defining gas with chemical mechanism
16     gas = ct.Solution('chem.cti')
17
18     # Transport model for species
19     gas.transport_model = 'Multi'
20
21     mdot = 0.65
22
23     initial_grid = np.linspace(-0.01, 0.4, 9)
24
25     tol_ss = [1.0e-5, 1.0e-10]
26     tol_ts = [1.0e-5, 1.0e-10]
27     # amount of diagnostic output (0 to 8)
28     loglevel = 1
29     # 'True' to enable refinement, 'False' to disable
30     refine_grid = True
31
32     # Equivalence ratio
33     EQUI = phi
34
35     # Species mole fractions
36     io2 = gas.species_index('O2')  # Index of O2 in mix
37     in2 = gas.species_index('N2')  # Index of N2 in mix
38     ih2 = gas.species_index('H2')  # Index of N2 in mix
39     iar = gas.species_index('AR')  # Index of AR in mix
40
41     c = 1
42     comp = [0] * gas.n_species
43     comp[ih2] = 2 * EQUI
44     comp[io2] = c
```

```
45      comp[in2] = 3.76 * c * 0.78 / 0.79
46      comp[iar] = 3.76 * c * 0.01 / 0.79
47
48      # Initializing gas temp, pressure and composition
49      gas.TPX = tburner, p, comp
50
51      # Flame object
52      f = ct.FreeFlame(gas, initial_grid)
53      f.flame.set_steady_tolerances(default=tol_ss)
54      f.flame.set_transient_tolerances(default=tol_ts)
55      f.set_refine_criteria(ratio=2.7, slope=0.06, curve=0.12)
56      f.set_grid_min(1e-9)
57
58      # Set properties of the upstream fuel-air mixture
59      f.inlet.T = tburner
60      f.inlet.X = comp
61      f.inlet.mdot = mdot
62
63      f.set_time_step(1e-5, [2, 5, 10])
64      f.energy_enabled = True
65
66      f.transport_model = 'Multi'
67      try:
68          f.solve(loglevel=loglevel, refine_grid=refine_grid)
69      except Exception:
70          print("failed multi solve at phi = ", EQUI)
71      print("\n***************MULTI ENERGY {0:7f} {1:7f}***************".
        format(EQUI, f.u[0]))
72
73      return f.u[0]
74
75
76  def BLFmodel(C, PRINT, h, dpdx, S_l0, T_u, p_u, phi):
77
78      # Gas constant
79      R = 8.314
80      Ea = 125604.0
81
82      # Lewis numbers
83      Le_O2 = 2.32
84      Le_H2 = 0.33
85
86      gamma2 = 1.
87
88      # Hydraulic diameter
89      D_h = h*2/1000.0
90
91      # An equilibrium reaction (with Cantera) results in burned properties
92
93      gas1 = ct.Solution('chem.cti')
94      x = 'H2:'+str(2*phi)+', O2:1, N2:3.76'
95      gas1.transport_model = 'Multi'              # 'Multi' or 'Mix'
96      gas1.TPX = T_u, p_u*ct.one_atm, x
97
98      rho_u = gas1.TD[1]
99      cp_u = gas1.cp_mass
100     lambda_u = gas1.thermal_conductivity
101     mu_u = gas1.viscosity
102     nu_u = mu_u/rho_u
103     gas1.equilibrate('HP', solver='gibbs')
104     T_ad = gas1.T
105     rho_b = gas1.TD[1]
106     rho_avg = 1*rho_u + 0*rho_b
```

```
107     sigma = rho_u / rho_b
108     gamma1 = sigma
109 
110     # Flame properties
111     # Flame thickness
112     deltaf = 2 * lambda_u / (rho_u * cp_u * S_l0)
113     beta = (Ea * (T_ad - T_u)) / (R * T_ad ** 2)
114     A = 1 + beta * (1 / phi - 1)
115 
116     # Effective lewis number
117     Le = 1 + (Le_O2 - 1 + A * (Le_H2 - 1)) / (1 + A)
118     alfa = gamma1 + 0.5 * beta * (Le - 1) * gamma2
119     Lm = deltaf * (alfa - (sigma - 1) * (gamma1 / sigma))
120     # Integral length scale
121     l_t = 0.1 * D_h
122     s = np.log10(l_t / deltaf)
123 
124     error = 10
125     count = 0
126     U_FB = 1
127     while abs(error) > 0.01:
128         def equation1(eq1):
129             u_tau = eq1
130             return u_tau**2 - (0.03955 * (U_FB-2.4*u_tau)**(7/4.)*(mu_u/
    rho_u)**(1/4.)*(D_h)**(-1/4.))
131         u_tau = fsolve(equation1, 0.1, xtol=1.49012e-2)
132         S_t = 0
133         imax = 50
134         for i in range(5, imax, 1):
135             y = i * (mu_u/(rho_u*u_tau))
136             u_fluc = u_tau*(2.661 - 7.211*np.log(u_tau*y*rho_u/mu_u) +
    7.600*np.log(u_tau*y*rho_u/mu_u)**2
137                             - 2.900*np.log(u_tau*y*rho_u/mu_u)**3 + 0.472*
    np.log(u_tau*y*rho_u/mu_u)**4
138                             - 0.028*np.log(u_tau*y*rho_u/mu_u)**5)
139 
140             Gamma = 10**(-1/(s+0.4)*np.exp(-(s+0.4))+(1-np.exp(-(s+0.4)))
    *(2/3.*(1-1/2.*np.exp(-(u_fluc/S_l0)**(1/3.)))*s-0.11 ))
141 
142             # MODIFICATION: Anistropic flame stretch
143             v_fluc = u_tau*(-0.00052*(u_tau*y*rho_u/mu_u)**2 + 0.045873*(
    u_tau*y*rho_u/mu_u) - 0.014410)
144             w_fluc = u_tau*1.4*(-0.00052*(u_tau*y*rho_u/mu_u)**2 +
    0.045873*(u_tau*y*rho_u/mu_u) - 0.014410)
145 
146             k = 1/2. * (u_fluc**2 + v_fluc**2 + w_fluc**2)
147             kappa_turb = Gamma*u_fluc*v_fluc*w_fluc/(l_t*k)
148             kappa_mean = 0.
149             # kappa_turb = 2/3. * Gamma*u_fluc/l_t
150             kappa_s = 1/2.*u_fluc/l_t
151             kappa = (kappa_mean + kappa_turb + kappa_s)
152             S_ls = S_l0 - kappa*Lm
153             S_t_new = (S_ls * (1 + C * (u_fluc / S_ls) ** 0.5))
154 
155             # MODIFICATION: Lewis correction for all temperatures
156             if T_u > 200:
157                 if Le < 1.0 and Le >=0.5:
158                     S_t_new = (0.6052*(1/Le)**2 - 1.1314*(1/Le) + 1.5224)
    * S_t_new
159                 if Le < 0.50:
160                     S_t_new = S_t_new * 1.678
161 
162             if S_t_new > S_t:
```

```
163                 S_t = S_t_new
164                 Y = u_tau * y *rho_u / mu_u
165                 kappa_FB, Gamma_FB, S_ls_FB = kappa,Gamma,S_ls
166                 u_fluc_FB = u_fluc
167                 S_l0_FB = S_l0
168                 S_ls_FB = S_ls
169                 Ka = (u_fluc / S_l0)**(3/2.) * (l_t/deltaf)**(-1/2.)
170                 u_TAU = u_tau
171
172
173         # Stratford's criterium
174         dp_max = rho_u * S_t**2 * (T_ad/T_u - 1)
175         U_FB_new = (((dp_max + dpdx*0.0001)*(2*dp_max+dpdx*0.0001)**0.5 /
    (0.39))**(2/3.) * 2/rho_u)**0.5
176         error = U_FB_new - U_FB
177         U_FB = U_FB_new
178         count = count+1
179
180         # if Ka > 1:
181         #     flame = 'Thin reaction zone'
182         # elif Ka < 1:
183         #     flame = 'Corrugated flamelets'
184
185     dpdxmax = dp_max/0.01
186     U_FB_bar = U_FB[0] - 2.4*u_TAU[0]
187
188     if PRINT == 1:
189         print('S_t = ', S_t, 'T_u = ', T_u, 'K    ', 'phi = ', round(phi,2)
    , '    ', 'U_FB_bar = ', round(U_FB_bar, 1), 'm/s    ',
190               'u_fluc_FB/S_Ls_FB = ', round(u_fluc_FB[0]/S_ls_FB[0], 1),
    '    ', 'l_t/deltaf = ', round(l_t/deltaf, 1))
191
192     return U_FB_bar, S_t, rho_avg, nu_u, Le, deltaf
193
194
195 def evaluate_h1():
196     # Evaluating for this C
197
198     # Inlet temperature
199     T_u = 550
200
201     # Inlet pressure
202     p_u = 6.7
203
204     # Lists to store output
205     gclist = []
206     h1_list = []
207     vc2list = []
208     fblist = []
209
210     # List of fuel equivalence ratio
211     phi_list = [0.3, 0.35, 0.4, 0.45, 0.5, 0.55, 0.6, 0.65]
212     # Laminar flame speed calculated with function LFS
213     sl_list = [0.0681, 0.22007, 0.4559, 0.7719, 1.14142, 1.5700, 2.0471,
    2.561]
214
215     # Fuel equivalence ratio
216     for i in range(len(phi_list)):
217
218         # Laminar flame speed
219         S_l0 = sllist[i]
220
221         # Equivalence ratio
```

```
222         phi = phi_list[i]
223 
224         # initial height at the trapped vortex
225         h1 = 20
226 
227         # Mass flow rate
228         mf = 0.65
229 
230         while True:
231 
232             # Cross sectional area at inlet to the combustor
233             area1 = np.pi*((h1+h1+h1*0.3)**2 - (h1+h1)**2)*10**(-6)
234             # Cross sectional area at inlet to the dome section
235             area2 = 2*np.pi*(2*h1)*h1*0.5*10**(-6)
236             dpdx = 0
237 
238             # Calling Tober's BLFModel to obtain flashback resistance velocity and flame properties
239             FB_C, S_t, rho, nu_gas, Le, deltal = BLFmodel(2, 0, h1 * 0.3, dpdx, S_l0, T_u, p_u, phi)
240 
241             # Bulk flow velocity at inlet to the combustor
242             V_C2 = mf/(rho*area1)
243 
244             # Bulk flow velocity at inlet to the dome section
245             V_C3 = V_C2*area1/area2
246 
247             # Critical velocity gradient (Lin)
248             gc = S_t / (Le * deltal)
249 
250             # Blasius correlation
251             gf = 0.03955*(V_C3**(7/4))*(nu_gas**(-3/4)) * ((h1*0.5)**(-1/4))
252 
253             print(gc, gf)
254             print('Velocity = {}\t\t Width of channel = {} \t\t Density = {}\t\t Flashback = {}\n\n'.format(V_C2, h1, rho,
255 
                                                                                                                FB_C))
256             # Checking the flashback condition
257             if V_C2 < 2.0*FB_C or gf < 2.0*gc:
258                 h1 = h1 - h1/100
259             elif V_C2 > 2.2*FB_C and gf > 2.2*gc:
260                 h1 = h1 + (150-h1)/100
261             else:
262                 break
263 
264         h1_list.append(h1)
265         fblist.append(FB_C)
266         vc2list.append(V_C2)
267         gclist.append(gc)
268 
269     print(h1_list)
270     print(phi_list)
271     print(fblist)
272     print(vc2list)
273     print(gclist)
274 
275 
276 if __name__ == '__main__':
277     evaluate_h1()
```

C

Additional Simulation Results

C.1. Validation Case Results

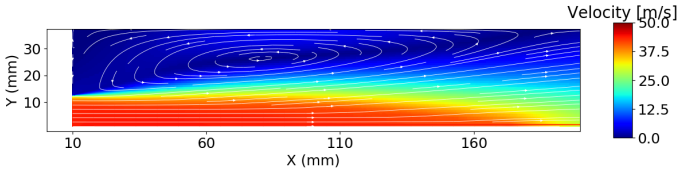

FIGURE C.1: Velocity contour and streamlines at $\phi = 0.25$.

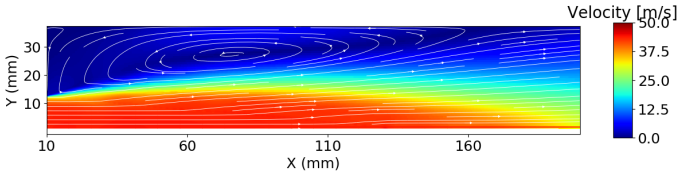

FIGURE C.2: Velocity contour and streamlines at $\phi = 0.35$.

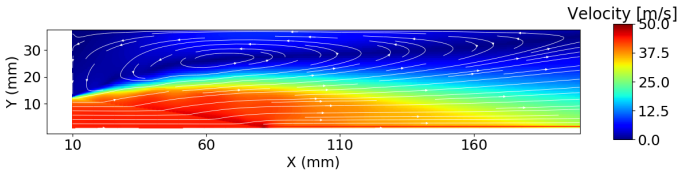

FIGURE C.3: Velocity contour and streamlines at $\phi = 0.45$.

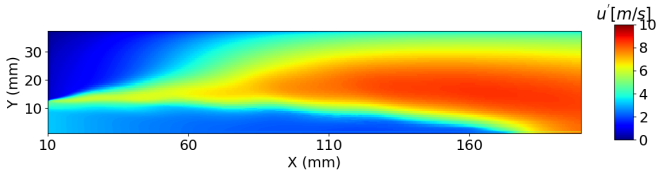

FIGURE C.4: Turbulent velocity contour at $\phi = 0.25$.

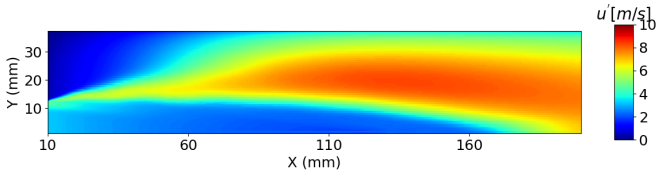

FIGURE C.5: Turbulent velocity contour at $\phi = 0.35$.

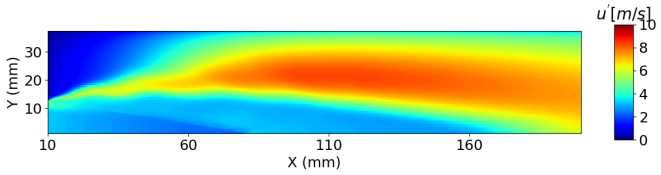

FIGURE C.6: Turbulent velocity contour at $\phi = 0.45$.

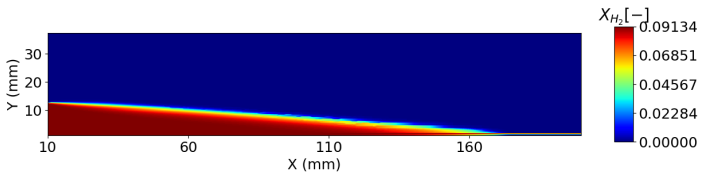

FIGURE C.7: Hydrogen mole fraction distribution at $\phi = 0.25$.

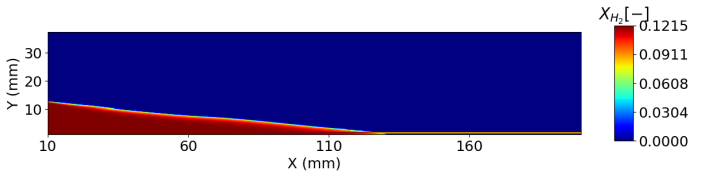

FIGURE C.8: Hydrogen mole fraction distribution at $\phi = 0.35$.

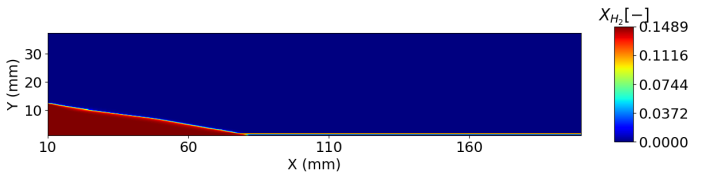

FIGURE C.9: Hydrogen mole fraction distribution at $\phi = 0.45$.

C.2. Aerodynamically Trapped Vortex Results

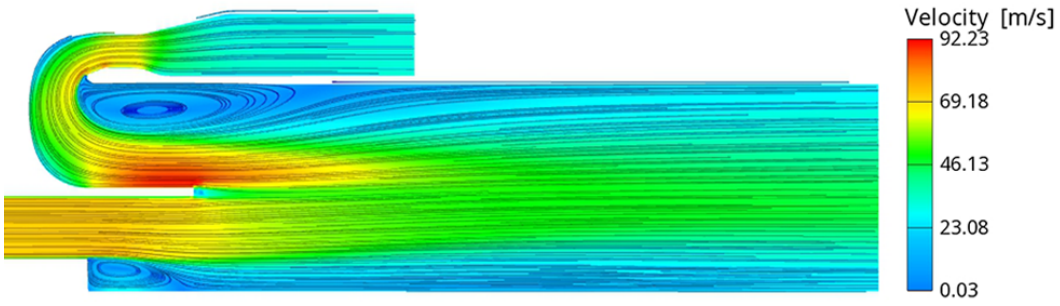

FIGURE C.10: Velocity contour and streamlines for the ATV combustor for inlet $\dot{m} = 0.8$ kg/s.

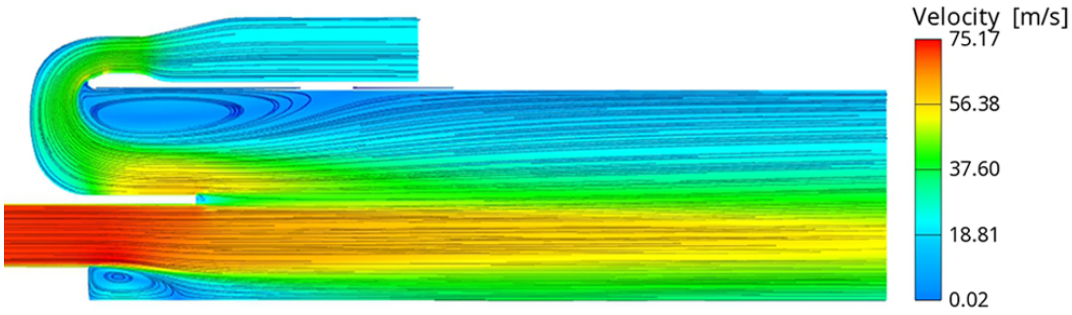

FIGURE C.11: Velocity contour and streamlines for the ATV combustor for inlet $\dot{m} = 0.5$ kg/s.

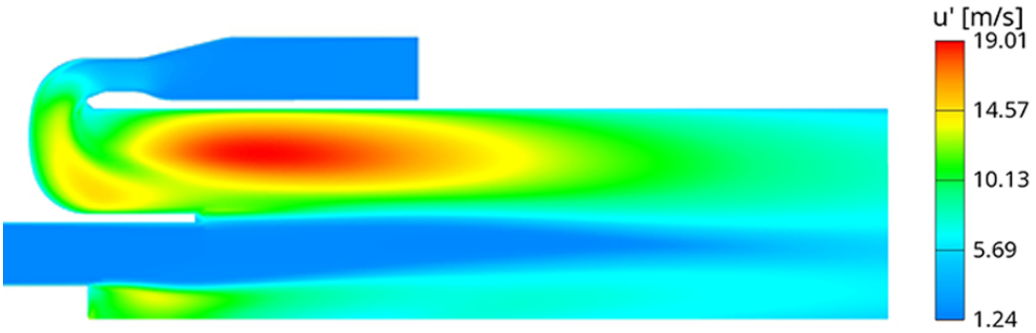

FIGURE C.12: Velocity contour and streamlines for the ATV combustor for inlet turbulent intensity $u^{'} = 24$ %

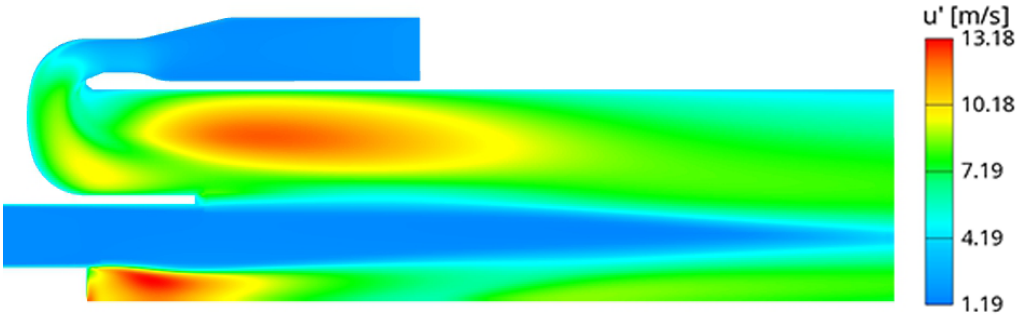

FIGURE C.13: Velocity contour and streamlines for the ATV combustor for inlet turbulent intensity $u^{'} = 15$ %

Bibliography

Beerer, David et al. "Flashback and Turbulent Flame Speed Measurements in Hydrogen/Methane Flames Stabilized by a Low-Swirl Injector at Elevated Pressures and Temperatures". In: *Journal of Engineering for Gas Turbines and Power* 136 (Nov. 2013), p. 031502. DOI: 10.1115/1.4025636.

Benim, Ali Cemal and Khawar J. Syed. "Chapter 7 - Flashback Due to Turbulent Flame Propagation in the Core Flow". In: *Flashback Mechanisms in Lean Premixed Gas Turbine Combustion*. Ed. by Ali Cemal Benim and Khawar J. Syed. Boston: Academic Press, 2015, pp. 45–57. ISBN: 978-0-12-800755-6. DOI: https://doi.org/10.1016/B978-0-12-800755-6.00007-6. URL: http://www.sciencedirect.com/science/article/pii/B9780128007556000076.

— "Chapter 8 - Flashback Due to Flame Propagation in Boundary Layers". In: *Flashback Mechanisms in Lean Premixed Gas Turbine Combustion*. Ed. by Ali Cemal Benim and Khawar J. Syed. Boston: Academic Press, 2015, pp. 59–71. ISBN: 978-0-12-800755-6. DOI: https://doi.org/10.1016/B978-0-12-800755-6.00008-8. URL: http://www.sciencedirect.com/science/article/pii/B9780128007556000088.

Bockris, J.O'M. "The origin of ideas on a Hydrogen Economy and its solution to the decay of the environment". In: *International Journal of Hydrogen Energy* 27.7 (2002). Proceedings of the Selected Papers of the Third International Con ference on Hydrogen Treatment of Materials, HTM-2001, pp. 731–740. ISSN: 0360-3199. DOI: https://doi.org/10.1016/S0360-3199(01)00154-9. URL: http://www.sciencedirect.com/science/article/pii/S0360319901001549.

Borghi, R. "On the Structure and Morphology of Turbulent Premixed Flames". In: *Recent Advances in the Aerospace Sciences: In Honor of Luigi Crocco on His Seventy-fifth Birthday*. Ed. by Corrado Casci and Claudio Bruno. Boston, MA: Springer US, 1985, pp. 117–138. ISBN: 978-1-4684-4298-4. DOI: 10.1007/978-1-4684-4298-4_7. URL: https://doi.org/10.1007/978-1-4684-4298-4_7.

C. Vogel, J and J K. Eaton. "Combined Heat Transfer and Fluid Dynamic Measurements Downstream of a Backward-Facing Step". In: *Journal of Heat Transfer-transactions of The Asme - J HEAT TRANSFER* 107 (Nov. 1985). DOI: 10.1115/1.3247522.

Cheng, R.K. et al. "Laboratory investigations of a low-swirl injector with H2 and CH4 at gas turbine conditions". In: *Proceedings of the Combustion Institute* 32.2 (2009), pp. 3001–3009. ISSN: 1540-7489. DOI: https://doi.org/10.1016/j.proci.2008.06.141. URL: http://www.sciencedirect.com/science/article/pii/S1540748908001430.

Cheng, R.K et al. *Development of a low swirl injector concept for gas turbines*. July 2000. URL: https://www.osti.gov/servlets/purl/785290.

D. York, William, Willy S. Ziminsky, and Ertan Yilmaz. "Development and Testing of a Low NOX Hydrogen Combustion System for Heavy Duty Gas Turbines". In: vol. 135. June 2012. DOI: 10.1115/GT2012-69913.

Dam, Bidhan et al. "Effects of syngas composition on combustion induced vortex breakdown (CIVB) flashback in a swirl stabilized combustor". In: *Fuel* 90.11 (2011), pp. 3274–3284. ISSN: 0016-2361. DOI: https://doi.org/10.1016/j.fuel.2011.06.024. URL: http://www.sciencedirect.com/science/article/pii/S0016236111003425.

Daniele, S et al. "Flame front/turbulence interaction for syngas fuels in the thin reaction zones regime: Turbulent and stretched laminar flame speeds at elevated pressures and temperatures". In: *Journal of Fluid Mechanics* 724 (June 2013), pp. 36–68. DOI: 10.1017/jfm.2013.141.

De, Santanu, Avinash Agarwal, et al. *Modeling and Simulation of Turbulent Combustion*. Dec. 2017. ISBN: 978-981-10-7409-7. DOI: 10.1007/978-981-10-7410-3.

De, Santanu and Swetaprovo Chaudhuri. "Mechanics and Modelling of Turbulence–Combustion Interaction". In: *Modeling and Simulation of Turbulent Combustion*. Ed. by Santanu De et al. Singapore: Springer Singapore, 2018, pp. 3–43. ISBN: 978-981-10-7410-3. DOI: 10.1007/978-981-10-7410-3_1. URL: https://doi.org/10.1007/978-981-10-7410-3_1.

Dowling, A.p. "The calculation of thermoacoustic oscillations". In: *Journal of Sound and Vibration* 180.4 (1995), pp. 557–581. DOI: 10.1006/jsvi.1995.0100.

Durbin, Paul A. "Near-wall turbulence closure modeling without "damping functions"". In: *Theoretical and Computational Fluid Dynamics* 3.1 (1991), pp. 1–13.

Eichler, Christian Thomas. "Flame Flashback in Wall Boundary Layers of Premixed Combustion Systems". PhD thesis. 2011.

F Magnussen, Bjørn. "The eddy dissipation concept: A bridge between science and technology". In: *Thematic Conference on Computational Combustion* (Jan. 2005).

Fritz, Jassin, Martin Kröner, and Thomas Sattelmayer. "Flashback in a Swirl Burner With Cylindrical Premixing Zone". In: *Journal of Engineering for Gas Turbines and Power-transactions of The Asme - J ENG GAS TURB POWER-T ASME* 126 (Apr. 2004). DOI: 10.1115/1.1473155.

Funke, Dr.-Ing. Harald et al. "Experimental and Numerical Characterization of the Dry Low NOx Micromix Hydrogen Combustion Principle at Increased Energy Density for Industrial Hydrogen Gas Turbine Applications". In: vol. 1. June 2013. DOI: 10.1115/GT2013-94771.

Goodwin, David G. et al. *Cantera: An Object-oriented Software Toolkit for Chemical Kinetics, Thermodynamics, and Transport Processes*. https://www.cantera.org. Version 2.4.0. 2018. DOI: 10.5281/zenodo.1174508.

Hanjalic, K., M. Popovac, and M. Hadžiabdić. "A robust near-wall elliptic-relaxation eddy-viscosity turbulence model for CFD". In: *International Journal of Heat and Fluid Flow* 25.6 (2004), pp. 1047–1051. ISSN: 0142-727X. DOI: https://doi.org/10.1016/j.ijheatfluidflow.2004.07.005. URL: http://www.sciencedirect.com/science/article/pii/S0142727X0400116X.

Hinze, J.O. *Turbulence:* McGraw-Hill classic textbook reissue series. McGraw-Hill, 1975. ISBN: 9780070290372. URL: https://books.google.nl/books?id=xfRQAAAAMAAJ.

Hoferichter, Vera, Christoph Hirsch, and Thomas Sattelmayer. "Prediction of Confined Flame Flashback Limits Using Boundary Layer Separation Theory". In: *Journal of Engineering for Gas Turbines and Power* 139 (July 2016). DOI: 10.1115/1.4034237.

Hoferichter, Vera, Christoph Hirsch, Thomas Sattelmayer, et al. "Comparison of Two Methods to Predict Boundary Layer Flashback Limits of Turbulent Hydrogen-Air Jet Flames". In: *Flow, Turbulence and Combustion* 100 (Dec. 2017). DOI: 10.1007/s10494-017-9882-2.

Johnson, M.R. et al. "A comparison of the flowfields and emissions of high-swirl injectors and low-swirl injectors for lean premixed gas turbines". In: *Proceedings of the Combustion Institute* 30.2 (2005), pp. 2867–2874. ISSN: 1540-7489. DOI: https://doi.org/10.1016/j.proci.2004.07.040. URL: http://www.sciencedirect.com/science/article/pii/S0082078404000384.

Jung, Yongjin, Min Jung Lee, and Nam Il Kim. "Direct prediction of laminar burning velocity and quenching distance of hydrogen-air flames using an annular stepwise diverging

tube (ASDT)". In: *Combustion and Flame* 164 (2016), pp. 397–399. ISSN: 0010-2180. DOI: https://doi.org/10.1016/j.combustflame.2015.12.005. URL: http://www.sciencedirect.com/science/article/pii/S0010218015004484.

Kalantari, Alireza, Elliot Sullivan-Lewis, and Vincent Mcdonell. "Flashback Propensity of Turbulent Hydrogen-Air Jet Flames at Gas Turbine Conditions". In: *Journal of Engineering for Gas Turbines and Power* 138 (Oct. 2015). DOI: 10.1115/1.4031761.

Lam, Kam-Kei, Philipp Geipel, and Jenny Larfeldt. "Hydrogen Enriched Combustion Testing of SIEMENS Industrial SGT-400 at Atmospheric Conditions". In: *Journal of Engineering for Gas Turbines and Power* 137 (Sept. 2014), p. 021502. DOI: 10.1115/1.4028209.

Lam, Kam-Kei and Nishant Parsania. "Hydrogen Enriched Combustion Testing of Siemens SGT-400 at High Pressure Conditions". In: June 2016, V04BT04A019. DOI: 10.1115/GT2016-57470.

Lefebvre, Arthur H. (Arthur Henry) and Dilip R Ballal. *Gas turbine combustion : alternative fuels and emissions*. English. 3rd ed. "A CRC title." Boca Raton, FL : CRC Press, 2010. ISBN: 9781420086041 (hbk.) URL: http://lib.myilibrary.com?id=692822.

Lewis, Bernard and Guenther von Elbe. "Stability and Structure of Burner Flames". In: *The Journal of Chemical Physics* 11.2 (1943), pp. 75–97. DOI: 10.1063/1.1723808. eprint: https://doi.org/10.1063/1.1723808. URL: https://doi.org/10.1063/1.1723808.

Li, Juan et al. "An updated comprehensive kinetic model of hydrogen combustion". In: *International Journal of Chemical Kinetics* 36 (Oct. 2004), pp. 566–575. DOI: 10.1002/kin.20026.

Liang, Long, John G. Stevens, and John T. Farrell. "A Dynamic Multi-Zone Partitioning Scheme for Solving Detailed Chemical Kinetics in Reactive Flow Computations". In: *Combustion Science and Technology* 181.11 (2009), pp. 1345–1371. URL: https://doi.org/10.1080/00102200903190836.

Lin, Yu-chun. PhD thesis. ETH-Zürich, 2014. URL: https://doi.org/10.3929/ethz-a-010248887.

Lipatnikov, A.N. and J. Chomiak. "Molecular transport effects on turbulent flame propagation and structure". In: *Progress in Energy and Combustion Science* 31.1 (2005), pp. 1–73. ISSN: 0360-1285. DOI: https://doi.org/10.1016/j.pecs.2004.07.001. URL: http://www.sciencedirect.com/science/article/pii/S0360128504000486.

Littlejohn, D et al. "Development of the Low Swirl Injector for Fuel-Flexible GasTurbines". In: 6 (Jan. 2007). URL: https://www.researchgate.net/publication/239877341_Development_of_the_Low_Swirl_Injector_for_Fuel-Flexible_GasTurbines.

Miranda, Paulo Emílio V. de. "Chapter 1 - Hydrogen Energy: Sustainable and Perennial". In: *Science and Engineering of Hydrogen-Based Energy Technologies*. Ed. by Paulo Emilio V. de Miranda. Academic Press, 2019, pp. 1–38. ISBN: 978-0-12-814251-6. DOI: https://doi.org/10.1016/B978-0-12-814251-6.00001-0. URL: http://www.sciencedirect.com/science/article/pii/B9780128142516000010.

Movileanu, Codina et al. "Adiabatic Flame Temperature of Fuel-Air Mixtures, in Isobaric and Isochoric Combustion Processes". In: *Revista de Chimie -Bucharest- Original Edition-* 62 (Apr. 2011), pp. 376–379.

Nakahara, Masaya and H. Kido. "A study of the premixed turbulent combustion mechanism taking the preferential diffusion effect into consideration". In: *Memoirs of the Kyushu University, Faculty of Engineering* 58 (June 1998), pp. 55–82.

Noble, David et al. "Syngas Mixture Composition Effects Upon Flashback and Blowout". In: *Proceedings of the ASME Turbo Expo* 1 (Jan. 2006). DOI: 10.1115/GT2006-90470.

Ó Conaire, Marcus et al. "A comprehensive modeling study of hydrogen oxidation". In: *International Journal of Chemical Kinetics* 36.11 (2004), pp. 603–622. DOI: 10.1002/kin.20036. eprint: https://onlinelibrary.wiley.com/doi/pdf/10.1002/kin.

20036. URL: https://onlinelibrary.wiley.com/doi/abs/10.1002/kin.20036.

O'Connor, J., S. Hemchandra, and T. Lieuwen. "7 - Combustion Instabilities in Lean Premixed Systems". In: *Lean Combustion (Second Edition)*. Ed. by Derek Dunn-Rankin and Peter Therkelsen. Second Edition. Boston: Academic Press, 2016, pp. 231–259. ISBN: 978-0-12-804557-2. DOI: https://doi.org/10.1016/B978-0-12-804557-2.00007-9. URL: http://www.sciencedirect.com/science/article/pii/B9780128045572000079.

Oijen, Jeroen van and Philip Goey. "Modelling of Premixed Laminar Flames using Flamelet-Generated Manifolds". In: *Combustion Science and Technology - COMBUST SCI TECHNOL* 161 (Dec. 2000), pp. 113–137. DOI: 10.1080/00102200008935814.

Peter, N. "The turbulent burning velocity for large-scale and small-scale turbulence". In: *Journal of Fluid Mechanics* 384 (1999), pp. 107–132. DOI: 10.1017/S0022112098004212.

Physical Properties of natural gases. N.V. Nederlandse Gasunie, 1988.

Poinsot, Thierry and Denis Veynante. "Theoretical and Numerical Combustion". In: *Prog. Energy Combust. Sci.* 28 (Jan. 2005).

Pomraning, Eric, Keith Richards, and P. K. Senecal. *Modeling Turbulent Combustion Using a RANS Model, Detailed Chemistry, and Adaptive Mesh Refinement*. Apr. 2014. URL: https://www.sae.org/publications/technical-papers/content/2014-01-1116/.

Pope, S. B. *Turbulent flows*. Cambridge University Press, 2015.

Ramaekers, Wilhelmus et al. "Comparison of different CFD models for predicting emissions in an OPRA DLE combustor". In: June 2019.

Reichel, Thoralf, Steffen Terhaar, and Christian Paschereit. "Flashback Resistance and Fuel–Air Mixing in Lean Premixed Hydrogen Combustion". In: *Journal of Propulsion and Power* 34 (Jan. 2018), pp. 670–701. DOI: 10.2514/1.B36646.

Rizkalla, Hany et al. "FlameSheet™ Combustor Extended Engine Validation for Operational Flexibility and Low Emissions". In: June 2018, V003T08A004. DOI: 10.1115/GT2018-75764.

Schlichting, Hermann and Klaus Gersten. *Boundary-layer theory*. Springer, 2016.

Siewert, Piotr. "Flame front characteristics of turbulent lean premixed methane / air flames at high-pressure". PhD thesis. ETH, 2006. URL: https://www.research-collection.ethz.ch/handle/20.500.11850/149334?show=full.

Smith, Gregory P. et al. *GRI-Mech 3.0*. URL: http://www.me.berkeley.edu/gri_mech/.

Ströhle, Jochen and Tore Myhrvold. "An evaluation of detailed reaction mechanisms for hydrogen combustion under gas turbine conditions". In: *International Journal of Hydrogen Energy* 32.1 (2007), pp. 125–135. ISSN: 0360-3199. DOI: https://doi.org/10.1016/j.ijhydene.2006.04.005. URL: http://www.sciencedirect.com/science/article/pii/S0360319906001716.

Stuttaford, Peter John, Stephen Jorgensen, et al. *Flamesheet combustor dome*. US Patent 9,752,781. May 2017.

Stuttaford, Peter John and Hany Rizkalla. *Flamesheet combustor contoured liner*. US Patent App. 10/060,630. Aug. 2018.

Stuttaford, Peter J et al. *Flamesheet combustor*. US Patent 6,935,116. Aug. 2005.

Stuttaford, Peter et al. "FlameSheet Combustor Engine and Rig Validation for Operational and Fuel Flexibility With Low Emissions". In: *Proceedings of ASME Turbo Expo 2016: Turbmachinery Technical Conference and Exposition* 4A (June 2016), p. 11. DOI: 10.1115/GT2016-56696.

Taylor, R. and R. Krishna. *Multicomponent Mass Transfer*. Wiley Series in Chemical Engineering. Wiley, 1993. ISBN: 9780471574170. URL: https://books.google.nl/books?id=FrpX9dNjWc0C.

Tober, Joeri. *Boundary layer flashback prediction of a low emissions full hydrogen burner for gas turbine applications*. Jan. 2019. URL: https://repository.tudelft.nl/islandora/object/uuid:29260da8-c1e9-4ffb-932b-121ce0326752?collection=education.

Varley, James. *Testing Time for FlameSheet*. Nov. 2017. URL: https://www.ansaldoenergia.com/PublishingImages/news/Recent%5C%20Success%5C%20with%5C%20Ansaldo%5C%E2%5C%80%5C%99s%5C%20FlameSheet%5C%E2%5C%84%5C%A2%5C%20Combustion%5C%20System/Ansaldo%5C%20FlameSheet%5C%28TM%5C%29%5C%20Combustion%5C%20System%5C%20-%5C%20MPS%5C%20Nov%5C%202017.pdf.

Venkateshan, S.P. and Prasanna Swaminathan. "Chapter 9 - Numerical Integration". In: *Computational Methods in Engineering*. Ed. by S.P. Venkateshan and Prasanna Swaminathan. Boston: Academic Press, 2014, pp. 317–373. ISBN: 978-0-12-416702-5. DOI: https://doi.org/10.1016/B978-0-12-416702-5.50009-0. URL: http://www.sciencedirect.com/science/article/pii/B9780124167025500090.

Wilcox, David C et al. *Turbulence modeling for CFD*. Vol. 2. DCW industries La Canada, CA, 1998.

Wohl, Kurt. "Quenching, flash-back, blow-off-theory and experiment". In: *Symposium (International) on Combustion* 4.1 (1953). Fourth Symposium (International) on Combustion, pp. 68–89. ISSN: 0082-0784. DOI: https://doi.org/10.1016/S0082-0784(53)80011-1. URL: http://www.sciencedirect.com/science/article/pii/S0082078453800111.

Wu, M. S. et al. "Turbulent Premixed Hydrogen/Air Flames at High Reynolds Numbers". In: *Combustion Science and Technology* 73.1-3 (1990), pp. 327–350. DOI: 10.1080/00102209008951655. eprint: https://doi.org/10.1080/00102209008951655. URL: https://doi.org/10.1080/00102209008951655.

Zel'dovich, Ya B. "Theory of Combustion and Detonation of Gases [in Russian], Izd". In: *AN SSSR* (1944).

Zhao, Dan, Ephraim Gutmark, and Philip de Goey. "A review of cavity-based trapped vortex, ultra-compact, high-g, inter-turbine combustors". In: *Progress in Energy and Combustion Science* 66 (2018), pp. 42–82. ISSN: 0360-1285. DOI: https://doi.org/10.1016/j.pecs.2017.12.001. URL: http://www.sciencedirect.com/science/article/pii/S0360128517300898.